Fakulteit Ingenieurswese, Bou-omgewing & IT
Faculty of Engineering, Built Environment & IT

School of Engineering

Department of Materials Science and Metallurgical Engineering

This report is completed in partial fulfilment of requirements for

the degree of MEng (Metallurgical Engineering) at the University of Pretoria

Characterisation of Wear in Natural Rubber and Polyurethane Hydrocyclones Used for Minerals Processing Applications

by

S. Combrink 12214282

Supervisor: Prof. Natasia Naude
Date of Submission: 29 April 2020

UNIVERSITEIT VAN PRETORIA
UNIVERSITY OF PRETORIA
YUNIBESITHI YA PRETORIA
Denkleiers • Leading Minds • Dikgopolo tša Dihlalefi

Abstract

Slurry wear is a common problem in the minerals processing industry. Hydrocyclones are widely used in wet mineral classification applications and can be notoriously prone to wear. This study investigated wear in hydrocyclones, with specific attention to wear of spigots in polyurethane- and natural rubber-lined cyclones.

Hydrocyclone wear, and more specifically spigot wear and its influence on efficiency (imperfection value), was investigated for a Multotec HC250 (250 mm barrel diameter) hydrocyclone. The HC250 hydrocyclone comprised a metal shell lined with vulcanized natural rubber, with a thermoset polyurethane spigot and vortex finder. Tests were conducted on this hydrocyclone in a pilot-scale recirculating test setup. The wear rate of the spigot was quantified by measuring its volume change with operating time using microcomputed-tomography scans. After 122 days in operation (recirculating feed materials in a closed loop), wear in the hydrocyclone led to an increase of 13.67% in the volume of the spigot. This relatively low wear rate was related to the fact that material recirculation led to particle smoothening and a reduction in particle size. This result also showed the enormous influence of particle shape and size on wear. A large single wear groove at the bottom of the natural rubber lower cone formed due to localized porosity (a compression-moulding defect), as determined by microcomputed tomography. The worn natural rubber lining also showed signs of chemical attack (devulcanization) occurring at microscopic level. In terms of efficiency, it was found that wear in the spigot resulted in a lower imperfection value of 0.48 compared with that of 0.39 for a new spigot. The relative density of the underflow decreased significantly from a value of 1.359 for the new hydrocyclone to 1.183 when worn. Although the worn spigot recovered a larger amount of water to the underflow, misplacement of fines and the fish-hook effect were greater for the new spigot.

Multotec VV165 polyurethane (165 mm barrel diameter) hydrocyclones, used at the Exxaro Grootegeluk coal dense medium separation plant (South Africa) for magnetite densification, were also evaluated to determine their wear rate and enable more informed decisions on replacement intervals. It was found that after 90 days of operation in densifying magnetite medium (−45 µm), these hydrocyclones showed no wear, based on the change in volume in the spigot as measured by microcomputed tomography. These findings showed the importance of particle size on the wear rate of a hydrocyclone spigot and confirmed the requirement of a critical diameter at a set velocity to cause wear. The magnetite medium of −45 µm was below the critical particle diameter that would cause wear within this time period.

Keywords: Hydrocyclone, Wear, Efficiency, Microcomputed tomography.

TABLE OF CONTENTS

List of Tables

List of Figures

Nomenclature

CFD	computational fluid dynamics
d50	hydrocyclone cut size
Dc	barrel diameter
DMS	dense medium separation
Du	spigot inner diameter
HV	Vickers hardness
IMP	imperfection, slope of the partition curve
IRHD	international rubber hardness degree
K_{IC}	plane strain fracture toughness
LPT	Lagrangian particle tracking
LZVV	line of zero vertical velocity
Micro-CT	microcomputed tomography
NR	vulcanized natural rubber
O/F	Overflow of cyclone
PTFE	polytetrafluoroethylene
PU	polyurethane
RD	relative density
PSD	particle size distribution
Sa	arithmetic mean roughness
SAR	slurry abrasivity resistance number
SBR	styrene-butadiene rubber
SF	shape factor
SG	specific gravity
SJE	Slurry jet erosion
%Sm	solids concentration by mass
TPU	thermoplastic polyurethane
U/F	underflow of cyclone

Acknowledgements

Firstly, I would like to express my appreciation to my supervisor, Prof. Natasia Naude, for guiding me throughout this project and all her contributions made towards the project. I would also like to thank her for her significant contribution towards my professional development. I would also like to express gratitude towards Mr W. Roux, Prof. G.T. van Rooyen and Prof. J. Labuschagne from the University of Pretoria for their assistance.

I am also grateful for the assistance of my supervisor at Multotec, Mr F. Bornman, and Multotec for making this project possible by sponsoring the project and for the use of the Multotec R&D facilities to conduct test work. I would also like to thank Multotec for the assistance in constructing and modifying the test rig. The Multotec R&D team assisted me throughout the project in managing the test rig, which ran for weeks on end. I would like to thank the whole Multotec team for their assistance.

The microcomputed-tomography scans were carried out at the Nuclear Energy Corporation of South Africa (NECSA) using their MIXRAD facilities. I would like to thank Dr F. De Beer and Mr J. Hoffman for making the facilities available for the wear analysis and for accommodating me. Mr J. Hoffman also assisted greatly with reconstruction and analysis work at NECSA. Mr Kyle Naidoo from Exxaro also assisted and collaborated with me on the research done on the wear of densification cyclones at Exxaro. English language editing was carried out by Dr. K. Sole and Mr L. Neethling. Lastly, I would like to thank my family for all their support.

CHAPTER 1: OVERVIEW

1.1 Effect of Wear on Hydrocyclones

Wear is a common problem in the mining and minerals processing industry, and material losses lead to significant financial losses. According to Holmberg *et al.* (2017), friction and wear contribute to estimated annual losses of EUR 210,000 million worldwide. The cost of replacing worn-out equipment can heavily impact operating costs and decrease overall profitability of an operation.

Wear in mining also results in an estimated 970 million tons of carbon dioxide emissions worldwide per year due to material replacement, Holmberg *et al.* (2017). Worn-out equipment creates a lot of excess waste that needs to be managed. Another important factor is efficiency reduction due to functional damage to equipment. Losses in efficiency can have various negative downstream effects on a process, such as material misplacement, energy losses and safety risks.

1.2 Objectives

The objective of this research was to investigate wear in polyurethane (PU)- and natural rubber (NR)-lined hydrocyclones. The wear mechanisms in these hydrocyclones (i.e., the driving forces for wear) were analysed, along with the influence of feed particle size and substrate material properties. A hydrocyclone test rig was constructed to produce wear and was used to evaluate the relationship between spigot wear and efficiency (i.e., the partition curve).

1.3 Overview

This thesis is presented in five chapters. The outlines of those following Chapter 1 are described below.

Chapter 2: Literature

The literature study covers cyclones, with a focus on hydrocyclones, their various applications and operating conditions. The difference between erosive and abrasive wear is highlighted. Various wear tests are discussed and compared to evaluate wear mechanisms and their relevance to hydrocyclone wear. Hydrocyclone materials of construction were investigated, with a focus on polymers and metals. Lastly, the influences of slurry feed and particle properties on wear were examined.

Chapter 3: Methodology

The methodology section describes the experimental procedures and the different tests that were utilized in this study. Construction of the experimental setup (hydrocyclone test rig) is described.

Chapter 4: Results and Discussion

In this section, the various results of the project are given, critically discussed and compared with those reported in literature.

Chapter 5: Conclusion and Recommendations

The main findings of the project are highlighted, along with recommendations for future work.

CHAPTER 2: LITERATURE REVIEW

2.1 Introduction

This chapter deals with various aspects of hydrocyclone wear, applications, separation mechanisms, geometry, concentration distribution, energy distribution and efficiency.

The two main wear mechanisms and different wear test methods are discussed. Hydrocyclone materials of construction are investigated to determine which material properties are associated with higher wear resistance. The influences of feed and particle properties on erosive wear are also examined.

2.2 Cyclones (Dense Medium Separation and Hydrocyclones)

Cyclones are devices that separate particles based on their difference in specific gravity (SG) (i.e., density) and particle size (Gupta and Yan, 2016). Cyclones have the advantage of being able to handle very large throughputs and are mechanically simple to operate and maintain. Suspended particles within a fluid or slurry enter the cyclone inlet under pressure by using either a pump or gravity. Upon entering the cyclone, the slurry forms two multiphase free vortexes that flow upwards towards the vortex finder and downwards towards the spigot. These two vortices are divided by a zero vertical (axial) velocity line (LZVV), as displayed in Figure 2.1, where the axial velocity is zero: once a particle moves beyond this radial point, the particle will move with the flow of the inner or outer vortex.

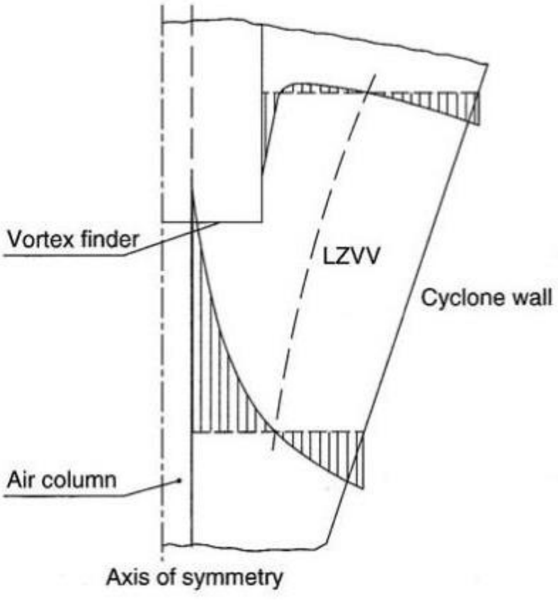

Figure 2.1: Diagram showing the theoretical line of zero vertical velocity (LZVV) in a hydrocyclone, where the axial flow changes direction, flowing downwards on the side closest to the hydrocyclone wall and flowing upwards in the inner area (Richardson and Harker, 2002).

An air core is also created at the spigot and forms an air vortex (Robinson and Garcia, 2015) along the axis of the cyclone, which is also a low-pressure zone. Within the helical flow pattern of the cyclone, particles with greater mass, which is a function of SG and volume, experience a greater radial outward centrifugal force and have a greater probability of overcoming opposing inward forces, most notably drag. Particles with greater mass will, therefore, move outwards towards the downward-flowing vortex that discharges at the spigot; particles with less mass have a greater probability of remaining within the inner vortex or being forced inward by displaced fluid, most notably due to drag, and flow upwards towards the vortex finder (Wills and Napier-Munn, 2006). Figure 2.2(a) shows a dense medium separation (DMS) cyclone and (b) shows a hydrocyclone.

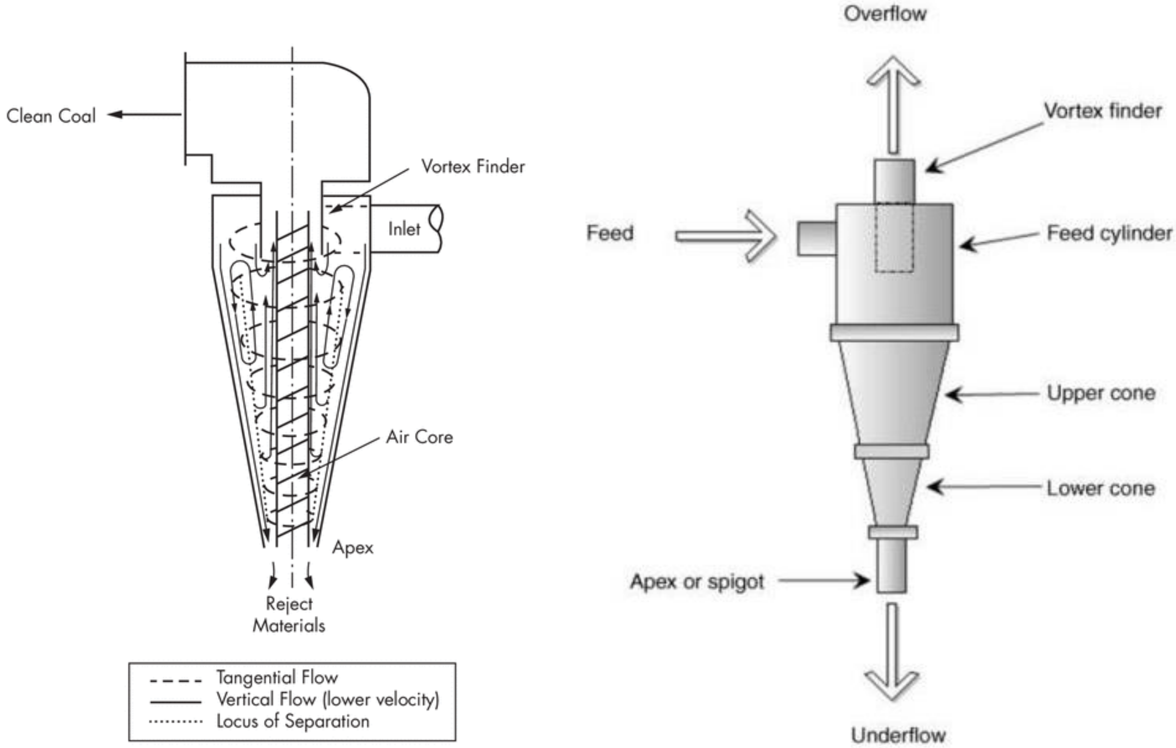

a) *b)*

Figure 2.2: (a) Schematic representation of dense medium separation cyclone, used for concentrating coal. The basic flow directions are indicated and the locus of separation (LZVV: line of zero vertical velocity) (Dunne et al.*, 2019). (b) Schematic sketch of hydrocyclone, showing the various parts and flow directions (Gupta and Yan, 2016).*

Hydrocyclones are used in various industries, including drilling, petrochemical (liquid/liquid hydrocyclone), and food and paper manufacturing. Hydrocyclones are also one of the most commonly used wet classifiers (liquid/solid hydrocyclone) in the minerals processing industry. The use of hydrocyclones as classifiers started to emerge in the 1950s (Flintoff and Kuehl II, 2011). The various parts of a hydrocyclone are shown in Figure 2.2(b), which include the overflow pipe, vortex finder, feed cylinder (inlet) and barrel (optional), upper cone (optional in the case of a flat bottom), lower cone (optional) and spigot. Hydrocyclones are primarily used for size classification purposes and work more efficiently with a homogenous SG particle feed (Gupta and Yan, 2016). A large SG variation between classified particles can lead to lower separation efficiency because some larger particles with a lower relative SG report to the overflow. This happens partly due to heavy medium formation at the hydrocyclone wall by the heavier particles (Flintoff and Kuehl II, 2011).

DMS cyclones were developed in the Netherlands in the 1940s and have become one of the most popular dense medium concentrators used in the minerals processing industry (Dunne *et al.*, 2019). In most cases, DMS cyclones use a higher density medium to separate particles based on SG. Water-only automedium cyclones are also used for gravity separation in fine coal applications (Flintoff and Kuehl II, 2011). The medium usually consists of ultra-fine (−75 µm) magnetite or ferrosilicon particles and the density of the medium is determined by the number of particles (magnetite or ferrosilicon) in suspension. The actual cut density will usually be higher than the medium density in a DMS cyclone due to a densification effect that occurs within the lower regions of the cyclone (Gupta and Yan, 2016). The use of a medium (fluid with a higher density) influences the magnitude of the resultant radial outward force experienced by a particle in a cyclone. Particles with a density close to or lower than that of the medium will experience a much smaller resultant radial outward force compared with a particle with a high density relative to the medium. These lower-density particles will mostly move upwards towards the vortex finder. In DMS cyclone applications, the product can move to either the underflow (U/F) or overflow (O/F); for example, in coal processing, the product will go to the overflow, while in diamond recovery, the diamonds will report to the underflow (Wills and Napier-Munn, 2006).

The primary difference between DMS cyclones and hydrocyclones is that the latter do not artificially increase the density of the medium, as in the case of DMS cyclones.

2.3 Hydrocyclones

A more in-depth view of hydrocyclones is given in this section, which includes various applications, materials of construction, separation mechanisms, models, the conditions present within a hydrocyclone and how efficiency is measured.

2.3.1 Hydrocyclone Applications

Hydrocyclones are used for various applications in the minerals processing industry. Table 2.1 summarizes some applications for commonly mined ores and minerals in Southern Africa. Not all hydrocyclone applications are equally sensitive to wear and therefore the downstream impact (i.e., influence on mineral recovery) due to hydrocyclone wear will differ.

An example of a wear-sensitive application is the classification cyclones that are used in milling circuits. These are critical to a process, mainly because the cut point, recirculating load and efficiency have a direct impact on optimal liberation of particles. If wear influences these parameters due to geometrical changes (Wills and Napier-Munn, 2006), it could lead to lower downstream mineral recovery. An example of a less-critical application would be a tailings dewatering cyclone. This application will not influence mineral recovery, but will only have an impact on the moisture content of the tailings.

Maintenance requirements and replacement schedules have an influence on the operating cost of a plant and premature replacement of components leads to higher operating costs. Therefore, it is important to evaluate how critical a hydrocyclone application is to a process.

Table 2.1: Different hydrocyclone types and applications common in Southern Africa (Olson and Turner, 2002).

Ore	Cyclone type	Application
Gold	Classification	Size classification in milling circuit
	Tailings	Used to build a tailings dam or dewater tailings
Coal	Classification e	Size classification and fines removal
	Densification (medium)	Used to control the density of a medium
	Densification	Densification of discards or product
Platinum and chrome	Desliming	Used prior to spirals
	Tailings	Used to build a tailings dam or dewater tailings
	Classification	Size classification in a milling circuit
	Stacker	Used with secondary mill and for dewatering chrome product
	Degrit	Used with a thickener to dewater tailings
Copper	Classification	Used for size classification in a milling circuit
	Tailings	Used to build a tailings dam or dewater tailings
Iron	Classification	Used for size classification
	Densification	Used to control a medium density
Mineral sands	Classification	Used in a closed circuit with a trommel screen and for spiral feed
	Stacker	Used to dewater product and tailings

2.3.2 Separation Mechanisms and Models

The balanced orbit theory is a widely accepted theory of separation for hydrocyclones and is one of the oldest models (Wills and Napier-Munn, 2006). In this model, only the centrifugal and drag forces are used to describe the mechanism of separation, where larger and denser particles (relative to the fluid) will experience a greater centrifugal force compared with smaller particles with the same SG (Equation 2.1). The centrifugal force acts in the outward radial direction towards the hydrocyclone wall and the drag force acts in the inward direction, as illustrated in Figure 2.3.

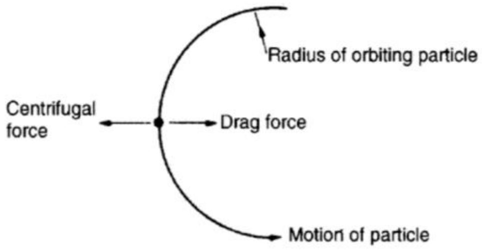

Figure 2.3: Two main separation forces exerted on particles in hydrocyclones (Wills and Napier-Munn, 2006).

The basic mechanism of separation proposed by Barth's balanced orbit theory is based on two governing equations: Equation 2.1 describes the centrifugal force experienced by a particle in a vortex, assuming that the particle acts as a fluid (Maurice, 2003); Equation 2.2 is the drag force experienced by a particle in a fluid (de Haan and Bosch, 2013):

$$Fc = \frac{\pi}{6} d_p^3 (\rho_p - \rho_l) \frac{C^2}{r^{2n+1}}, \tag{2.1}$$

$$F_D = \frac{18 \mu C_{DR_e}}{\rho_p d_p^2 24}, \tag{2.2}$$

where d_p is the particle diameter, ρ_p and ρ_l are the densities of the particle and liquid, respectively. The C term is a constant and is dependent on the flow regime, r is the radius from the air core, C_D is the drag coefficient and R_e the Reynolds number. The balanced orbit theory uses these two equations to illustrate that larger and higher-density particles will experience a larger radial outward centrifugal force relative to the inward radial drag force. Equation 2.1 also resembles Stokes' law, which has been used to predict particle separation in hydrocyclones by taking into account the effect of centrifugal force (Flintoff and Kuehl II, 2011).

Centripetal forces are radial forces within an inertial reference frame that keep a particle moving around a constant circular path, if present. It is often assumed that the centrifugal force acts in the same manner (in an opposite direction), but this is not true. Centrifugal forces are referred to as 'fictitious' forces, which do not exist in an inertial frame of reference, but only in a rotating (non-inertial) reference frame (Raine, 2017). A centrifugal force within a circular reference frame will make a particle appear to move radially outward, but, from an inertial reference frame, the particle will move in a tangential direction. Therefore, the radial force analysis in Figure 2.3 can only be viewed within a rotating frame of reference and centrifugal forces are limited to this reference frame.

Numerous modern separation mechanisms have been suggested by other authors (Zhang *et al.*, 2017). The most recent understanding of hydrocyclones is based on validated computational fluid dynamic (CFD) models. These models are either based on a discrete force analysis method, such as Lagrangian particle tracking (LPT), that discretely analyses a particle within a fluid, but can only be used for dilute conditions, or on continuum mechanic Eulerian–Eulerian methods that can only handle a narrow feed particle size distribution (PSD). Owing to their respective limitations, these models are often combined and modified to suit a specific application and require validation by experimental results.

Although CFD models are very useful in design, hydrocyclone sizing is more commonly carried out using empirical models, such as those of Plitt and Arterburn, owing to their simplicity and lower computational requirements compared with CFD modelling (Flintoff and Kuehl II, 2011). Empirical models relate the d50 value (diameter at which 50% of particles are cut) to other operational and geometrical variables. It should be taken into account that these models were developed using specific hydrocyclone designs (e.g., the Krebs cyclone, in the case of Arterburn) and a specific slurry, and will not be completely accurate for all types of hydrocyclone designs and applications without the use of correction factors.

2.3.3 Geometry and Concentration Distribution

The solids concentration in a hydrocyclone will vary for each application, but will also differ based on the geometry of the different hydrocyclone components. Figure 2.4 shows the spatial density distribution in hydrocyclones of different scales based on the barrel diameter. The highest solids concentration is at the bottom of the hydrocyclone at the lower cone and spigot in all three cases (Ghodrat *et al.*, 2013). The concentration distribution is also dependent on the PSD and feed pressure. In the case of a coarse PSD (relative to the cut size) and fine cut size, more material will report to the underflow; in the case of higher feed pressure, and subsequently higher flowrate, a build-up of material could occur within the hydrocyclone due to constrained spigot capacity (Zhang *et al.*, 2017).

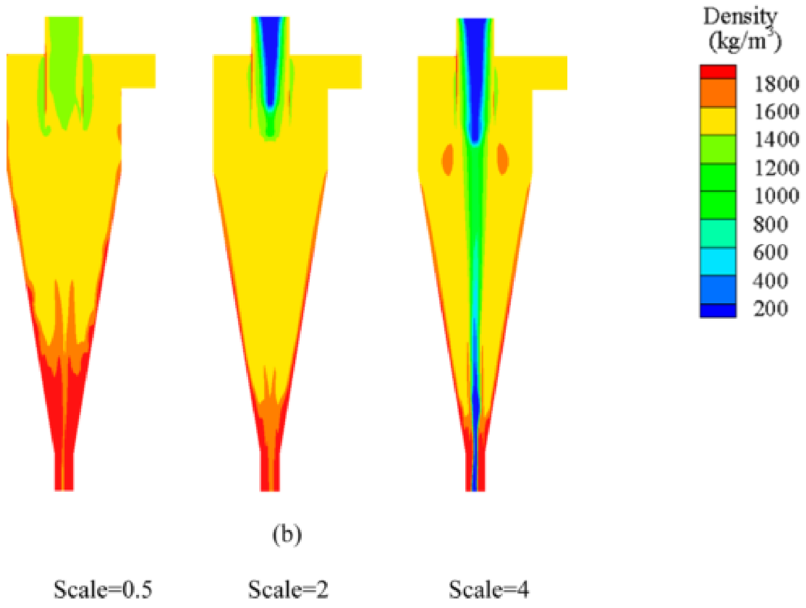

Figure 2.4: Slurry density distribution in different scale hydrocyclones at a solids concentration of 30% by volume, based on two-fluid modelling (Eulerian–Eulerian approach). The three different scales are based on barrel diameters (Dc) of 37.5 mm (scale = 0.5), 150 mm (scale = 2) and 300 mm (scale = 4) (Ghodrat et al.*, 2013).*

The influence of spigot size and its respective cone angle (at a constant barrel diameter) on the concentration distribution is displayed in Figure 2.6 (Ghodrat *et al*., 2013). A smaller spigot and cone will have a smaller volume and surface area compared with a larger cone and spigot, as illustrated by integrating *y* = *f*(*x*) in Figure 2.5. The change in surface area of an infinitesimal section of the hydrocyclone $dS = 2\pi y\ ds$ will decrease with *y* and the slope of *y* = *f*(*x*) is negative towards the bottom of the hydrocyclone, within the Cartesian system as drawn. Therefore, smaller spigots will have higher solids concentrations: a higher particle-to-wall interaction can be expected and, therefore, also a higher level of energy dissipation (Raine, 2017) by friction in this area (Chang *et al*., 2011).

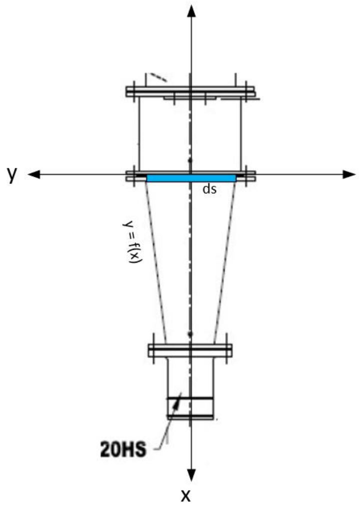

Figure 2.5: Illustration of change in surface area towards the lower end of a 250 mm (Dc) hydrocyclone, with the wall boundary illustrated by y = f(x) *and* ds *being an infinitesimal section of the hydrocyclone.*

Excessively high solids concentrations and feed volumes will lead to roping, in which the shape of the spigot discharge resembles a rope and lacks the presence of an air core. The discharge flowrate will also significantly decrease during roping due to the blocked outlet at the spigot that causes coarse material to short-circuit to the overflow. This phenomenon has a negative impact on separation efficiency (Flintoff and Kuehl II, 2011).

The stage between roping and flaring is referred to as transition discharge (this does not refer to the state where intermittent roping occurs) and is commonly the region in which hydrocyclones are efficiently operated (Schubert, 2010). Within the transition discharge regime, the sediment is mostly concentrated at the wall of the hydrocyclone, as seen in Figure 2.6 when the spigot inner diameter (Du) is equal to 20 mm and 25 mm. The high-density zone is located at the wall of the hydrocyclone and a low-pressure zone (air core) is maintained at the core. Within the flaring and transition discharge regime, the flowrate at the underflow and the feed pressure are significantly higher than when roping occurs.

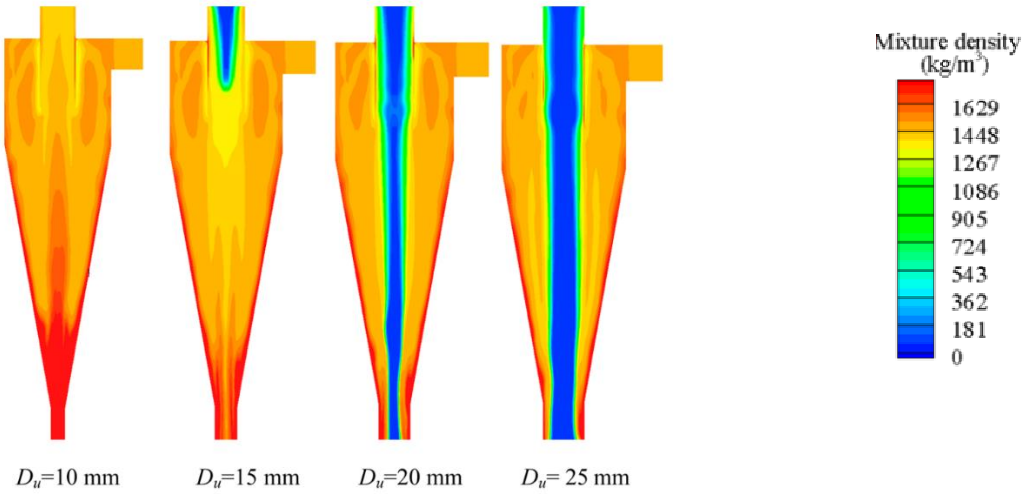

Figure 2.6: Slurry density distribution for different size spigots (Du) at a solids concentration of 30% by volume, based on two-fluid modelling (Ghodrat et al.*, 2013).*

Using positron emission particle tracking of radioactive ^{18}F ions in resin beads, it was observed that the flow orientation and retention time changed throughout the geometry of a laboratory-scale hydrocyclone, as shown in Figure 2.7. It was observed that the helicoidal flow pattern was disturbed at the lower cone due to an end-of-vortex phenomenon (Chang *et al.*, 2011). The retention time of a particle was also found to be higher in this region for this specific hydrocyclone geometry. The higher concentration was evident from the higher particle count in the lower regions of the hydrocyclone, as displayed in Figure 2.7.

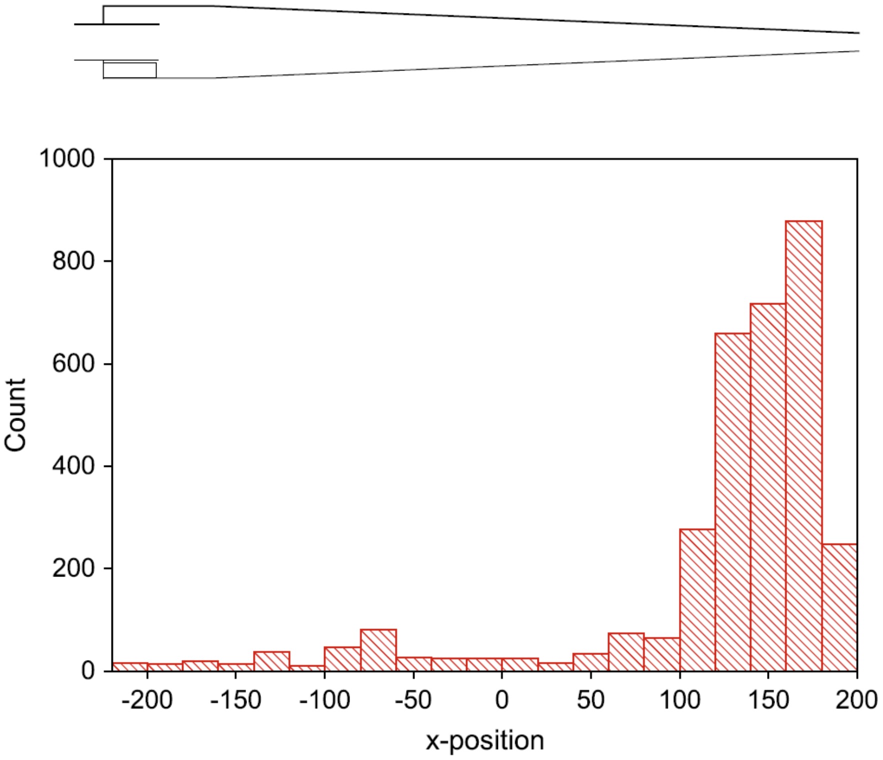

Figure 2.7: Positron emission particle tracking of ^{18}F ions in resin beads of 390 to 700 µm in a 40 mm diameter hydrocyclone operated at 80 kPa (Chang et al.*, 2011).*

2.3.4 Velocity and Energy Distribution

Based on the first law of thermodynamics, energy cannot be created nor destroyed, but only transferred. Furthermore, the total energy of the universe remains constant, which is the sum of the energy of a system and its surroundings. Therefore, if a particle (system) contains a fixed amount of energy (kinetic and potential), the energy can only be lost by energy transfer to its surroundings (Raine, 2017). The magnitude of kinetic energy that a particle possesses is therefore linked to its ability to transfer energy, which leads to wear (Stachowiak and Batchelor, 2014). Kinetic energy is a function of both mass and velocity. Therefore, areas with higher velocity particles can experience a higher degree of wear, as proven by empirical observations (Budinski, 2007a).

The velocity vector of a particle contains three components: the radial, axial and tangential directions. The most practical way to analyse these velocities is by using modelling. The typical tangential velocity profile in a hydrocyclone is shown in Figure 2.8 (Ghodrat *et al.*, 2013). A similar tangential velocity profile was found by Zhang *et al.* (2017).

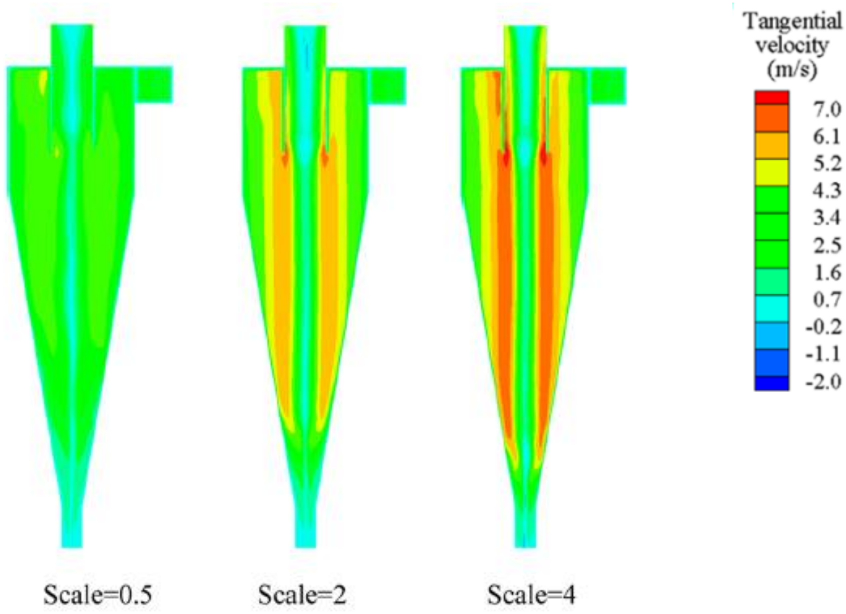

Figure 2.8: Tangential velocity for different size hydrocyclones at a solids concentration of 30% by volume using two-fluid modelling (Ghodrat et al.*, 2013). A similar tangential velocity profile was reported by Zhang* et al. *(2017).*

The tangential velocity was observed to be highest at the vortex finder and decreased radially outward from the air core. Another study found that the tangential velocity decreased axially towards the bottom (spigot), and suggested that this trend is due to higher interparticle interaction at the bottom of the hydrocyclone (Davailles *et al.*, 2012).

The radial forces and velocity distribution are dependent on the particle size and, based on LPT modelling, it was found that larger particles exerted a greater radial outward force at the bottom of the hydrocyclone around the spigot area. Smaller (−25 µm) particles showed a higher radial inward force closer to the core of the hydrocyclone (Zhang *et al.*, 2017). The Reynolds stress model did not show any clear pattern of higher radial velocities at the lower regions of the hydrocyclone, as shown in Figure 2.9(a).

The axial velocity at the wall of the barrel and lower cone remained roughly constant from the top to the bottom of the hydrocyclone based on the Reynolds stress model, as shown in Figure 2.9(b). The axial velocity (magnitude) is much higher at the vortex finder wall than that at the inlet, barrel, cone and spigot walls.

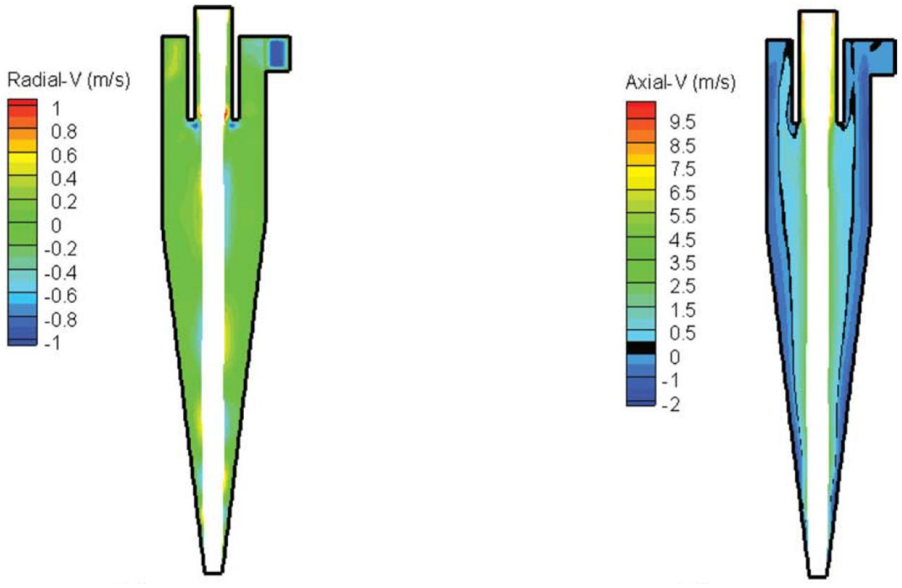

a) b)

Figure 2.9: (a) Radial and (b) axial velocities in a hydrocyclone based on Reynolds stress model (Wang and Yu, 2010).

2.3.5 Hydrocyclone Efficiency

Hydrocyclone efficiency is commonly assessed using a partition curve that plots the recovery of particles to the underflow for different size fractions *i* (*Rec$_i$*). The slope of the partition curve between 75% and 25% recovery to the underflow, normalized to the cut size (d50), is defined as the imperfection (IMP) and is a common way to assess the efficiency of separation. If the IMP value is compared for different operating conditions, the corrected partition curve should be used (Gupta and Yan, 2016). The partition curve is usually corrected to determine the corrected cut size (i.e., the actual cut size) using Equation 2.3. With Rec_i, the actual recovery for a size fraction (also known as the partition factor) and α_w is assumed to be equal to the water recovery to the underflow, if the Kellsal method is used. The α_w value is assumed to be the amount of material in each size fraction that short-circuits to the underflow without being classified and can therefore be used to correct the curve (Gupta and Yan, 2016). The partition curve can also be corrected using a mathematical transformation and by selecting α_w to be the minimum value of recovery to the underflow (Nageswararao, 2016).

$$CorRec_i = \frac{Rec_i - \alpha_w}{1 - \alpha_w} \tag{2.3}$$

Another method to determine the efficiency is by using a model such as that given by Equation 2.4 and evaluating the γ value. The γ term is related to the shape of the partition curve, with higher values related to a sharper cut and a smaller IMP value ($\gamma > 2$ is considered to be efficient). The *di* term is the particle size for the specific Rec_i value and d50$_c$ is the corrected cut size. This model also takes α_w to be equal to the water recovery to the underflow. The corrected curve is determined by removing the α_w terms (Flintoff and Kuehl II, 2011).

$$Rec_i = \alpha_w + (1 - \alpha_w)\left[1 - e^{-0.693}(\frac{di}{d50_c})^{\gamma}\right] \tag{2.4}$$

It has been found, however, that corrected recovery curves do not always produce interpretable results when using the Kellsal method in the presence of the fish-hook effect, due to negative normalization of certain size fractions. The fish-hook effect can be seen in the portion of the partition curve (hydrocyclone efficiency curve) shown in Figure 2.10, where there is higher recovery of ultra-fines to the underflow. The size of the fish-hook is characterized by the difference between the critical point and the dip point δ and the width of the fish-hook (D + C in Figure 2.10).

The fish-hook phenomenon occurs in applications where both large and ultra-fine (below 10 μm) particles are present. A study by Schubert (2010) suggested that interparticle interaction between large and ultra-fine particles caused swarms of ultra-fine particles to follow the large particles due to drag forces in the boundary layer of the larger particles (velocity gradient). The exact mechanism of the fish-hook effect has not been quantified, and there are other theories that relate the phenomenon to Reynolds number effects and turbulent dispersion (Dueck *et al*., 2014). Regardless of the mechanism, the importance of the fish-hook effect is that it diminishes the separation efficiency of ultra-fine particles and should be minimized if possible.

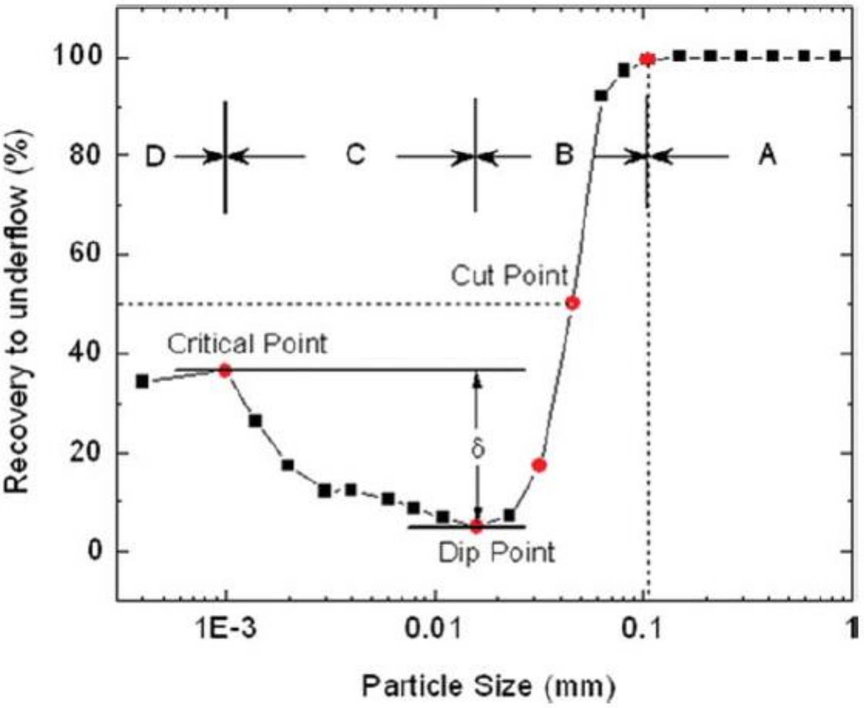

Figure 2.10: Example of the fish-hook effect seen in some hydrocyclone partition curves (Wang and Yu, 2010).

2.4 Overview of Wear

Wear is the mechanism by which a substrate loses mass due to physical interaction between the substrate and other particles, leading to the degradation of atomic bonds (Giltrow, 1970). Wear can broadly be categorized as either erosive or abrasive. Slurry wear occurs specifically when solid particles are suspended and carried using a fluid. The energy of the fluid is transferred to the solid particles in the fluid and the particles, in turn, transfer some of the energy to the substrate by friction or plastic or elastic deformation (Stachowiak and Batchelor, 2014). The two different types of wear are discussed in this section, along with approaches to modelling of erosive wear.

2.4.1 Abrasive Wear

Abrasive wear occurs where a normal force is applied to a grit (particles) that moves over the target material surface. Abrasive wear present in multiphase flows can be referred to as three-body mode because the opposing surface does not exert a direct force on the particles. An illustration of three-body abrasive wear is shown in Figure 2.11. When an opposing force is directly applied to the grit, the abrasive wear would be referred to as two-body mode abrasion, as illustrated in Figure 2.12 (Stachowiak and Batchelor, 2014).

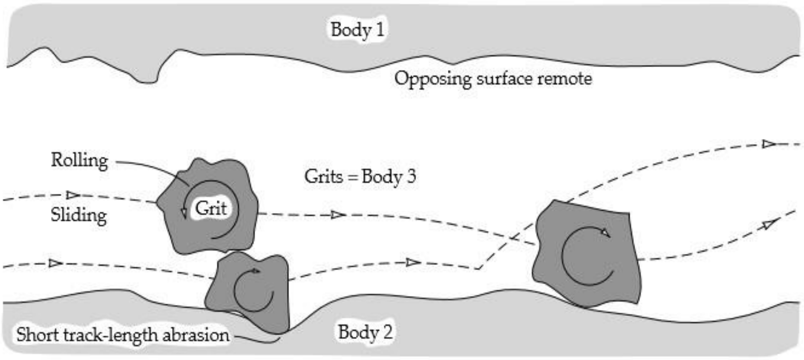

Figure 2.11: Mechanism of three-body abrasive wear (Stachowiak and Batchelor, 2014).

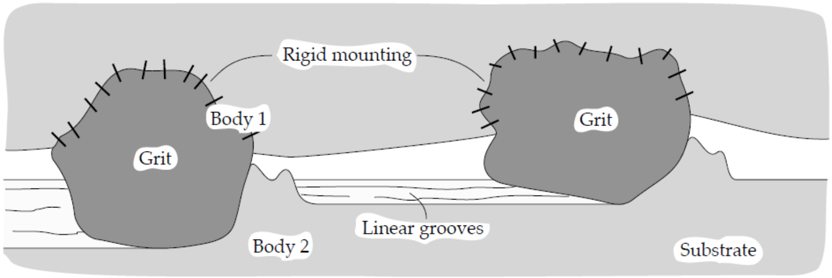

Figure 2.12: Mechanism of two-body abrasive wear (Stachowiak and Batchelor, 2014).

2.4.2 Erosive Wear

Erosive wear occurs when suspended particles in a fluid impact a substrate to cause wear. Different erosion mechanisms can occur, depending on the impingement angle and velocity of the particles. The material properties of the eroded material also play a role. Different erosion mechanisms are illustrated in Figure 2.13 (Stachowiak and Batchelor, 2014). It has been suggested that low-angle erosion will give a wear mechanism similar to that of abrasion.

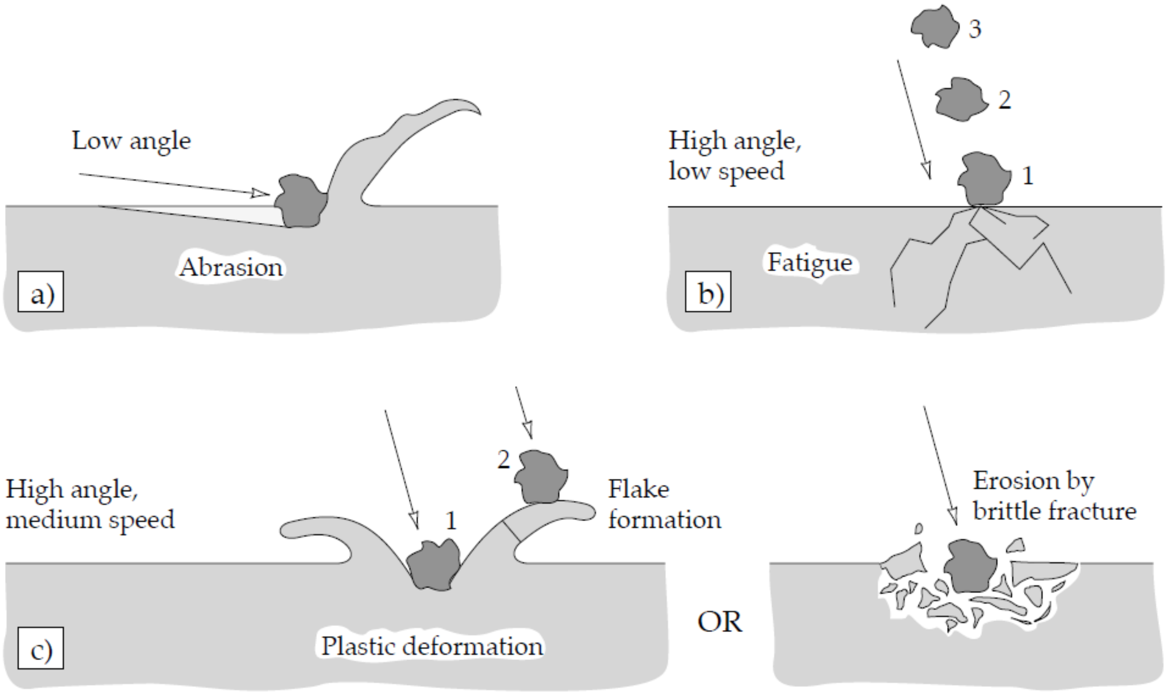

Figure 2.13: Basic illustration of different erosive wear mechanisms (Stachowiak and Batchelor, 2014).

2.4.3 Hydrocyclone Wear

Based on the two main wear mechanisms described above (abrasive and erosive), it is evident that hydrocyclone wear has an erosive wear mechanism, because particles are suspended in a fluid.

Numerous design factors influence the wear rate of hydrocyclones. Attempts have been made to minimize the amount of turbulence and wear at the hydrocyclone inlet by modifying the inlet design (Xu *et al.*, 2009). Furthermore, it has been suggested that tilting a hydrocyclone (~45°) leads to lower wear at the lower regions of the hydrocyclone due to a lower head (Flintoff and Kuehl II, 2011). Mono-cone designs have been used between the lower cone and spigot to minimize geometrical irregularities to minimize wear. In an attempt to achieve homogenous wear rates for the different parts within a hydrocyclone, some original equipment manufacturers use different wear-liner materials in different parts of the hydrocyclone to compensate for the higher wear rates at the spigot and lower cone. The operational effect of wear on a hydrocyclone may include lower relative density (RD) values encountered at the underflow due to spigot wear. In addition, it was suggested that wear grooves in the lower cone could lead to misplacement of coarse particles to the overflow. Replacing one component in a hydrocyclone that has been worn out, such as the lower cone, while keeping the old cone could also potentially worsen separation performance due increased turbulence (Olson and Turner, 2002).

The factors influencing hydrocyclone wear can be broadly listed in four categories: feed properties, particle properties, cyclone material and cyclone geometry, as listed in Table 2.2. These factors are mainly derived from an empirical slurry erosion model given by Equation 2.5 (Budinski, 2007a):

$$W \approx C_1\left[\left(\frac{MV^a dD}{E}\right)f(\theta)\right] + C_2, \qquad (2.5)$$

where *W* is the erosion rate, *M* is mass of particles per unit of fluid, *D* is density, *V* is fluid velocity; *d* is particle diameter, θ is the impingement angle, *E* is a property of the target material, C_1 is a friction constant, C_2 is a constant dependent on the slurry properties and *a* is the velocity exponent.

Equation 2.5 gives the erosion rate, where *W* (*dm*/*dt*) is the change in mass of the substrate over a specific time. This simple erosion model requires two constants that need to be empirically determined. It is an empirical equation that gives an indication of factors that can influence the erosion rate of a substrate.

Table 2.2: Factors that influence cyclone wear (from Budinski, 2007a).

Factor	Influence (Description)
Feed properties	Fluid velocity and pressure (pump speed, flowrate, RD)
	Concentration (solids concentration of feed)
	Chemical properties (pH, composition)
	Impingement angle (angle of attack on hydrocyclone)
Particle properties	Particle hardness
	Particle size
	Particle shape and friability.
	SG
Cyclone material	Material properties (measured)
	Chemical properties (composition and microstructure)
Cyclone geometry	Size and shape (e.g., inlet type, curvature, design)

Modelling hydrocyclone wear using CFD and discrete element analysis has been attempted (Azimian and Bart, 2016), but did not give results that accurately correlated with actual wear profiles, where it was found that the spigot (highest) and lower cone (second-highest) experience the most wear (Olson and Turner, 2002). Figure 2.14 shows that the model predicted that the connection point between the upper part of the cone and the barrel would experience the most wear, which was not the case; therefore, it is first required to obtain sufficient empirical data prior to modelling of wear.

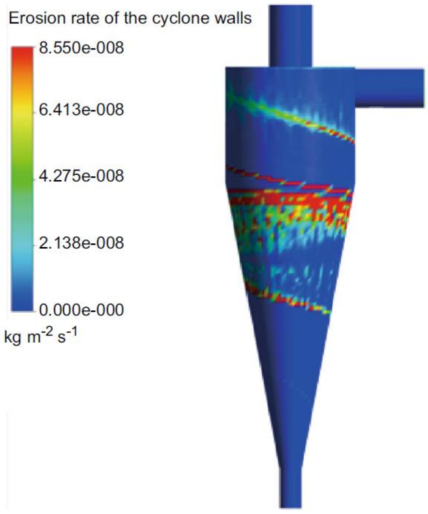

Figure 2.14: Erosion rate spatial distribution model based on a Euler–Lagrange computational fluid dynamics model (Azimian and Bart, 2016). Note that the model was not properly validated by empirical wear rates in the different zones of a hydrocyclone.

2.5 Laboratory Wear Test Methods

Measuring hydrocyclone wear in-situ in an industrial application is the most representative method of analysing hydrocyclone wear, but this method is not always available due to logistical or practical constraints. A pilot-scale hydrocyclone test setup can also be used to recirculate feed material to produce and analyse wear. This method has the disadvantage of potentially taking more time to produce wear due to smoothing of the particles during feed recirculation (see Figure 2.42) (Miller and Schmidt, 1987), but is more representative than laboratory-scale methods.

Laboratory-scale tests have the advantage of producing wear within minutes or hours under controlled conditions. Discussion of the following test methods is aimed at reviewing laboratory-scale methods that could be used to simulate hydrocyclone wear. The test methods discussed are the Miller test (ASTM G75), jet erosion test (ASTM G 76), slurry pot test (ASTM G119), Coriolis test, abrasion wheel test (ASTM G65), rotary drum abrader test (ASTM D5963) and the slurry jet erosion (SJE) test. Specific details of these tests are presented in Appendix A.

According to the American Society for Testing and Materials (ASTM) guidelines, selection should be based on which test method best simulates the conditions and wear mechanism found in practice (ASTM International, 2015b): in this case, hydrocyclones. Other (standard and non-standard) test methods are also subsequently required to empirically quantify the wear rate of materials under different wear conditions.

2.5.1 Miller Test (ASTM G75)

The Miller machine, shown in Figure 2.15, is used in a three-body test that uses abrasion to produce wear. The sample is reciprocally moved through the slurry for 6 h before measuring the mass loss (ASTM International, 2015c).

The Miller test is commonly used to determine the Miller number of a slurry and indicates the abrasivity of the particles. The Miller number is determined using a 27% chrome cast iron sample. The Miller machine is also used to determine the slurry abrasivity resistance number (SAR): in this case, the slurry is kept constant and the sample material is changed to measure the relative wear resistance. The Miller number is useful for quantifying the abrasiveness of a specific ore in general applications, but the test is primarily an abrasion test and not an erosion test.

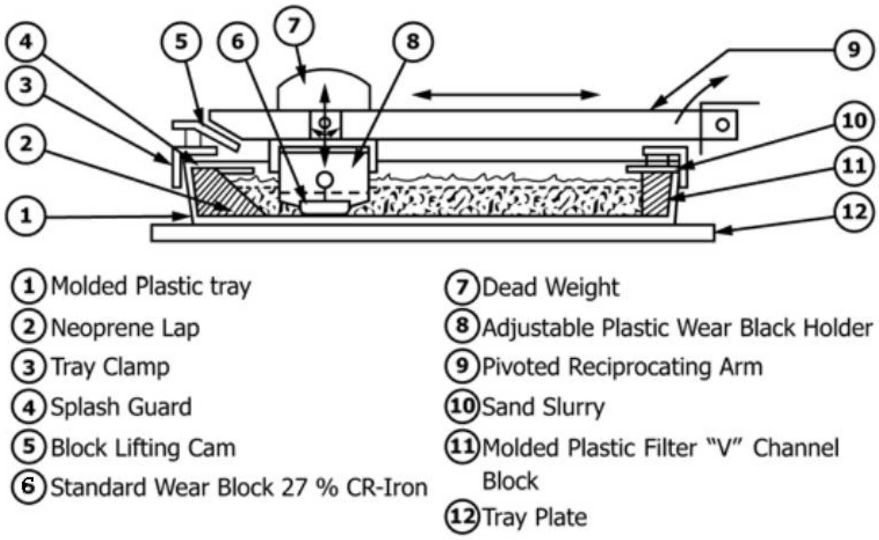

Figure 2.15: Miller abrasion tester (ASTM International, 2015c).

2.5.2 Jet Erosion Test (ASTM G76)

The ASTM G76 jet erosion test is a solid particle impingement test that uses gas as the fluid. The setup for this test is shown in Figure 2.16 and is based on high-speed erosive wear. This test, unfortunately, has a few drawbacks: it needs 2 g/min aluminium oxide in a gas stream, which leads to a complex setup to control, and it requires measurement of the velocity of the particles, which can be cumbersome (Budinski, 2007b). A fundamental drawback is the fact that the carrier fluid is air; therefore, this cannot be defined as a slurry erosion test.

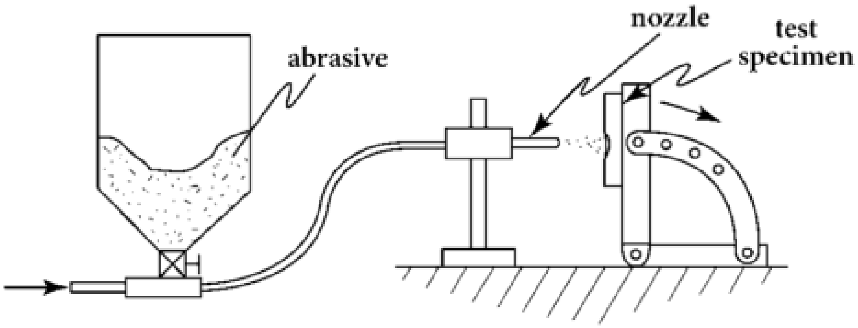

Figure 2.16: Apparatus for ASTM G76 jet impingement test (Budinski, 2007b).

2.5.3 Slurry Pot Test (ASTM G119)

The ASTM G119 slurry pot test equipment consists of a pot, impeller and motor. Specimens are immersed in and rotated through the slurry on the impeller sample holders. The impeller speed must be controlled as specified by the standard.

The test is conventionally carried out using a batch of slurry that is not replaced during the test, although use of a continuous feed of fresh slurry would be more accurate. This, however, requires a much larger experimental setup, and, for some materials, the time required might make this option unpractical (Budinski, 2007b). This method is a popular slurry erosion test, and various researchers (Gupta *et al*., 1995; Desale *et al*., 2006) have used this test method to measure the wear and corrosion resistance of materials. This test also allows the impact velocity, impingement angle and slurry concentration to be adjusted.

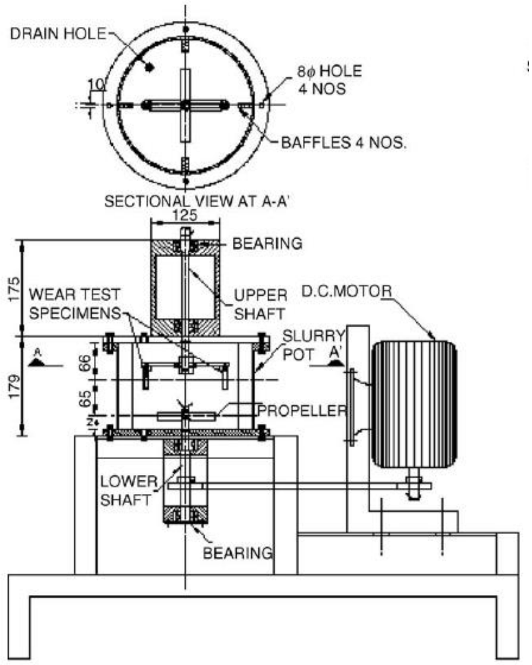

(a) Pot tester assembly

Figure 2.17: Setup for a slurry pot tester (Desale et al.*, 2006).*

2.5.4 Coriolis Test

The Coriolis test is a rotating slurry test that was designed to simulate conditions within slurry pumps and cyclones (Llewellyn *et al*., 2004). The Coriolis test device is illustrated in Figure 2.18, which includes a free-body diagram of the forces acting on the specimen.

Slurry enters the device through a pipe while the samples are rotated. The particles exert centrifugal and Coriolis forces on the specimen. The centrifugal force acts in an outward radial direction relative to the rotation centre and parallel to the wear groove, and the Coriolis force acts against the sidewall in an angular direction, as shown at the bottom of Figure 2.18. [It should be noted that the Coriolis and centrifugal forces are ‘fictitious’ forces and only exist in a rotating frame of reference (as viewed from the rotating specimen holder).] This test allows the particle velocity and feed concentration to be adjusted, but does not allow the impingement angle to be adjusted and only operates at low impingement angles (< 5°).

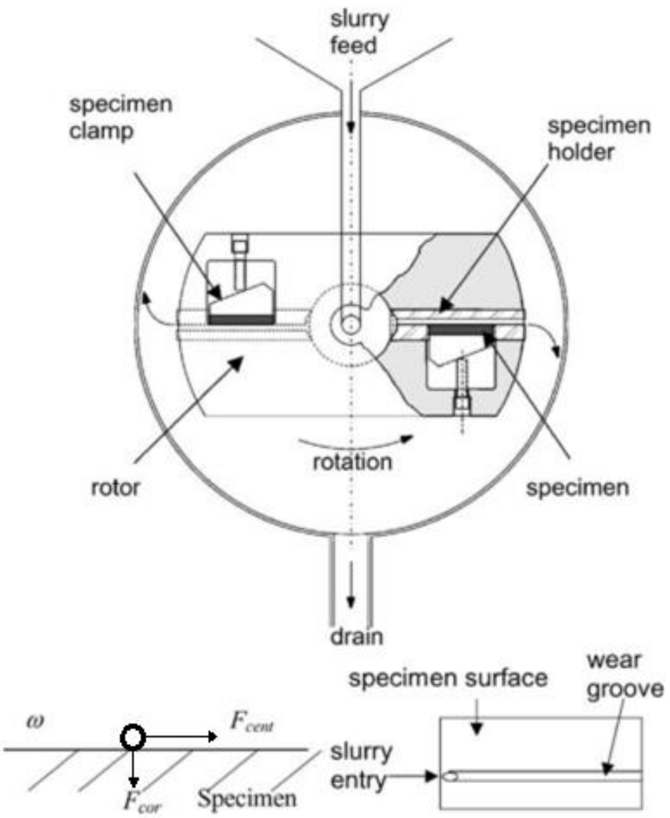

Figure 2.18: Coriolis rotating slurry test (Llewellyn et al.*, 2004).*

2.5.5 Abrasion Wheel Tests (ASTM G65)

The sand and rubber wheel test, ASTM G65, shown in Figure 2.19(a), is used to simulate three-body abrasion. This is a dry abrasion test and there is no fluid present (Budinski, 2007b). This test is sometimes used to test the abrasion resistance of screen panels. It is important to note that ASTM G65 is carried out over a much longer time interval than the more commonly cited rotary drum abrader test, Figure 2.20, ASTM D5963 (ISO 4649-A), because the wear rate is lower (refer to Table E.1 in Appendix E).

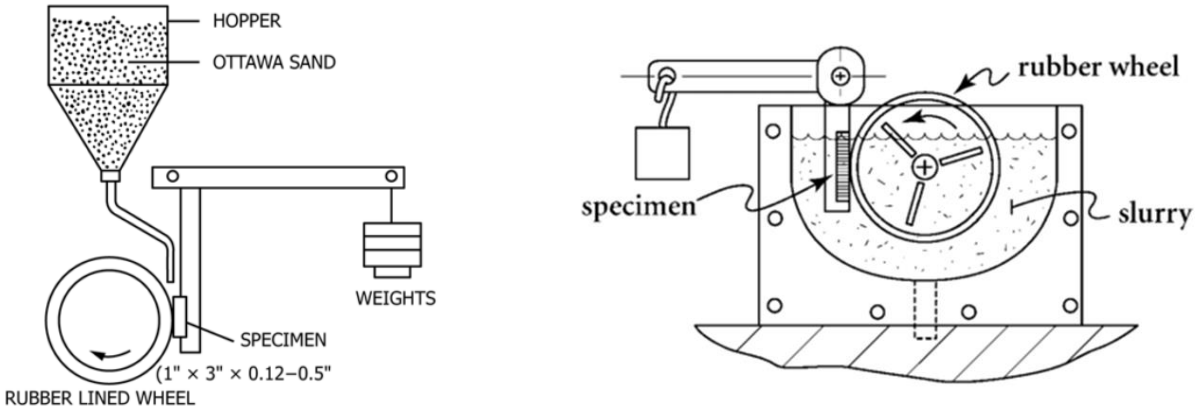

a)

b)

Figure 2.19: (a) ASTM 65 sand and rubber wheel test (ASTM International, 2016b) *and (b) ASTM G105 wet abrasion test (Budinski, 2007b).*

A slightly modified version of this test is given by ASTM G105, which uses a slurry instead of a dry feed material, as shown in Figure 2.19(b). Both the ASTM G65 and G105 methods use a feed of 212–300 µm rounded quartz sand (ASTM International, 2016a). These tests do not measure the abrasivity of different slurries, but are used to compare the wear resistance of different materials. The drawback of these tests is that they do not test the effect of particle properties and the possibility that the relative wear rate of materials may change depending on the slurry application. This phenomenon is seen in the minerals processing industry, where different materials are recommended for different applications based on the properties of the slurry.

2.5.6 Rotary Drum Abrader Test (ASTM D5963)

The rotary drum abrader test, specified by ASTM D5963 (ISO 4649-A) and shown in Figure 2.20, is very commonly used for polymer quality assurance (Budinski, 2007b). The test is based on the principle of two-body abrasion and is a dry abrasion test with no slurry present. [Materials abrasion resistance is commonly cited in material suppliers' product catalogues as the abrasion resistance.] The time duration of this test is relatively short: the sample is abraded for a total distance of 40 m and then stopped (ASTM International, 2015a). It is clear that the wear mechanism in this test differs significantly from that experienced in slurry erosion applications.

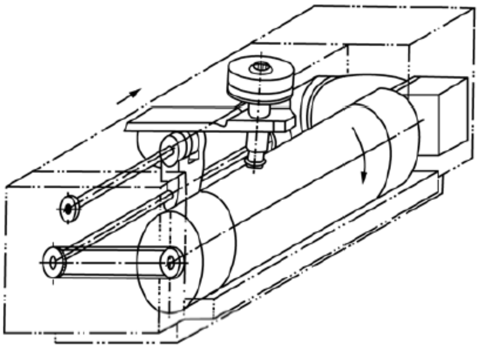

Figure 2.20: Rotary drum abrader (ASTM D5963, also known as ISO 4649-A) (ASTM International, 2015a).

2.5.7 Slurry Jet Erosion Test

The SJE tester, displayed in Figure 2.21(a), was developed by the National Research Council of Canada (Zhang *et al*., 1995) to specifically test the wear resistance of materials in slurry erosion conditions. The device recirculates feed material at a set RD and pumps the slurry into the sample at a set impingement angle and velocity (Xie *et al*., 2015). This test has the same challenge as the slurry pot test, in which the material is recirculated and changes shape due to attrition. This test gives a better representation of slurry erosion compared with that of the jet impingement test shown in Figure 2.16, which does not use a slurry. This test has also been modified by mounting the sample in a circular tube-like setup, shown in Figure 2.21(b), in which the slurry passes over the specimen in a circular motion to produce centrifugal forces (Zhang *et al*., 1995).

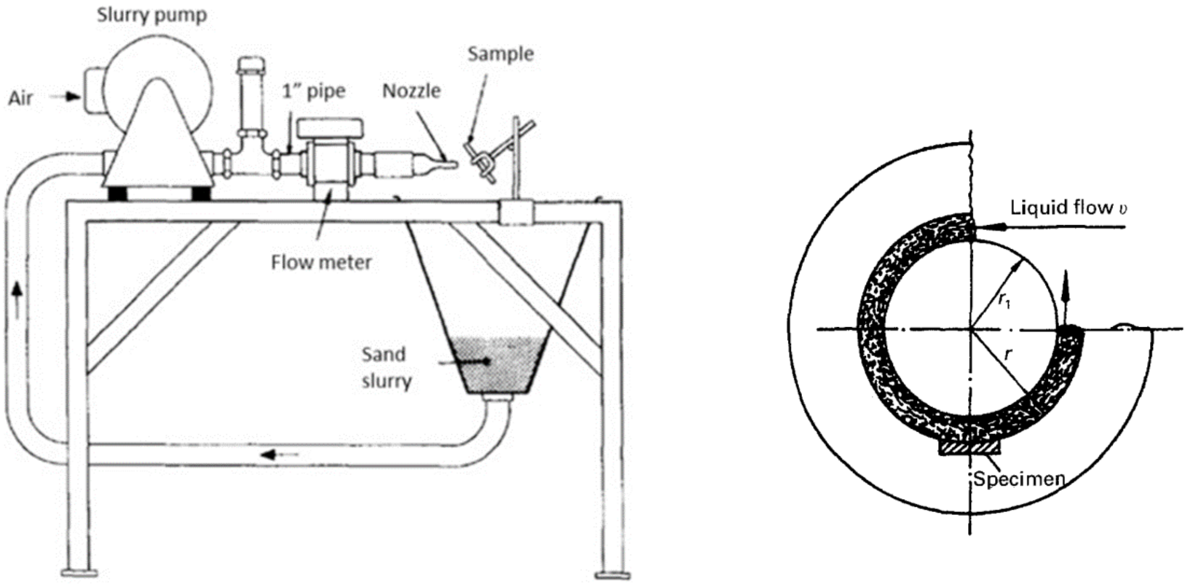

a)

b)

Figure 2.21: a) Slurry jet erosion test developed by the Canadian National Research Council (Xie et al.*, 2015). b)* Modified slurry jet erosion sample mounting setup *(Zhang* et al.*, 1995).*

2.5.8 Test Selection Summary

It often appears that material selection is based only on the mechanical and material properties of the material of construction, and that wear resistance is based on the cited abrasion resistance value (ASTM D5963 wear value is commonly cited: refer to Table E.1 in Appendix E). The consequence is that selection is based on the assumption that there is a strong relationship between abrasion resistance and erosion wear resistance in slurry wear applications, which is, in fact, not the case for most materials because wear mechanisms are complex and application-specific (Stachowiak and Batchelor, 2014; Budinski, 2007b).

Table 2.3 can be used to assess the test methods mentioned above to determine whether a test can be used to simulate the conditions and wear mechanism found in hydrocyclones, as required by the selection requirements of the ASTM guidelines (ASTM International, 2015b).

Table 2.3: Summary of wear test methods, showing adjustable factors and type of test.

Test method	Erosive wear	Abrasive wear	Slurry relative density	Particle velocity	Impingement angle adjustment	Particle properties
Miller		✓	✓			✓
Jet erosion	✓			✓	✓	
Slurry pot	✓		✓	✓	✓	✓
Coriolis	✓		✓	✓		✓
Abrasion wheel		✓				
Wet abrasion wheel		✓	✓			
Drum abrader		✓				
Slurry jet erosion	✓		✓	✓	✓	✓

Based on the comparison given in Table 2.3, the most suitable standard test methods would be the SJE, Coriolis and slurry pot tests. A drawback of these tests is smoothening of the slurry particles that would occur if they are recirculated. Final test selection should be based on the wear surface morphology produced by each test and whether the test creates a wear surface that resembles that produced within hydrocyclones (ASTM International, 2015b). Unfortunately, due to limited equipment availability, this study was only able to make use of the drum abrader test: a pilot-scale test rig was constructed to produce wear according to this test method.

2.6 Wear of Hydrocyclone Materials

Factors that influence materials selection for hydrocyclones are discussed in this section, along with the relationship between material properties and wear of metals and polymers.

2.6.1 Wear-Resistant Materials

In the case of hydrocyclone materials selection, it is important to understand the application in which the hydrocyclone will be used and how critical the application is before making materials recommendations (Holmberg *et al.*, 2017). Material selection will then be based on a trade-off between the cost of the material and its wear life. Table 2.1 listed some such hydrocyclone applications.

Materials that are commonly used in cyclone and hydrocyclone wear applications are listed in Table 2.4, with comments on each and its relative price.

When selecting a hydrocyclone material, not only should the initial capital cost of each potential material be compared, but the indirect total cost over the lifetime of the operation, which includes maintenance down-time, wear life, replacement cost and potential losses due to inefficiency caused by wear (Cortie *et al.*, 1996). It is important to understand the relationship between materials properties and wear, because the properties are evaluated for optimal material selection. It is, however, suggested to always supplement materials properties selection with a suitable empirical wear test method, as discussed in Section 2.5.

Table 2.4: Material classes typically used for hydrocyclones (Multotec Employees 2018, personal communication).

Material	Comment	Relative price (est.)
(Poly)urethane	The least expensive option in most cases. Size limitation, otherwise reinforcement steel required (usually does not exceed Dc of 350 mm). Used for all applications.	Low – Medium
Rubber	Replaceable liners make maintenance much easier. Typically used in classification cyclones with linings in steel/cast iron/polyurethane shell.	Medium – High
Ceramics	Typically used in classification cyclones and DMS applications.	Medium – High
Metals	Can be used without a liner if the metal has a high wear resistance or if the application is not highly erosive. Typically (27% chrome cast iron) used in cyclone applications.	Medium – High

2.6.2 Manufacturing and Defects

The manufacturing methods of hydrocyclones are dependent on the material of construction and are summarized in Table 2.5. Quality control and defect mitigation are of importance in wear applications because defects could lead to accelerated wear.

Defects can be either geometrical or chemical in nature. Defects present in the manufacturing of NR are commonly related to the mixing, vulcanization and compression-moulding process. NR can be of varying levels of purity and is naturally not a completely homogenous material. The distribution of sulfur (used for vulcanization) can also vary, due to incomplete mixing or incorrect temperature and time control during curing, leading to incomplete cross-linking during vulcanization. Localized soft spots can occur due to a deficiency of sulfur or an uneven temperature distribution over complex material geometries. An example of a soft-spot defect is shown in Figure 2.2. Filler materials are also used and can lead to variations in mechanical properties over the material if not mixed homogenously (Clavier, 2008). Void formation can occur due to non-optimal sprue or flash design. The shape and position of the preformed uncured rubber needs to allow air to escape during compression. The viscosity of the rubber during compression moulding should also have an optimal value to minimize void formation and ensure complete filling of the mould (Ciesielski, 1999).

In the case of hand-cast thermosetting polyurethane, it is very important to avoid defects by using the correct casting technique, mixing ratio and temperature (Clavier, 2008). The extent of void formation in hand-cast parts is a function of the pouring technique, cleanliness of the mould, temperature, viscosity, reaction temperature (exothermicity of the reaction) and the mould design. Some other defects that can occur during polyurethane hand-casting are summarized in Table E.5 in Appendix E.

Defects that occur in thermoplastic PU injection moulding include short moulding, void formation, flow marks, sink marks and the possibility of cured stock entering a new part due to unremoved solidified parts in the runners or sprues.

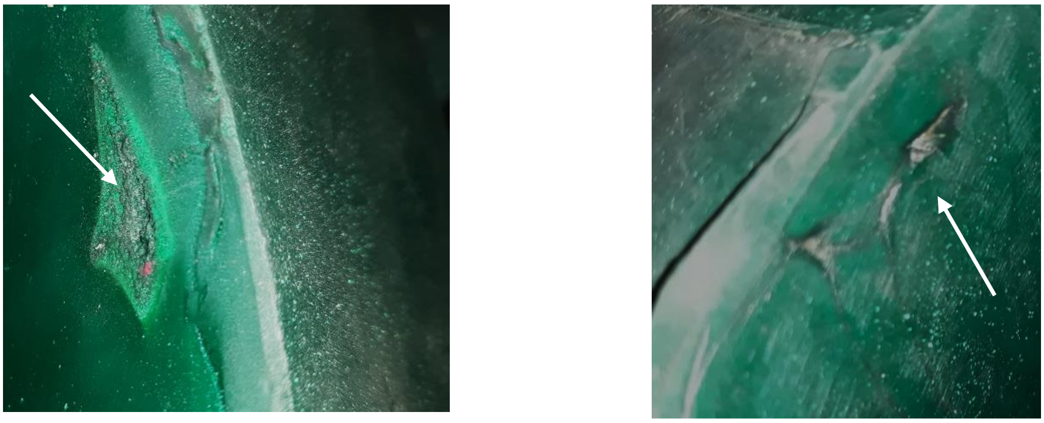

Figure 2.22: Images of a soft spot near the edge of the cone of a compression moulded and vulcanized natural rubber compound lining (Combrink, 2018).

Table 2.5: Selected engineering materials used in cyclones/hydrocyclones and their respective manufacturing method (Multotec Employees 2018, personal communication). Other manufacturing methods and materials are also available.

Component	Material	Manufacturing method
Vortex finder	Thermoplastic polyurethane	Injection moulding/ hand-cast
	Thermosetting polyurethane	Hand-cast
	Ceramic tiles	Tiling of steel shell
	Cast iron (high alloy)	Casting
Feed cylinder	Natural rubber	Compression mould, vulcanize, glue
	Thermoplastic polyurethane	Injection mould
	Thermosetting polyurethane	Hand-cast
	Ceramic tiles	Tiling of steel shell
	Cast iron (high alloy)	Casting
Upper cone	Natural rubber	Compression mould, vulcanize
	Thermoplastic polyurethane	Injection mould
	Thermosetting polyurethane	Hand-cast
	Ceramic tiles	Tiling of steel shell
	Cast iron (high alloy)	Casting
Lower cone	Natural rubber	Compression mould, vulcanize
	Thermoplastic polyurethane	Injection mould
	Thermosetting polyurethane	Hand-cast
	Ceramic tiles	Tiling of steel shell
	Cast iron (high alloy)	Casting
Spigot	Natural rubber	Compression mould, vulcanize
	Thermoplastic polyurethane	Injection mould
	Thermosetting polyurethane	Hand-cast
	Ceramic	Fired ceramic
	Cast iron (high alloy)	Casting

2.6.3 Metals

Metals are widely used as a material of construction for both DMS cyclones and hydrocyclones. The wear-resistant metals typically used for slurry wear applications are white cast irons (Llewellyn et al., 2004).

Erosive wear mechanisms of metals can involve corrosion, fatigue and plastic deformation. Corrosive wear occurs when a corrosion reaction takes place and forms a passivating film on the surface of the substrate. The film is then eroded at an accelerated rate due to its inferior mechanical properties relative to those of the parent metal. Fatigue wear can occur by repeated impingement of abrasive material, which can lead to micro-crack propagation caused by shear forces on the surface of the substrate (Stachowiak and Batchelor, 2014). The erosive wear mechanism will also be a function of the substrate material and particle properties. For ductile metals, sharper erodent particles lead to a cutting-wear mechanism, whereas rounder particles lead to micro-ploughing (Desale *et al*., 2006). The two basic mechanisms by which metals typically resist wear are illustrated in Figure 2.23. Some metals have a high resistance to permanent deformation (high hardness and Young's modulus). The applied stress of an eroding particle can typically be too low to cause any significant deformation or cause very low deformation within the elastic limit of the material. Hardness is, however, not always the property associated with high wear resistance; another important material property that should be considered is toughness. Toughness is typically related to the K_{IC} (plane strain fracture toughness) value and cracking resistance (Stachowiak and Batchelor, 2014).

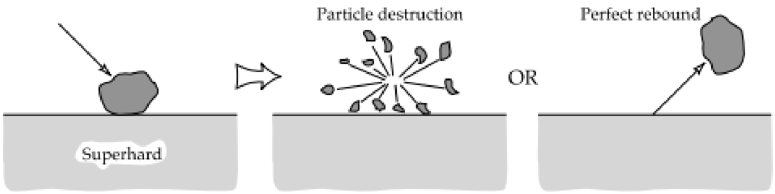

Figure 2.23: Basic wear-resistance mechanisms of metals (Stachowiak and Batchelor, 2014).

In slurry wear applications, metals also need adequate corrosion resistance. Stainless steel has very good corrosion resistance, but lacks the wear resistance offered by white cast irons, such as hypoeutectic white iron (27% Cr, 3%C; ASTM A532) and high chrome (35% Cr, 5%C) hypereutectic white iron (Llewellyn *et al*., 2004).

Attempts have been made to relate metal hardness to wear resistance: some results are shown in Figure 2.24. No linear trend can be established between hardness and wear resistance between different types of metals: hardness can either increase or decrease erosive wear resistance, depending on the impingement angle. For mild steel, an increase in hardness can lead to higher erosive wear resistance at a low impingement angle, but higher hardness values have a negative effect at a high impingement angle, as shown in Figure 2.24 (Stachowiak and Batchelor, 2014). Hardness is therefore not the primary property that should be considered when selecting a metal for slurry wear applications (Jafari *et al*., 2018). This observation was confirmed by Moore, who showed that the microstructure is more important to consider than hardness (Moore, 1974).

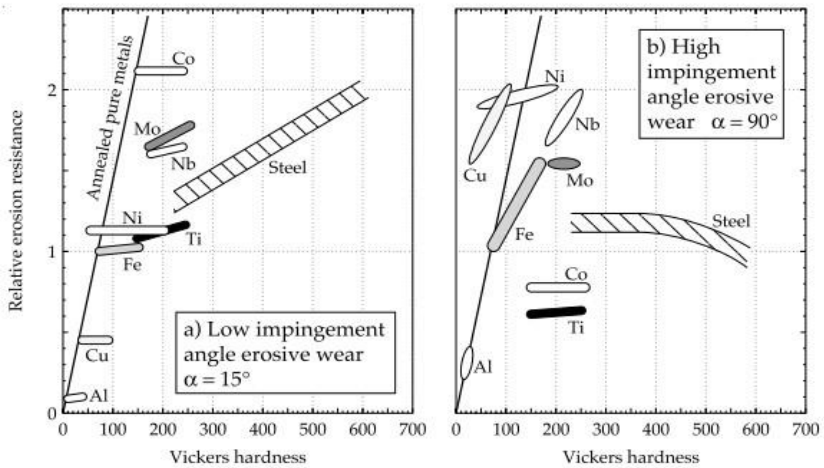

Figure 2.24: Erosive wear resistance based on the results of a jet erosion test using silicon carbide at two different impingement angles for various metals (Stachowiak and Batchelor, 2014).

SJE wear resistances of different metals and elastomers are compared in Figure 2.25(a) at three different impingement angles. Different metal alloys had different responses to the impingement angle: the 35% Cr 5%C and 27%Cr 3%C white irons both experienced the highest erosion rate at 90º, whereas AR400 and martensitic stainless steels showed the highest erosion rate at 45º (Xie *et al*., 2015). The wear profile produced on a metal will differ based on the angle of attack in this test, as illustrated in Figure 2.25(b). A lower impingement angle leaves a longer elliptical wear groove compared with higher angles. The angle of attack at which the erosion rate will be the highest will therefore not only be dependent on the erodent properties, but also on the type of metal (Desale *et al.*, 2006). This is discussed further in Section 2.7.4. This observation highlights the need to individually test or evaluate wear rates of metals for each slurry wear application (Stachowiak and Batchelor, 2014).

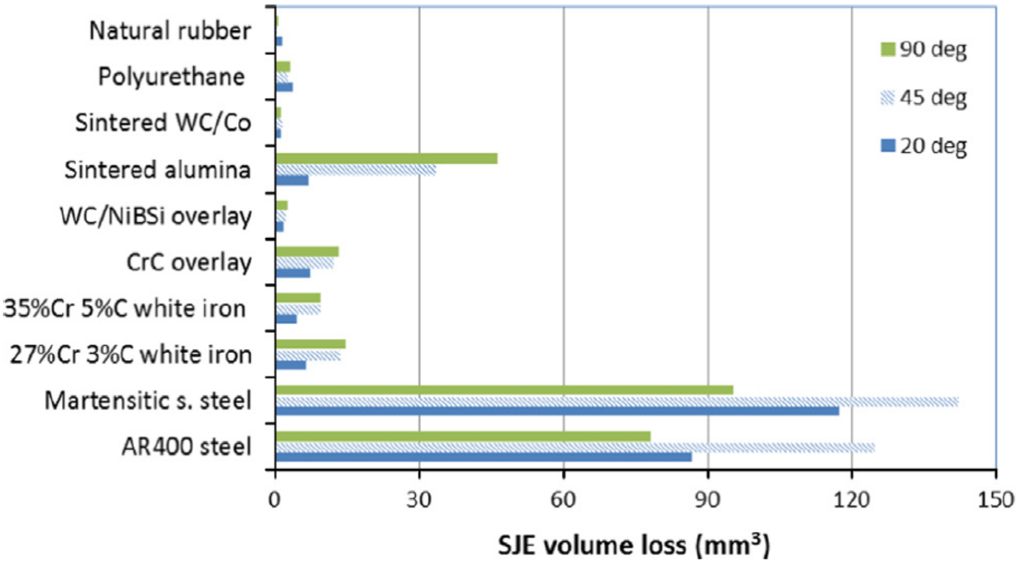

(a)

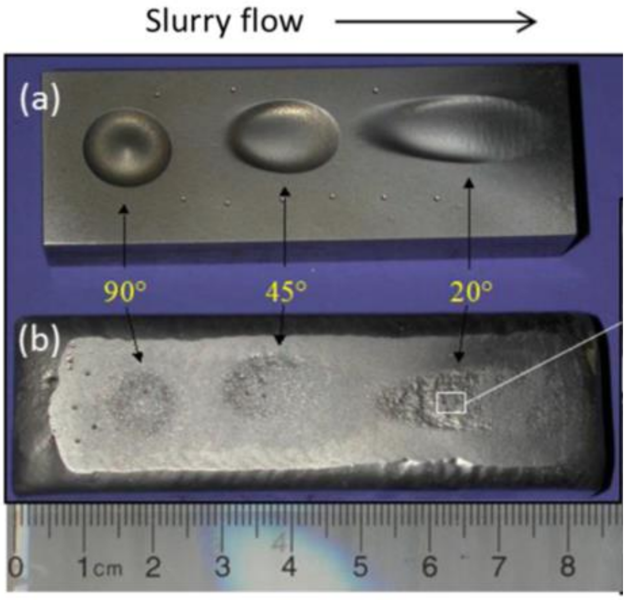

(b)

Figure 2.25: (a) Results of slurry jet erosion test carried out at 16 m/s for 2 h on various wear-resistant materials using silica feed (abrasive) material with a particle size of 212–300 μm and semi-round shape. (b) Slurry jet erosion test wear grooves on (a) low-carbon steel and (b) Tungsten Carbide-MMC overlay at different impingement angles (Xie et al.*, 2015).*

2.6.4 Polymers

Polymers comprise a very large group of materials that consist of a macro-molecule containing a very large number of atoms bonded in a repetitive pattern. Polymers include both rubber and PU (the hydrocyclone materials investigated in this study). Polymers can be created with a wide range of material properties, based on their composition and manufacturing methods used, and can be either elastomeric or non-elastomeric. The use of polymers in slurry wear applications is very popular due to their excellent wear resistance compared with that of other materials used for slurry transport, as shown in Figure 2.25(a) (Xie *et al*., 2015).

There is a wide range of blends and types of rubber available, which can be classified as either natural (vulcanized, compounded) or synthetic. Vulcanized NR has remained a popular erosive wear lining due to its good wear resistance compared with that of most synthetic rubber alternatives, as shown in Figure 2.29 (Arnold and Hutchings, 1991). NR is typically used in a metal hydrocyclone (the shell) as a replaceable wear lining. Both synthetic and natural rubbers are elastomers due to their ability to be greatly elastically deformed.

PU is a popular engineering material due to its ease of manufacturing and relatively low cost compared with that of other engineering materials. PU and urethane are therefore commonly used to manufacture hydrocyclones. PU hydrocyclones are manufactured using either thermosetting PU or thermoplastic polyurethane (TPU). TPU is used in solid (reacted) pelletized form before being melted and injection-moulded or extruded into its final shape. There are three classes of TPU: polyester TPU, polyether TPU and polycaprolactone TPU. Hydrocyclones are typically made of polyether TPU due to its good physical properties and resistance to hydrolysis. Thermosetting PU is formed by two liquid components: a polyol and an isocyanate component. These components react in the presence of heat to form a cross-linked structure during curing that is chemically irreversible. The type of polyol and isocyanate used will determine whether the PU is elastomeric or not. A PU that is considered to be an elastomer needs to have Young's modulus and elongation-at-yield values similar to those of NR or synthetic rubbers.

The basic erosive wear mechanism of polymers (both PU and rubber) can involve ploughing (plastic deformation), gouging (immediate micro-cracking) and/or surface fatigue, depending on the particle properties and feed conditions (Zhang *et al*., 2015). Polymers can also be prone to chemical attack under certain conditions, which can lead to chemical bond degradation and accelerated wear.

Gouging occurs when a relatively large piece of the elastomer is cut by a sharp and often larger particle (+1 mm) (Xie *et al*., 2015), as illustrated in Figure 2.26. Softer elastomeric polymers can typically be more sensitive to gouging by large particles and would require good gouging resistance if used in certain abrasive environments with large sharp particles (Xie *et al*., 2019). Surface fatigue occurs over time and cracks propagate due to cyclically applied localized stress that is caused by impinging of more spherical particles, as illustrated in Figure 2.26.

Wear and manufacturing defects can lead to surface irregularity, as illustrated in Figure 2.27. This irregular surface can be compared with a notch with a higher stress concentration in that localized area. The higher stress concentration, in turn, leads to a lower stress required for crack propagation by gouging and surface fatigue (Arnold and Hutchings, 1991).

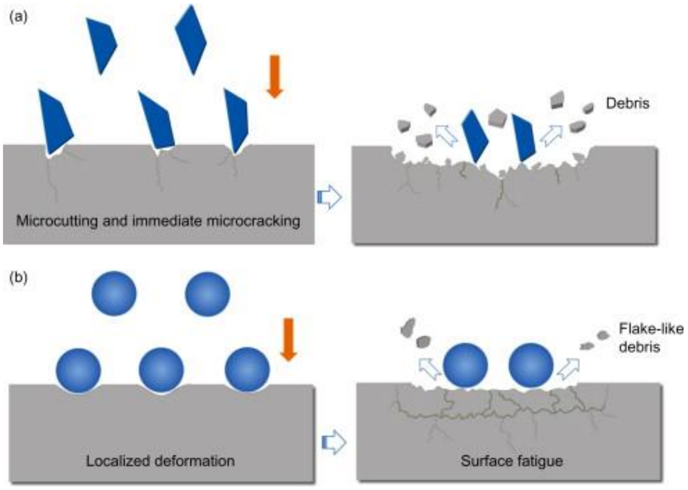

Figure 2.26: Erosive wear mechanism of polymers: (a) surface fatigue, (b) micro-cutting (Zhang et al*., 2015).*

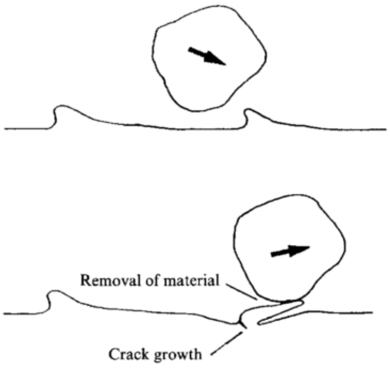

Figure 2.27: Material removal mechanism of an elastomer at low angles (Arnold and Hutchings, 1991).

It has been proposed that elastomeric polymers resist erosive wear by the basic mechanisms illustrated in Figure 2.28. This mechanism is based on elastic recovery, energy absorption and deflection within the elastic limit of the material (Stachowiak and Batchelor, 2014).

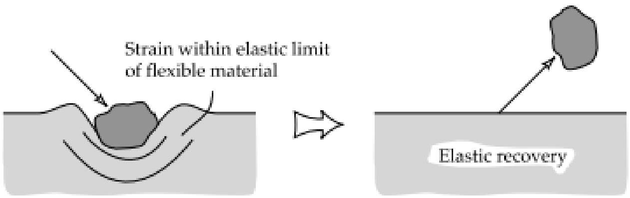

Figure 2.28: Schematic showing how elastic materials resist erosive wear (Stachowiak and Batchelor, 2014).

Polymer materials are rarely harder than the particles flowing within a slurry, yet Figure 2.25 shows that certain polymers have much better erosion resistance than steel. The main reason for this is the ability of elastomers to elastically deform much more than metals. Elastomers are designed to have an extremely high modulus of resilience (see Equation 2.6). This property makes these materials very wear-resistant relative to their hardness. The relationship between polymer hardness and erosion resistance for various polymers is compared in Figure 2.29.

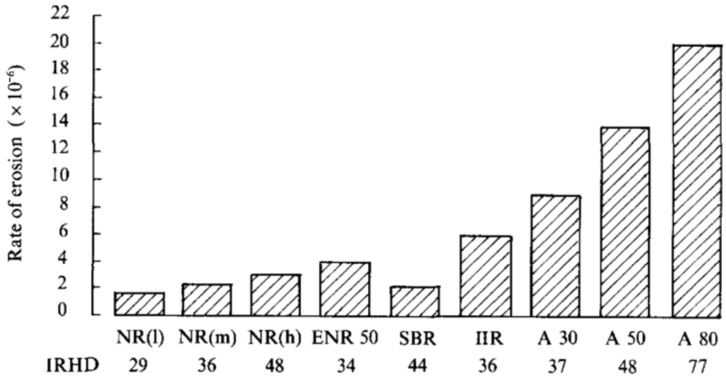

Figure 2.29: Erosion rate as a function of international rubber hardness degree (IRHD). Jet erosion tests were carried out using silica at 30º and a particle velocity of 50 m/s on natural rubber (NR), styrene-butadiene rubber (SBR), butyl rubber (IIR), epoxidized natural rubber (ENR) and polyurethane (A) (Arnold and Hutchings, 1991).

Figure 2.29 shows that, of the three different NRs tested with low (l), medium (m) and high (h) elastic moduli, the rubber with the lowest modulus of elasticity and international rubber hardness degree (IRHD) gave the best erosion resistance. Figure 2.30 shows the relative erosion resistances of various materials. In the Coriolis test, the softer rubber (NR 1, Shore A 40) showed a higher erosion resistance compared with that of the harder NR 2 (Shore A 60) (Jones, 2011). In both tests, softer rubber showed better erosion resistance, a phenomenon that could be related to the higher fatigue resistance of the softer material (Arnold and Hutchings, 1993).

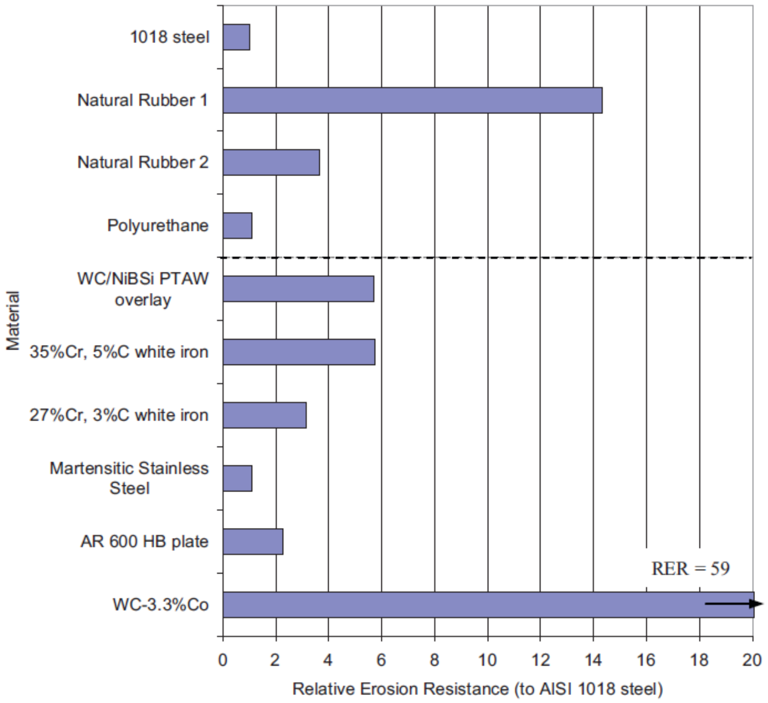

Figure 2.30: Relative erosion resistance (relative to AISI 1018: e.g., RER 59 has an erosion rate 59 times lower than AISI 1018) for various materials for a Coriolis test using silicon carbide abrasive. The average particle velocity in the test device was 19 m/s and the particles used had an angular shape and a size range of 205–365 μm. NR 1 and NR 2 had Shore A hardness values of 40 and 60, respectively (Jones, 2011).

In addition to hardness, other materials properties should also be considered. Arnold and Hutchings (1991) suggested that the erosion resistance of elastomers is dependent on the properties listed in Table 2.6. These data show that rubber with a low modulus of elasticity should have a high modulus of resilience. Therefore, the modulus of elasticity only acts as an indication of resilience, but should not be considered in isolation. The area below a stress–strain curve is used to calculate the modulus of resilience and can be calculated using Equation 2.6, where σ and ε represent the stress and strain, respectively. The strain and stress up to the point of yielding should be used to calculate the modulus of resilience.

$$U_r = \int \sigma \, d\epsilon \tag{2.6}$$

Table 2.6: Target material properties employed to increase the erosion resistance of rubber (Arnold and Hutchings, 1991; Xie et al.*, 2019).*

Property	Requirement
Modulus of elasticity (Young's modulus)	Lower is better
Fatigue resistance	Higher is better
Coefficient of friction	Lower is better
Chemical resistance	Higher is better
Modulus of resilience	Higher is better
Gouging resistance	Higher is better

As observed from the data in Table 2.6, polymers with lower interfacial friction will have lower erosion rates than those with a higher interfacial friction. This was proven using rubber in the presence and absence of lubricant: in each case, the presence of a lubricant or a lower friction coefficient gave a lower erosion rate (Arnold and Hutchings, 1991).

The influence of impingement angle on the wear rate of a material is tribo-system dependent and will differ based on the material and abrasive particles present. Figure 2.31 and Figure 2.32 show that polymers generally experience higher wear rates at lower impingement angles. Figure 2.32 shows that the erosion rate of NR was highest at an impingement angle of 15°. This is lower than the maximum wear rate angle for PU, shown in Figure 2.31.

Chemical attack (e.g., oxidation, microbial) can be accelerated by the presence of a weakened surface layer of a polymer caused by eroding particles that can create preferential sites for chemical attack by a solvent (Stachowiak and Batchelor, 2014), as illustrated in Figure 2.33. NR is not completely inert to hydrolysis and certain solvents can cause devulcanization, where the crosslinked sulfur bonds break down, leading to softening of the material in localized or macroscopic areas, depending on the reaction conditions.

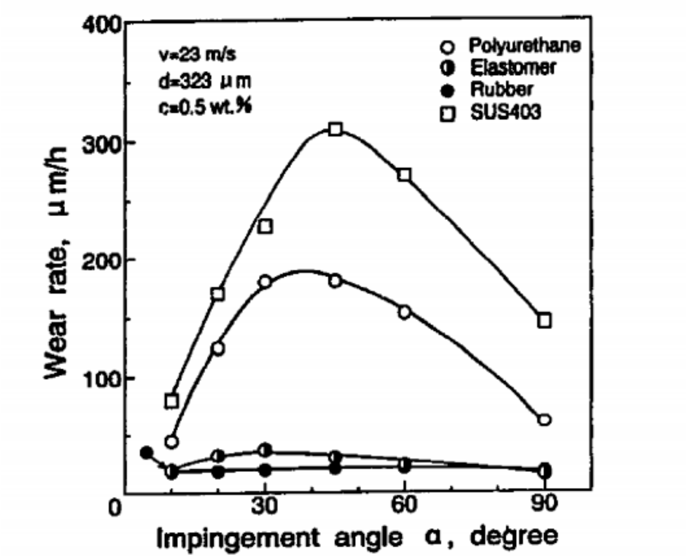

Figure 2.31: Wear rate as a function of impingement angle at a particle velocity of 23 m/s for different materials (Iwai and Nambu, 1997).

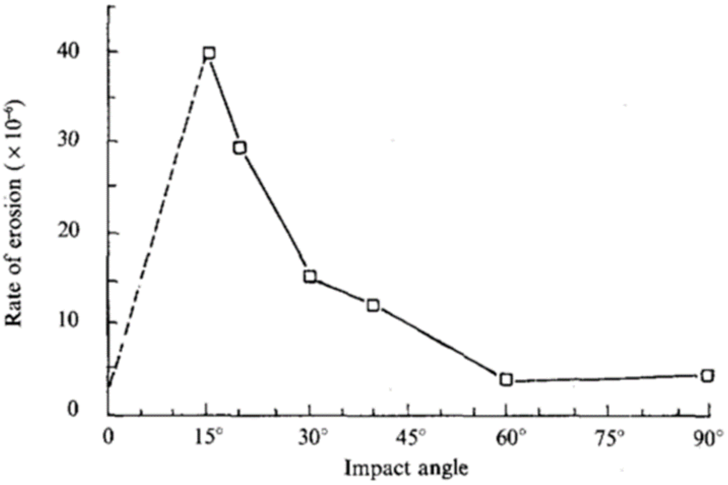

Figure 2.32: Erosion rate as a function of impingement angle is shown for natural rubber with a medium modulus of elasticity. The data refer to a jet erosion test carried out using 120 µm silica particles at a velocity of 100 m/s (Arnold and Hutchings, 1991).

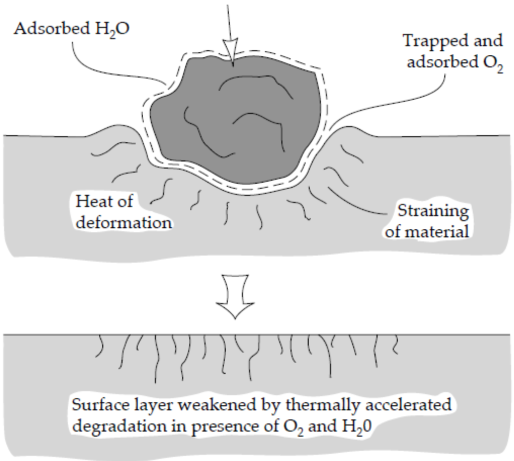

Figure 2.33: Mechanism of accelerated chemical attack due to aggravated cracking and wear on the surface of a polymer (Stachowiak and Batchelor, 2014).

2.7 Effect of Feed and Particle Properties on Wear

Hydrocyclone feed properties include those that can be best described either within a continuum or by using a discrete approach (Ghodrat *et al.*, 2013). Continuum feed properties are the fluid properties, which include concentration (viscosity), flow velocity and chemical properties. These properties are controllable to a certain extent: flow velocity can be controlled by adjusting the pressure and geometry of the hydrocyclone; feed concertation can be controlled by adding water or solids; chemical properties can be controlled in some cases by controlling the pH of the slurry. Discrete feed properties are the particle properties that can be measured discretely for each individual particle. These include particle hardness, SG, size and shape. This section investigates the influence that these properties have on the wear rate of hydrocyclones.

2.7.1 Flow Velocity

There is a power-law relationship between the flowrate and the pressure drop on entering a hydrocyclone. Higher pressure drops lead to higher flowrates and thus higher particle velocities within a fixed control volume (Zhang *et al.*, 2017).

Wear also has a power-law relationship with velocity, as indicated by Equation 2.7, where k is an empirical constant, v is velocity and n is the velocity exponent (typically taking a value of 2–3) (Stachowiak and Batchelor, 2014). The empirical constant k is a function of the wear mechanism and the particle and feed properties (Zhang *et al.*, 1995). The power-law relationship in Equation 2.7 also relates to the kinetic energy of a particle and shows that wear is related to the dissipation of energy from a particle to its surroundings, as described by the first law of thermodynamics.

$$\frac{dm}{dt} = kv^n \tag{2.7}$$

Velocity is also related to the amount of turbulence within a flow regime: hydrocyclone feed velocities will typically have a high Reynolds number (Re > 10^4) and be within the turbulent flow regime (White, 2009). Turbulent flow leads to more particle impacts with the substrate wall and thereby accelerates the wear rate, as illustrated in Figure 2.34. Therefore, it is typically desirable to minimize the amount of turbulence by using more streamlined hydrocyclone designs.

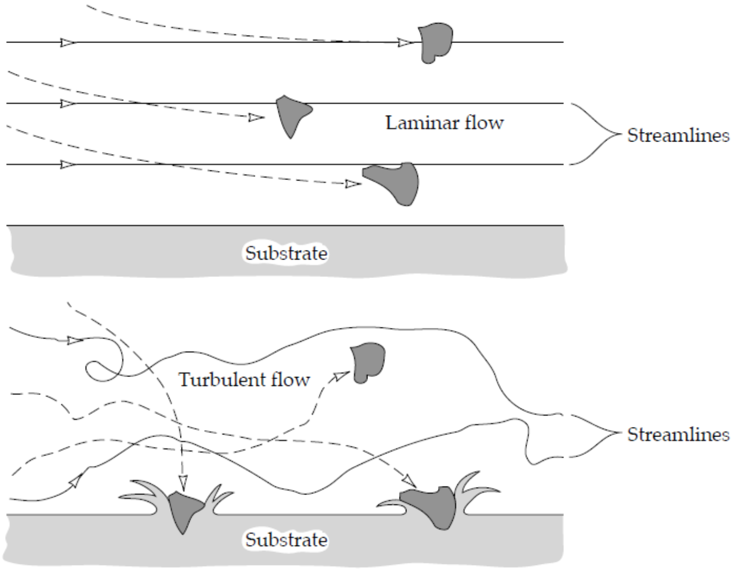

Figure 2.34: Illustration of particle paths within laminar and turbulent flow regimes (Stachowiak and Batchelor, 2014).

2.7.2 Slurry concentration

The influence of slurry concentration on wear rate has been investigated by various authors (Zhang *et al.*, 1995; Jafari *et al.*, 2018; Frosell *et al.*, 2015). The results varied based on the test used and the wear mechanism present.

Figure 2.35 shows the relationship between slurry concentration and wear rate for polytetrafluoroethylene (PTFE), nylon, styrene-butadiene rubber (SBR) and PU based on a modified SJE test (shown in Figure 2.21) that was designed to simulate the conditions of centrifugal slurry erosion.

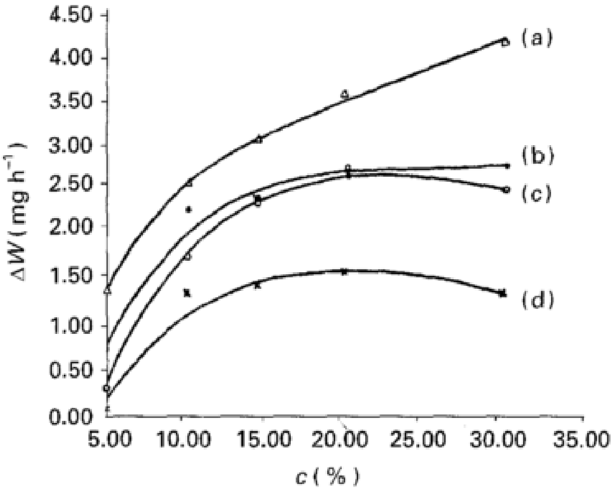

Figure 2.35. Influence of slurry concentration on wear rate for (a) polytetrafluoroethylene, (b) nylon, (c) styrene-butadiene rubber and (d) polyurethane using a modified slurry jet erosion test that simulated the flow experienced in an hydrocyclone at a particle velocity of 11.08 m/s using quartz particles sized between 200–300 µm (Zhang et al.*, 1995). Note that this device was not built according to a standard.*

The modified SJE test data shown in Figure 2.35 show that the wear rate increased with slurry concentration up to about 15% solids by mass for nylon, SBR and PU; above this concentration, the wear rate changed, depending on the substrate material. In most cases, the derivative (slope) of the wear rate started to decrease at this point. The reason for this is related to interparticle interaction that can influence the particle velocity and impingement angle (Zhang *et al.*, 1995).

The results from a slurry pot test performed according to ASTM G119 are displayed in Figure 2.36. The results showed an increase in erosion rate for steel at higher slurry concentrations (Jafari *et al.*, 2018). The mass loss increase was not linear and showed a decreased rate of change as the slurry concentration exceeded 50% solids by mass. Therefore, for certain materials, there appears to be a critical point at which an increase in the slurry concentration will no longer lead to an increase in the wear rate and the wear rate could decrease beyond this point in some cases (such as for PU, shown in Figure 2.35). The value of this critical point in slurry concentration in hydrocyclone wear needs to be verified with in-situ tests using specific materials of construction used in practice.

Based on these tests, it can be stated that the influence of slurry concentration on the wear rate will be dependent on the substrate material type, and there is no simple relationship that applies to all material types and wear mechanisms.

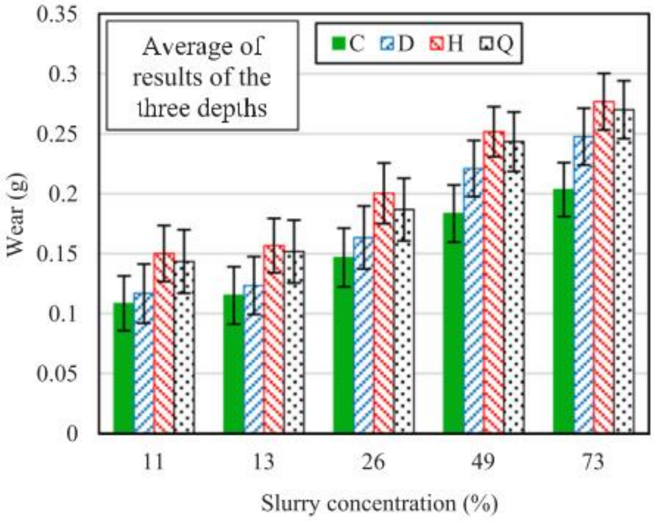

Figure 2.36. Comparison of amount of wear as a function of slurry concentration, with data taken from a slurry pot ASTM G119 test. The test was conducted on four different steels, labelled C, D, H and Q (Jafari et al., *2018).*

2.7.3 Chemical Properties

The water quality varies between different minerals processing plants because water (or solution) recycled back to the plant has usually been exposed to different minerals and potential chemical reactions (Cortie *et al.*, 1996). Chemical properties of the slurry will influence whether some materials (substrates) will undergo chemical attack and the extent to which this will occur. An example would be the higher oxidation rate of steel in an acidic environment and its subsequent increased wear rate.

Common mineral reactions in a slurry environment are hydrolysis and redox reactions. The oxidation of certain iron sulfide minerals in the presence of water leads to sulfate formation and will increase the hydronium ion concentration, which will lower the pH of the slurry. These sulfide minerals include pyrite (FeS_2), marcasite (FeS_2), chalcopyrite ($CuFeS_2$) and arsenopyrite (FeAsS) (Jacobs and Testa, 2014). Their oxidation reactions are facilitated by acidophilic aerobic microbes that catalyse the oxidation of ferrous (Fe^{2+}) to ferric (Fe^{3+}) iron. Microbes can also cause direct chemical attack or degradation of materials. A common sulfide mineral that is very prone to acid formation is pyrite. Its basic preliminary oxidation reaction is given by Equation 2.8. The decrease in pH of a coal ore that was recycled in a wear test is shown in Figure 2.37, where the pH dropped to a value of 4 after 500 cycles. These data show that, with time, the pH of a solution can decrease as acid formation progresses, allowing more sulfide minerals to dissolve into solution. This can occur due to plant water recirculation and can be controlled by dosing the slurry with a base to increase the pH.

$$2FeS_2(s) + 7O_2(g) + 2H_2O(l) \rightarrow 2Fe^{2+}(aq) + 4SO_4^{2-}(aq) + 4H^+(aq) \qquad (2.8)$$

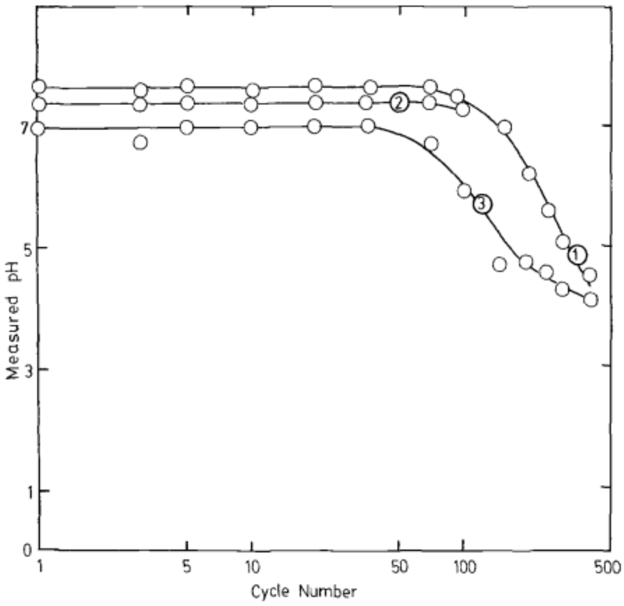

Figure 2.37: Effect of recycling process water through a closed-loop coal ore system on lowering the pH due to reaction of soluble disulfide minerals present (Miller and Schmidt, 1987).

2.7.4 Particle Hardness and Specific Gravity

For certain materials, the abrasive wear resistance increases if the substrate-to-erodent hardness ratio increases (Stachowiak and Batchelor, 2014). The hardness of elastomers is much lower than that of typical mineral particles, but can outperform that of harder non-elastomers (Budinski, 2007c). Therefore, the ratio of particle hardness to the hardness of the substrate does not provide a guideline for the abrasive wear of all material types.

In Figure 2.38, the erosion rate is compared for two ductile steels using a slurry pot test (AA6063 with a Vickers hardness of 91 HV and AISI 304L of 210 HV) at different orientation angles and using three different erodents with the properties listed in Table 2.7 (Desale *et al.*, 2006).

Figure 2.38 shows that alumina produced a significantly higher wear rate for both steels than silicon carbide at low impingement angles, although silicon carbide has a higher Vickers hardness (Table 2.7). This demonstrated that the particle SG or shape has a greater effect on the wear rate than hardness. The particle SG will also influence the amount of energy possessed by the particle. It is known that, for the same velocity and size, a particle with higher SG will have more kinetic energy (Desale *et al.*, 2006); however, a higher SG particle will require a higher minimum transport velocity to remain in suspension (Thakur, 2017), thereby creating the possibility that lower SG particles can have a higher velocity and kinetic energy. The effect of SG on wear will, therefore, also be dependent on particle velocity for the specific application.

Table 2.7: Erodent properties of quartz, alumina and silicon carbide used for the slurry pot test data shown in Figure 2.38.

Erodent	Hardness (HV)	Shape factor	SG	Particle size (µm)
Quartz	1100	0.7	2.65	500–600
Alumina	1800	0.37 (most angular)	3.94	500–600
Silicon carbide	2500	0.44	3.22	500–600

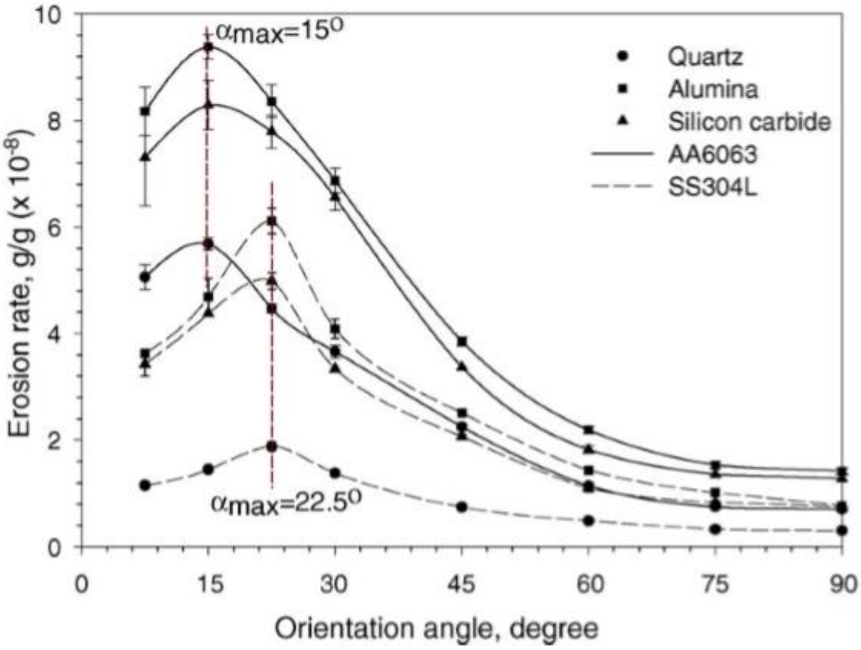

Figure 2.38: Comparison of erosion rate for two steels using a slurry pot test The slurry pot test (ASTM G119) used an average particle size of 550 µm, solids concentration of 10 % solids by mass and particle velocity of 3 m/s (Desale et al.*, 2006).*

2.7.5 Particle Shape and Friability

Particles that are more angular (less circular) will cause more wear, as shown in Figure 2.39 (Walker and Hambe, 2014). It is also evident that particle shape has a more severe effect at lower impingement angles, as shown in Figure 2.38 (Desale *et al.*, 2006). More angular particles have a smaller effective contact radius on the substrate compared with spherical particles, and therefore a smaller contact area, as illustrated in Figure 2.40. A more angular particle with a smaller contact area leads to a higher localized applied stress compared with that of a rounder particle (Desale *et al.*, 2006). Sharp particles can thus penetrate deeper into the substrate and cause more plastic deformation and wear (Xie *et al.*, 2019). The basic mechanism of smoothening of a friable particle is illustrated in Figure 2.41.

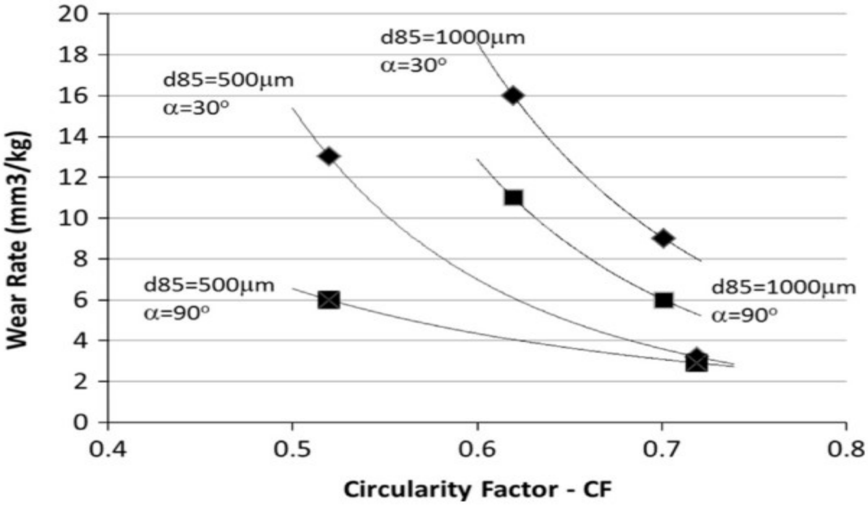

Figure 2.39: Influence of circularity of particles on wear rate of 27% Cr white iron eroded in a slurry jet erosion test using 500 µm alumina and 1000 µm quartz sand (Walker and Hambe, 2014).

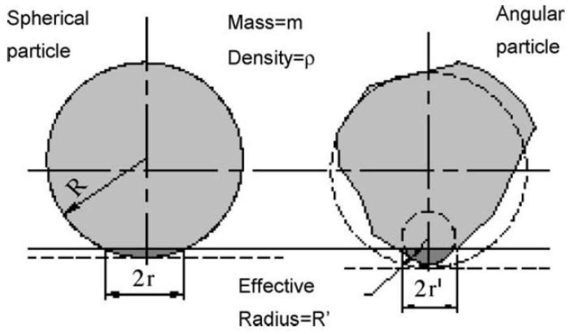

Figure 2.40: Effective radii of spherical and angular particles (Desale et al.*, 2006)*

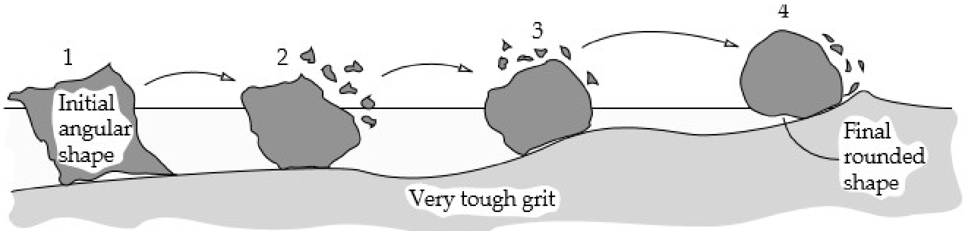

Figure 2.41: Illustration of how particles become smoother with time due to attrition (Stachowiak and Batchelor, 2014).

Friability is the gradual breakdown of particles due to externally applied forces. The shape of the particles will also become smoother and will lead to less wear. The smoothening effect is most severe when the material is recycled in a closed loop, as observed in the data of Figure 2.42, where particle roundness increased with the number of cycles. For practical reasons, laboratory-scale slurry wear tests usually require material to be recycled, especially when the wear rate is very slow; therefore, laboratory-scale tests that recirculate material cannot fully simulate field conditions, in which mostly new material enters the system.

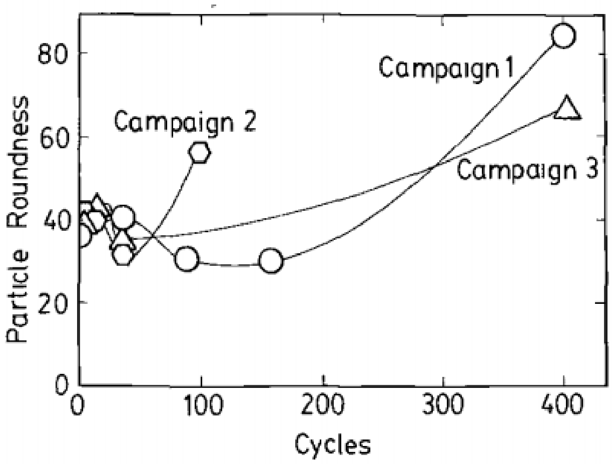

Figure 2.42: Particle roundness as a function of number of cycles through which the material is recycled. The roundness is the percentage of material with a shape factor larger than 0.03, with a perfect sphere having a roundness of 100 (Miller and Schmidt, 1987).

2.7.6 Particle Size

Using an SJE test, it was proven that a critical velocity of the impinging particles is required to cause wear. The critical velocity is a function of particle size, as shown in Figure 2.43 (Iwai and Nambu, 1997), with smaller particles requiring a much greater velocity to cause wear on a specific substrate. If the velocity is kept constant, there will be a critical diameter at which wear will start to occur for a specific particle velocity and material, as shown in Figure 2.44. The phenomenon of a critical velocity has also been observed in slurry pipeline and transport applications (Jacobs, 1991).

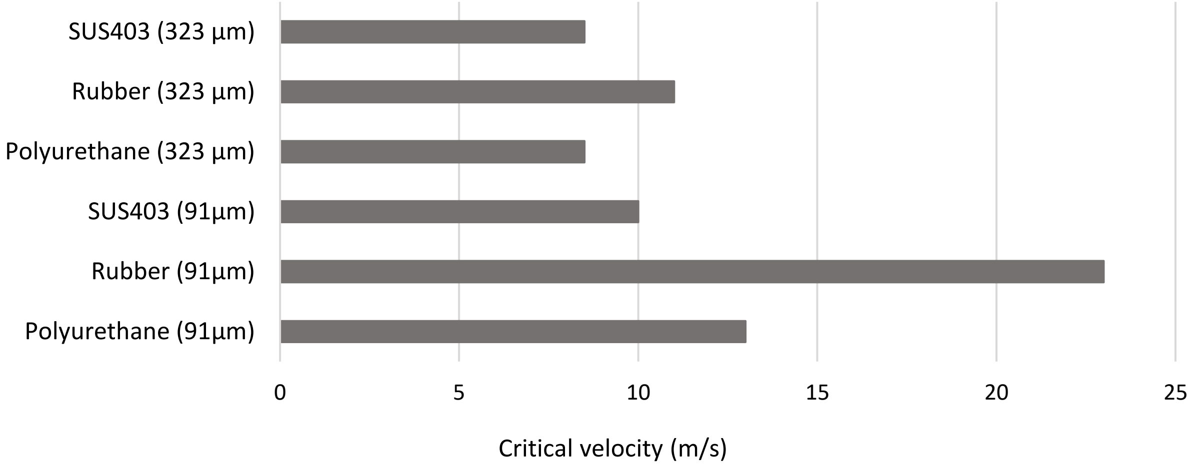

Figure 2.43: Critical velocity for different particle sizes and materials (SUS403 is a martensitic stainless steel) for a slurry jet erosion test carried out using 0.5 % solids by mass, silica erodent at an impingement angle of 30º (derived from Iwai and Nambu, 1997).

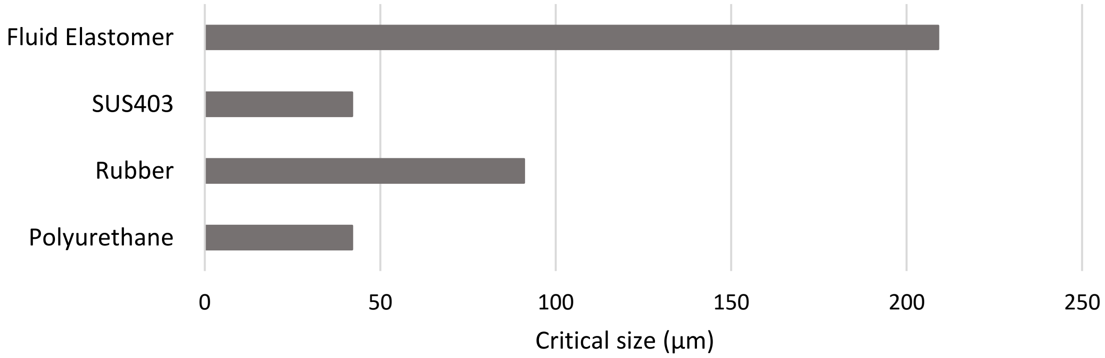

Figure 2.44: Critical diameter for different particle sizes and materials (SUS403 is a martensitic stainless steel) for a slurry jet erosion test carried out using 0.5 % solids by mass, silica erodent at an impingement angle of 30º and a particle velocity of 23 m/s (derived from Iwai and Nambu, 1997).

Figure 2.45 shows the relationship between particle size and wear rate for PTFE, nylon, SBR and PU based on a modified SJE test using semi-round quartz particles. The test was designed to simulate the conditions of centrifugal slurry erosion (refer to Section 2.5.7). The data show that the wear rate and its derivative ($\Delta W'$) are material (substrate)-dependent. The erosion wear rate increased with particle size, but the second derivative of the wear rate curve, displayed in Figure 2.45, was negative for all materials tested. It is evident that the influence of particle size on the wear rate is not the same for all materials because different wear mechanisms are present. The influence of particle size has also been shown to differ based on the impingement angle (Stachowiak and Batchelor, 2014).

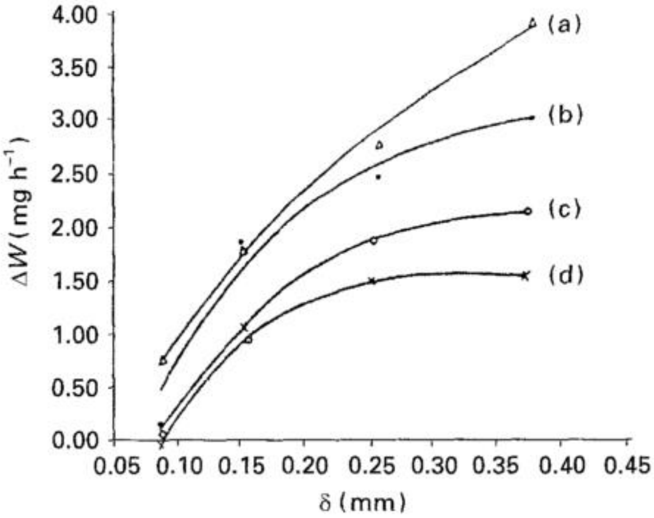

Figure 2.45: Erosion test wear rate as a function of changes in quartz particle size for (a) polytetrafluoroethylene, (b) nylon, (c) styrene-butadiene rubber and (d) polyurethane at a concentration of 10 % solids by mass and a particle velocity of 11 m/s. (Zhang et al.*, 1995).*

The decrease in the derivative of the erosion rate above a critical particle size (e.g., 250 µm) that is shown in Figure 2.45 will not always be the case, and does not apply for larger angular particles. It has been observed that large angular quartz particles (2–4 mm) will cause a much higher (order of magnitude larger) wear rate on certain polymers than smaller 212–300 µm quartz particles, as determined by a Coriolis test (Xie *et al.*, 2019). This relates to the findings that polymers can be prone to gouging at larger particle sizes (Jacobs, 1991).

2.8 Wear Quantification and Imaging Techniques

Selected methods used for measuring wear and material surface profiles are discussed in this section.

2.8.1 Optical Profilometer

Profilometers are devices used to determine the surface profile of a material at micron or nanometre scale. An optical profilometer does not make physical contact with the measured sample surface. A non-contact device has the advantage of not causing any possible damage to the sample surface and requires less time to create a surface profile (Lindroos *et al.*, 2010). There are various types of optical profilometers available: this study made use of a chromatic confocal profilometer.

A chromatic confocal profilometer uses a chromatic confocal white light source and spectrometer to create a height profile of a surface. Different wavelengths of light hit the surface and are reflected, but only one specific wavelength will focus on the exact surface height. This wavelength can be measured using a charge-coupled device spectrometer, thereby giving the surface height at a specific coordinate (Ramirez, 2012). Figure 2.46 shows a schematic of a chromatic confocal profilometer and the measurement technique.

The sensor moves over a specified area of the sample at a set resolution to create a three-dimensional (3D) surface profile. The area analysed is smaller than the sample itself and therefore needs to be representative of the overall sample. The scanned area is statistically analysed to determine various parameters. The most common parameters to measure are the arithmetic mean surface roughness (Sa) and the root mean square of the surface roughness (Sq). The Sa value is the average of the differences between each peak and the mean plane height, as illustrated in Figure 2.46(b) (Reyence, 2017). The meanings and methods for calculating various parameters are shown in Appendix B.

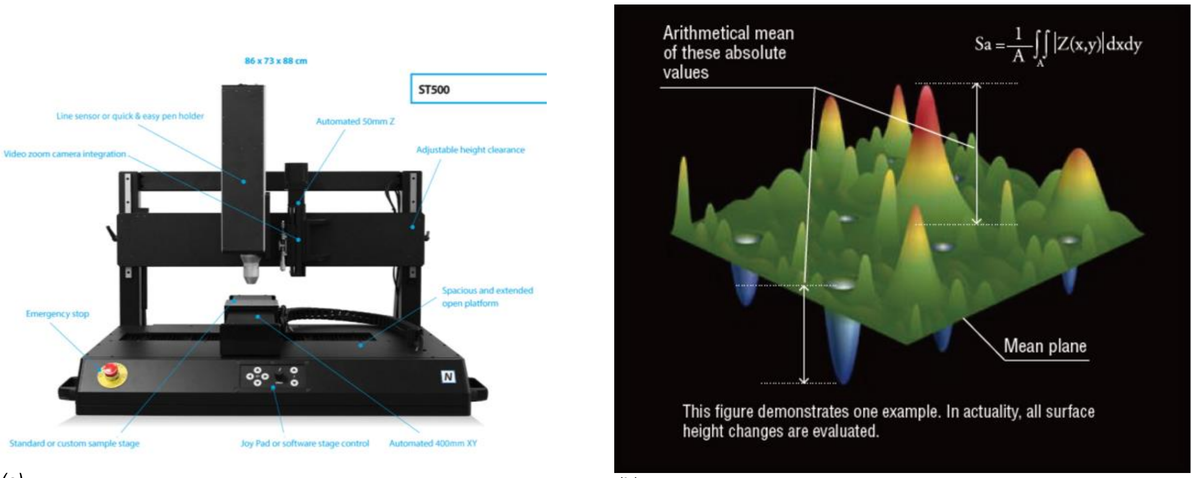

(a) *(b)*

Figure 2.46: (a) Nanovea ST500 optical chromatic confocal profilometer (Ramirez, 2012). (b) Determination of arithmetic mean roughness Sa (Reyence, 2017).

2.8.2 Microcomputed Tomography

Microcomputed tomography (micro-CT) scanners use an X-ray tube with a cathode and a metal or multi-metal target that is attached to the anode to create and emit X-rays from a point source at a desired wavelength. The X-rays are absorbed, scattered or pass through the matter of the sample, depending on its X-ray attenuation coefficient. The X-ray intensity that passes through the sample is measured using a detector. A sample manipulator is used to rotate and translate the sample to create multiple projections that are used for tomographic reconstruction (Hoffman and Beer, 2012). The scan resolution that can be obtained in a specific scan is dependent on the specifications of the detector, the size of the point source and the magnification, which is also dependent on the geometry of the sample (Buschow *et al.*, 2001). Certain materials (higher-density matter) require higher-energy X-rays to pass through the matter and could therefore require a higher power X-ray source (e.g., a 320 kV rather than 225 kV X-ray source). The principal components of a micro-CT scanner are illustrated in Figure 2.47.

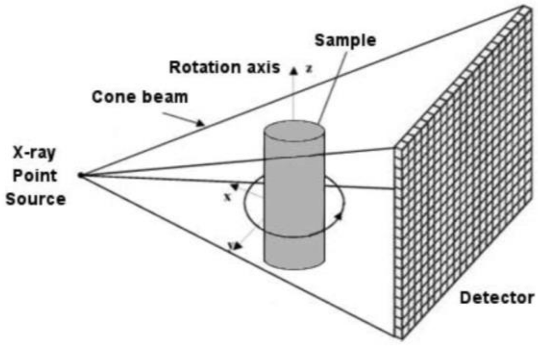

Figure 2.47: Principal components of a microcomputed-tomography scanner (Lin et al., 2009).

Micro-CT has been used to quantify wear of materials (MacDonald *et al.*, 2009), but has not yet been reported to have been used to study erosive wear in a hydrocyclone in a slurry environment.

2.9 Literature Summary

The influence of wear on various hydrocyclone applications differs because some applications are more sensitive to wear than others.

The geometry of a hydrocyclone will influence its concentration distribution: the highest solids concentration and larger particles will be found at the bottom of a hydrocyclone. The number of collisions with the sidewall of the hydrocyclone (substrate) will increase at the bottom of the lower cone, as has been illustrated by positron emission particle tracking methods. Velocity distributions within a hydrocyclone show that the tangential and axial velocities will be higher at the vortex finder compared with other regions.

Hydrocyclone efficiency is evaluated using a partition curve. The partition curve gives information on the actual and corrected cut points. Corrected data can be obtained by using a suitable model.

The two basic types of wear mechanisms are abrasive and erosive. Hydrocyclones experience erosive wear, which is a function of the feed properties, particle properties, hydrocyclone material and its geometry.

There are various standardized laboratory test methods available to test the wear resistance of materials. Based on ASTM selection guidelines, the SJE, Coriolis and slurry pot tests are considered the best options of those evaluated.

Hydrocyclones can be manufactured from various engineering materials, such as polymers, metals and ceramics. Polymers and metals were investigated. It was determined that hardness is not the determining factor of wear resistance of a metal and its microstructure should be considered to optimize the wear life for a specific application. For the case of polymers, it was found that the elastomeric properties play an important role in erosive wear resistance, due to the deflection of energy by deformed elastic materials. Evidence suggests that use of rubber requires a low Young’s modulus, high modulus of resilience, low hardness, high toughness and high tear strength to give an optimal wear life. It was generally observed that material selection and wear life predictions should be primarily based on application-specific test work using a suitable test method.

Feed and particle properties have a significant effect on the wear rate. Feed (slurry) properties are described as a continuum that is measured as a whole, which include flow velocity, slurry concentration and chemical properties. Particle properties are described as discrete properties that are unique to each particle and include particle hardness, SG, particle size and particle shape (friability). In the case of flow velocity, it was illustrated that the wear rate has a power-law relationship with the slurry velocity. The influence of slurry concentration showed different results based on the substrate. Furthermore, results using a modified SJE test and a slurry pot showed slightly different results. The modified SJE test showed that, for most polymers, there is a critical concentration above which the wear rate will decrease, perhaps due to interparticle interaction; the slurry pot test did not show a critical concentration point for the steel samples tested. Chemical properties of a slurry can commonly be influenced by the presence of iron sulfide minerals that oxidize (sometimes in the presence of aerobic microbes) to form sulfuric acid. The resulting lower pH then accelerates the wear of certain materials. A slurry pot test found that particle hardness has a less severe effect on wear rate (for ductile steels) compared with the SG and shape of the erodent particle. More angular particles lead to higher contact stresses with the substrate and therefore higher wear rates. The effect on the shape factor (smoothening) during recirculation of material in a continuous loop during a laboratory test was shown. A critical particle size is required, at a set velocity, to produce wear. Large angular particles typically cause gouging of polymers.

Modern methods for quantifying wear and measuring surface profiles of materials were briefly discussed.

CHAPTER 3: METHODOLOGY

3.1 Overview

The objectives of this project, as outlined in Section 1.2, were addressed in various phases of the experimental plan, illustrated in Figure 3.1. This chapter discusses each of these phases in further detail.

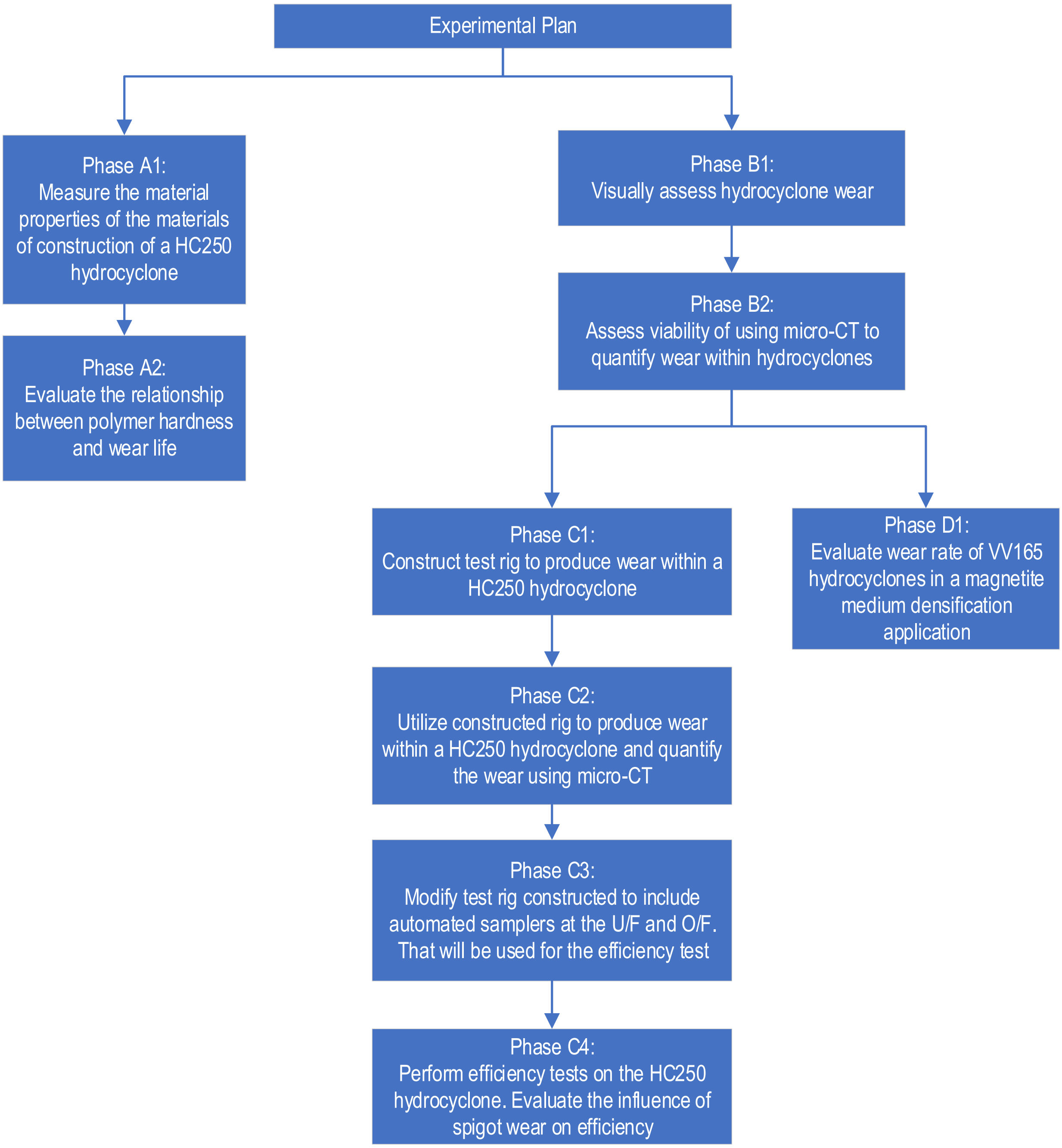

Figure 3.1: Summary of basic experimental plan used to address the objectives of this project.

3.2 Phase A: Material Properties

In Phase A1, the properties of the materials used in a Multotec HC250-15-1/A-B/50 (Dc 250 mm) hydrocyclone were measured. In Phase A2, the relationship between wear life and the Shore A hardness of selected NR compounds was tested.

3.2.1 Phase A1

During Phase A1, the material properties of an HC250 hydrocyclone (excluding the metal shell) were measured and compared. An overview of the activities of Phase A1 is illustrated in Figure 3.2.

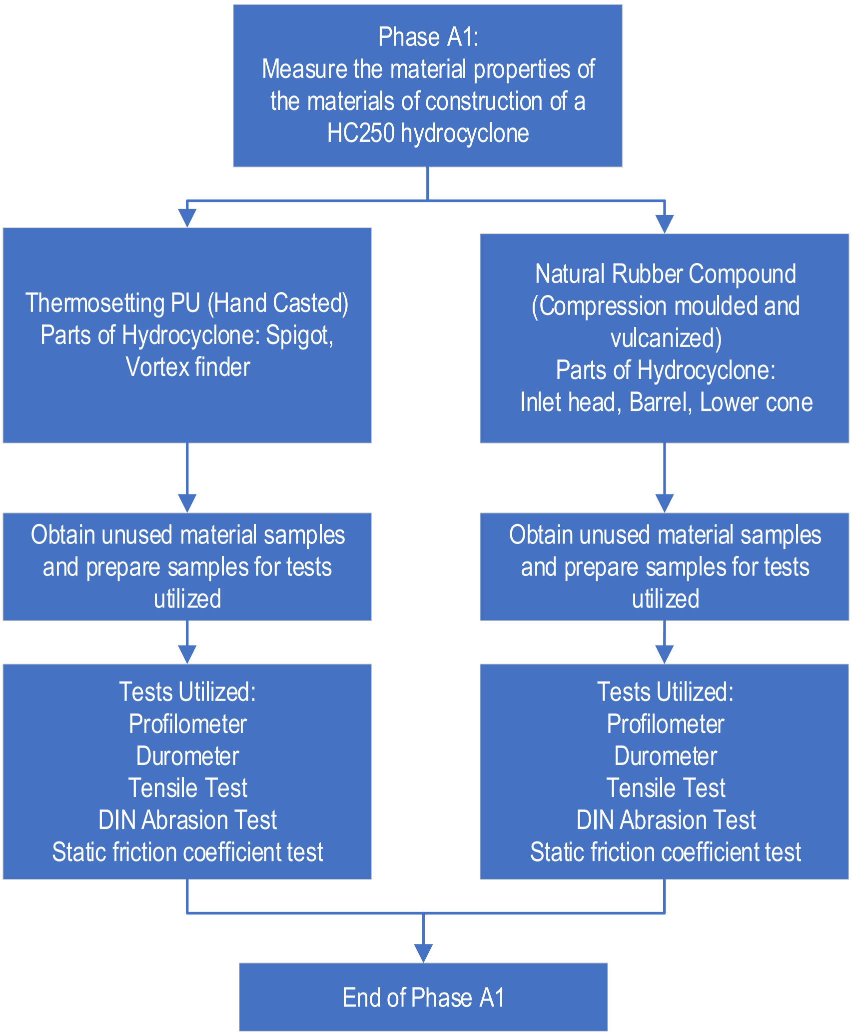

Figure 3.2: Summary of steps followed in Phase A1.

The Multotec HC250 hydrocyclone is made of a cast metal shell lined with a compression-moulded vulcanized natural rubber compound (NR; refer to Table E.4 in Appendix E for information on the composition) at the inlet head, barrel and cone. The spigot and vortex finder are made of hand-cast thermosetting polyurethane (PU) (BASF, Elasturan 6055/114; refer to Table E.2. in Appendix E for the composition). The various parts of the HC250 hydrocyclone are displayed in Figure 3.3.

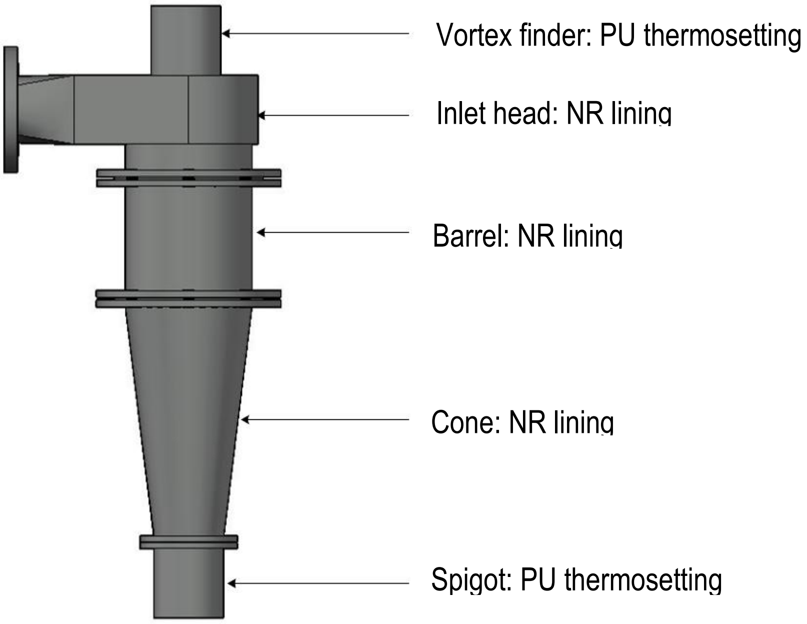

Figure 3.3: Different parts and materials of HC250-15-1/A-B/50 hydrocyclone. The exterior comprises a metal shell.

The various material tests carried out on the virgin NR and PU samples are listed in Table 3.1, along with the properties tested and laboratories employed.

Table 3.1: Material property tests.

Test	Property tested	Vendor
Tensile test	Tensile strength, ultimate elongation	Multotec
Durometer hardness test	Shore hardness	Multotec
DIN abrasion test	Wear volume	Multotec
Friction test	Static friction coefficient	University of Pretoria
Optical profilometer	Surface properties	University of Pretoria

The tensile test was performed using 30 mm × 4 mm tensile test samples on a fully automatic M350-10 CT tensile tester (Testometric Co., UK) that adheres to ASTM D412, DIN (Deutsches Institut für Normung), and EN (European) standards. The durometer hardness test was performed using a Shore A hardness tester according to ASTM D2240. The DIN abrasion test was the same as illustrated in Figure 2.20 and described by the ASTM D5963 standard.

An ST500 chromatic confocal profilometer (Nanovea, USA) was used to analyse the surface of unused thermosetting PU and NR to determine the difference in surface roughness (Sa) between the NR and PU used within the HC250 hydrocyclone.

3.2.2 Phase A2

During Phase A2, the relationship between polymer properties and wear life was briefly evaluated. The relationship between NR hardness and wear life was measured. An overview of Phase A2 activities is illustrated in Figure 3.4.

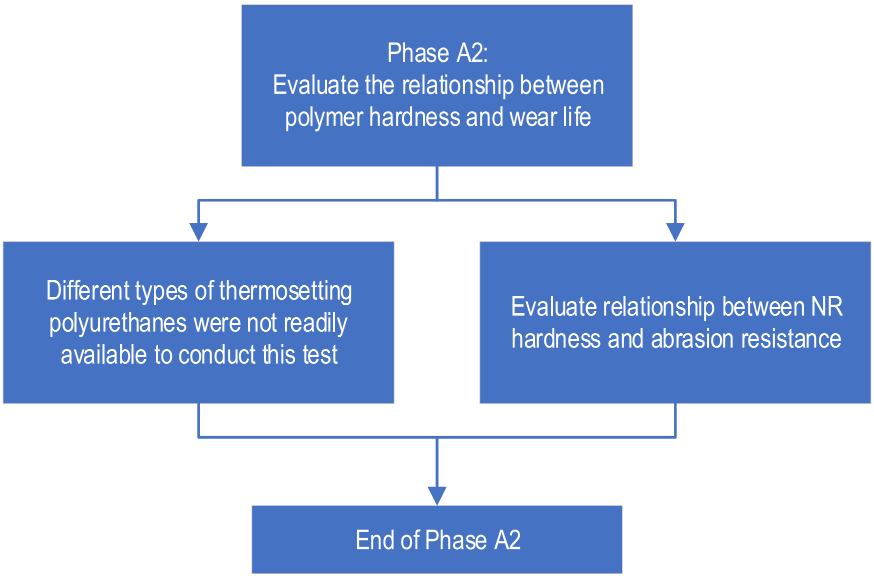

Figure 3.4: Summary of steps followed in Phase A2.

The abrasion resistance of three NR samples with different Shore A hardness values were measured using a DIN abrasion test, according to ASTM D5963. The ASTM D5963 test was used because it was readily available; more suitable test methods, as suggested in Section 2.5.8, were not available.

3.3 Phase B: Quantifying Wear

Initial hydrocyclone wear observations were made using a non-quantitative technique, i.e., use of photographs. Thereafter, it was investigated whether hydrocyclone wear could be quantified using micro-CT scans.

3.3.1 Phase B1

Hydrocyclone wear in selected minerals processing applications was visually assessed and photographed. An overview of the activities of Phase B1 is illustrated in Figure 3.5.

The wear patterns observed and photographed were from coal (VV350 PU hydrocyclone) and ferrochrome slag (D_c = 250 mm, PU hydrocyclone spigot) applications (the exact sites are proprietary and cannot be disclosed). The material feed sizes of the coal and ferrochrome slag applications were −0.5 mm and −3 mm, respectively. All hydrocyclones were used as classification hydrocyclones.

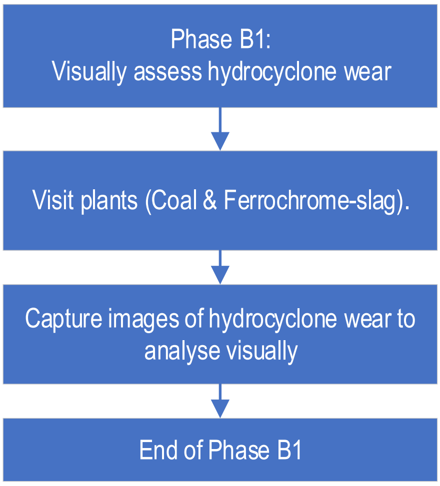

Figure 3.5: Summary of steps followed in Phase B1.

3.3.2 Phase B2

Phase B2 assessed whether it was feasible to quantify hydrocyclone wear using micro-CT scans. An overview of the activities of Phase B2 is illustrated in Figure 3.6.

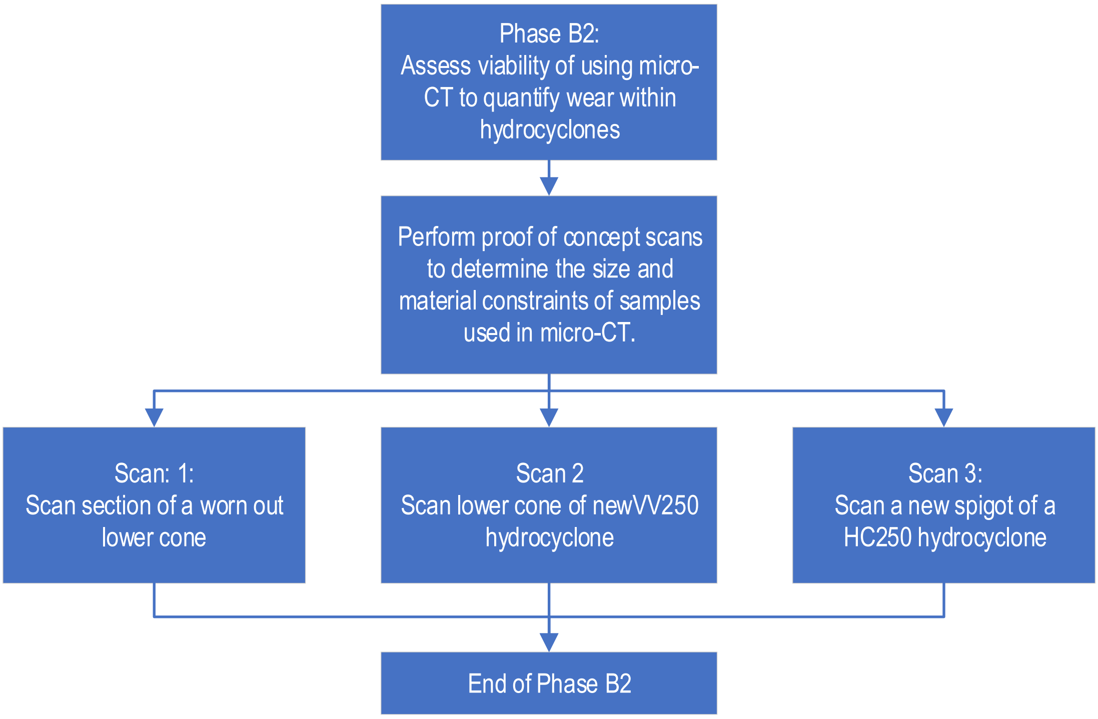

Figure 3.6: Summary of steps followed in phase B2.

The micro-CT scanner used was a Nikon XT H 225 ST (Japan), which was available at the MIXRAD facility at Nuclear Energy Corporation of South Africa (NECSA) (displayed in Figure 3.7. The 225 kV X-ray source (3 µm spot size) and translation table of the scanner are shown in Figure 3.7(b).

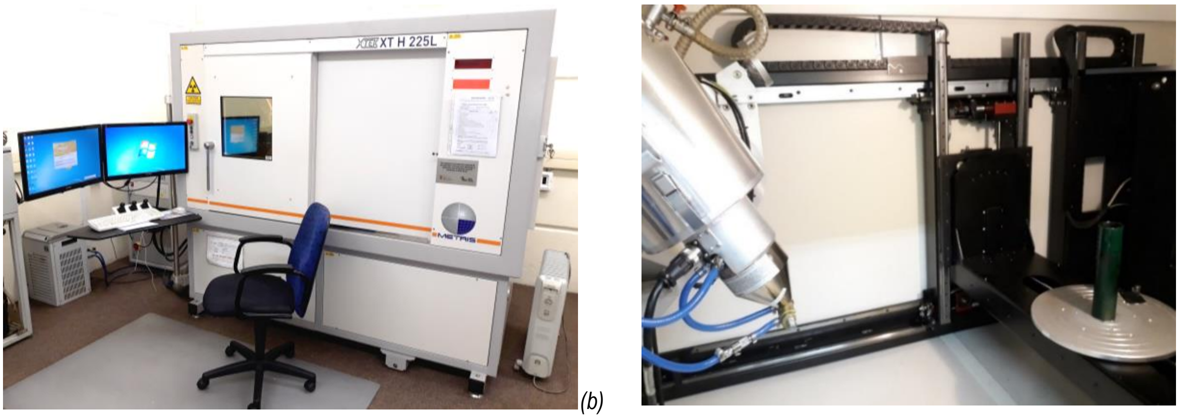

(a) (b)

Figure 3.7: (a) Exterior lead-lined cabinet of microcomputed tomography scanner (Nikon XT H 225 ST at MIXRAD, NECSA). (b) 225 kV X-ray source on the left and translation table on the right.

The scanner has a detector size of 400 mm × 400 mm and could handle a sample of this size, but at the severe cost of spatial resolution. Initials scans were carried out using a spatial resolution of 0.069 mm. Three proof-of-concepts scans were performed on a worn lower cone (origin and application unknown), a new lower cone (of a VV250) and a new (Dc = 35 mm HC250) spigot.

The height of the lower cones exceeded 400 mm, therefore only a section could be scanned. The spigot had an outside diameter of 120 mm and height of ±200 mm so the entire spigot could be scanned. Therefore, only the spigot could be fully analysed, so this was used for the remainder of the tests. The spigot area is known to experience the most wear and was, therefore, arguably the most important area to investigate.

3.4 Phase C: Wear and Efficiency Analysis of HC250 Hydrocyclone

3.4.1 Phase C1

An overview of the activities of Phase C1 is illustrated in Figure 3.8. A rig was developed to recirculate feed material and produce wear in a HC250 hydrocyclone, as displayed in Figure 3.10. Side and front views of the rig are displayed in Figure 3.10(a) and (b), respectively.

The rig displayed in Figure 3.10 recirculated material through the hydrocyclone using a common feed and discharge tank. The tank could handle up to 1200 L of slurry, but a lot of spillage would occur if the tank was filled to capacity. The bypass valve was used to sample the recirculating feed material. The rig had a gate valve and flush line to flush the pump, if necessary, and avoid any blockages. A pressure gauge (SANS 1123/1000) was used to measure the feed pressure into the hydrocyclone. A polymer pump impeller, frame plate and cover plate were used to extend the wear life of the pump. Pipes were rubber-lined to extend their wear life. The motor had a power rating of 37 kW and was controlled by a variable speed drive (WEG Industries, Brazil). The pump was a 4/3 centrifugal slurry pump with a gland seal.

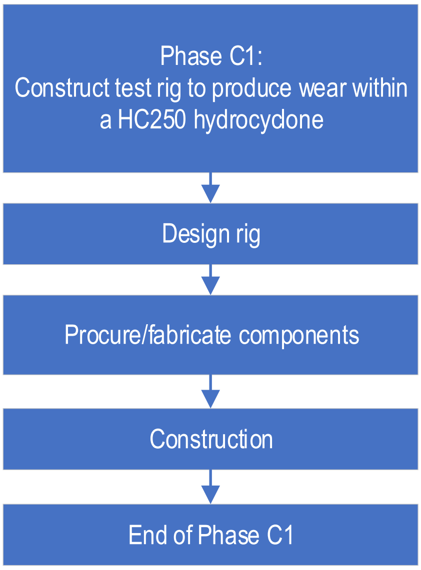

Figure 3.8: Summary of steps followed in Phase C1.

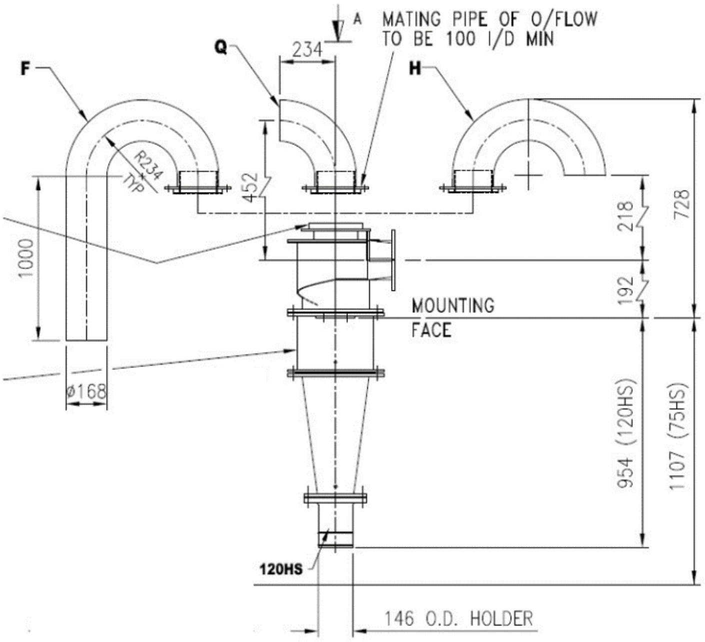

Figure 3.9: Geometry and dimensions of HC250-15-1/A-B/50 hydrocyclone (Multotec 2018).

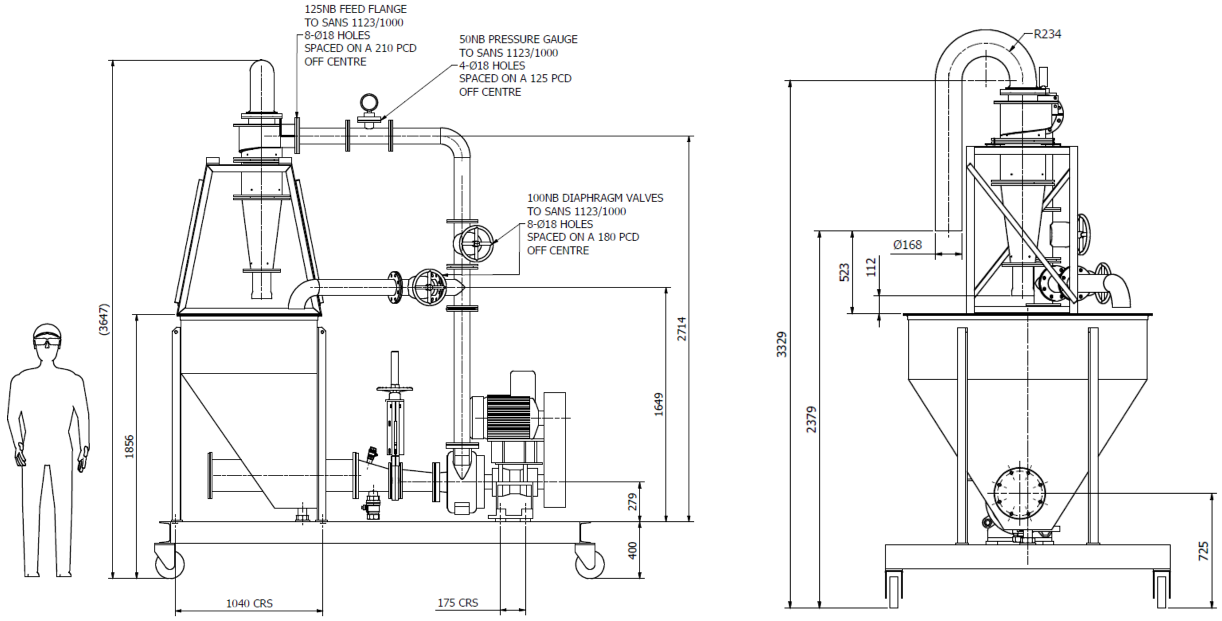

(a) *(b)*

Figure 3.10: Original design of wear test rig showing (a) side and (b) front views (Multotec 2018).

3.4.2 Phase C2

A recirculating wear test was carried out using the constructed rig to produce and quantify wear, using micro-CT scans, in a new HC250 hydrocyclone. An overview of the activities of Phase C2 is illustrated in Figure 3.11.

As illustrated in Figure 3.11, a new 50 mm spigot used in a HC250 hydrocyclone was scanned to determine its original volume. Thereafter, abrasive feed material was recirculated through the hydrocyclone to produce wear and the spigot was scanned again to determine the change in volume. This process was repeated multiple times. Visual inspections were carried out during this phase to look for signs of wear in the other parts of the hydrocyclone. The change in volume of the spigot was analysed using the change in void volume within a fixed volume (height and radius). The analysis was carried out using VGSTUDIO MAX software (Bruker, USA). A snapshot of the analysis of the 50 mm PU spigot is shown in Figure 3.12.

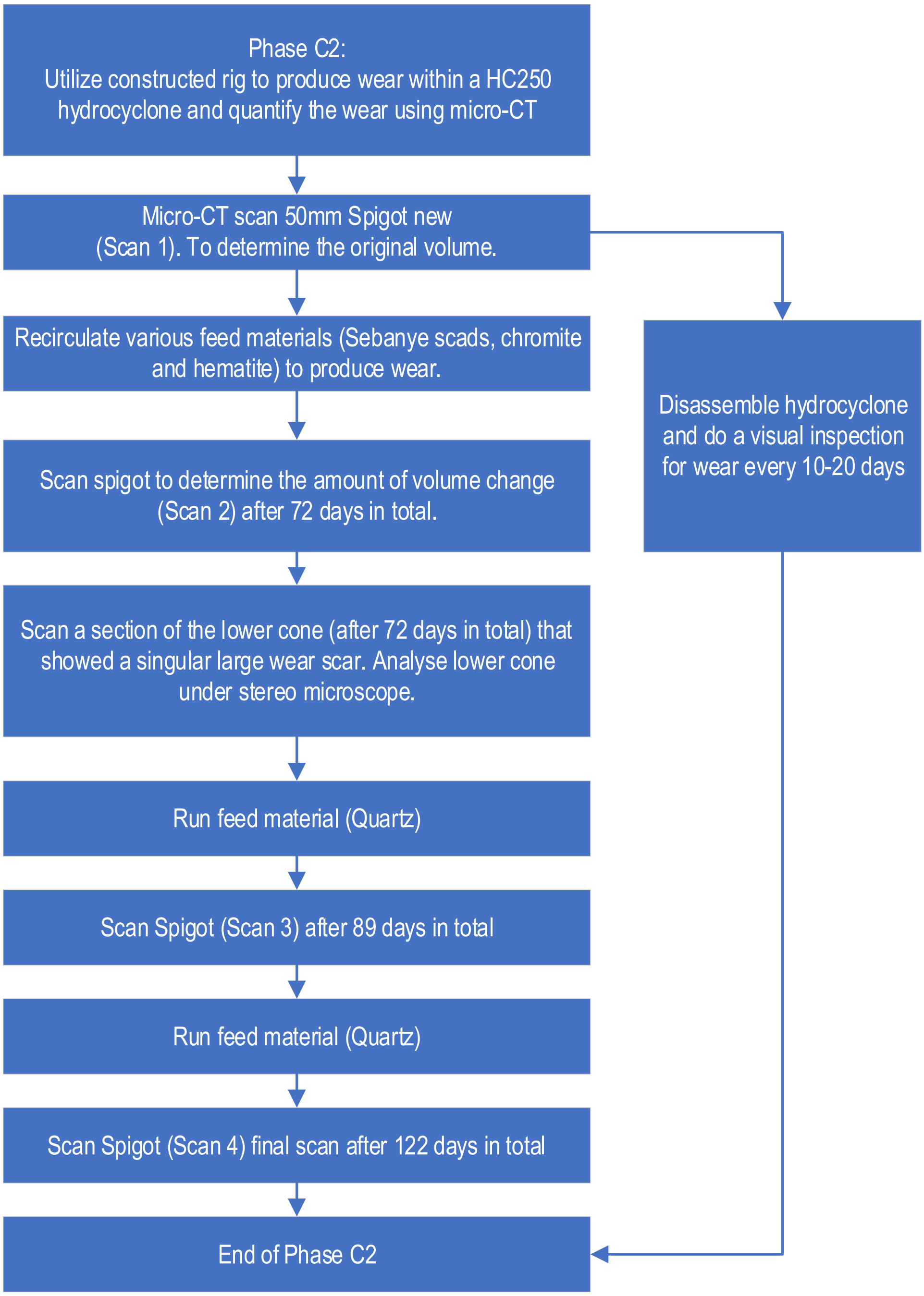

Figure 3.11: Summary of steps followed in Phase C2.

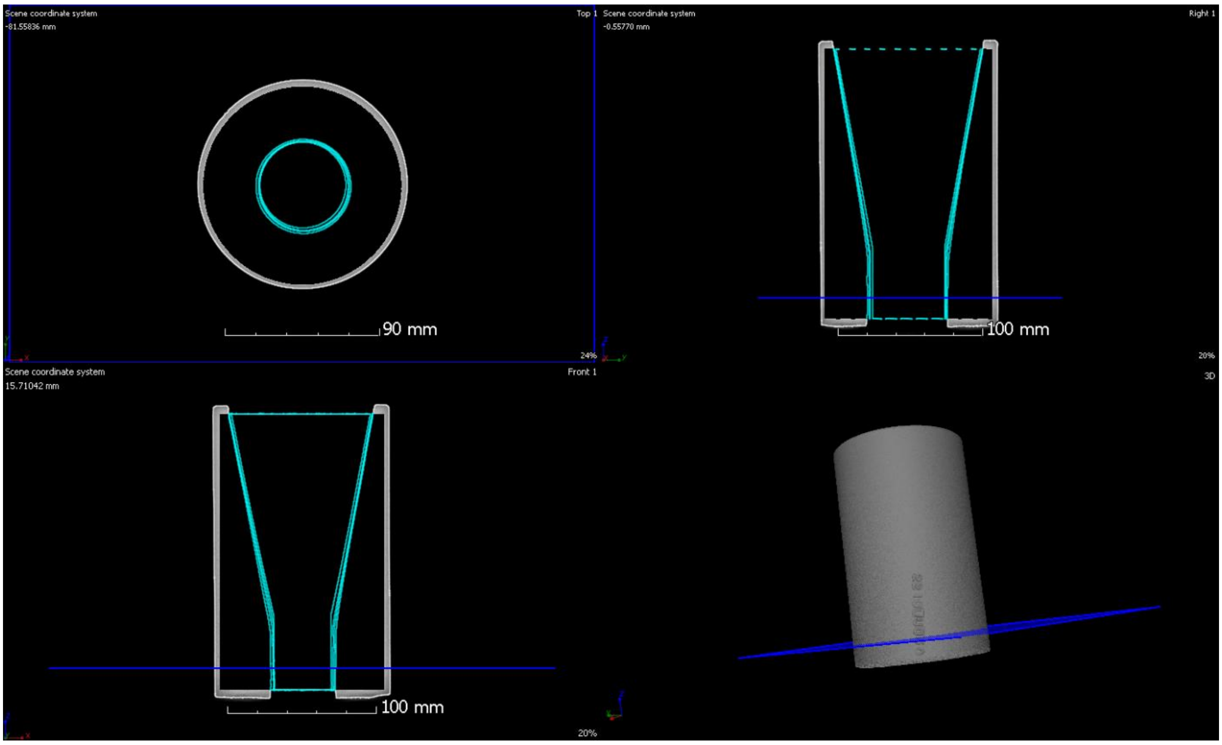

Figure 3.12: Three-dimensional view and orthographic projections of a section of HC250-15-1/A-B/50 PU (Elasturan 6055/115) spigot, as shown by VGSTUDIO MAX software.

Table 3.2 shows that the spigot was scanned new and after 72, 89 and 122 days in operation (the number of scans that could be completed and their interval was subject to availability of the micro-CT scanner). Destructive test work (sample sectioning, stereomicroscopy and micro-CT) was performed on the NR lower cone after 72 days, owing to a large singular wear groove that was observed. Thereafter, a new lower cone was installed that was used in the efficiency test described in Phase C4.

Table 3.2: Timeline of microcomputed-tomography scans on HC250-15-1/A-B/50 parts.

Abrasive material	Time (days)	Total (days)	Scan no.	Component
None	0	0	1	Spigot
Scads* 1	7	7	None	N/A
Scads 2	16	23	None	N/A
Chromite	14	37	None	N/A
Hematite ore	35	72	2	Lower-cone, spigot
Quartz 1	17	89	3	Spigot
Quartz 2	33	122	4	Spigot

*Gold ore tailings.

The volume of data produced from the four scans could be used to determine the wear rate of the hydrocyclone spigot that was subjected to recirculation of the various feed materials listed in Table 3.2 and Table 3.3. Different feed materials were used, with the expectation that different wear rates would be observed. The feed properties and conditions used to produce wear in the hydrocyclone are listed in Table 3.3.

Table 3.3 Feed materials and conditions used to produce wear in HC250-15-1/A-B/50 hydrocyclone.

Material	SG	P80 (µm)	Duration (cumulative) (days)	Pressure (kPa)	Solids (mass%)
Scads 1	2.75	500	7	90–100	18–25
Scads 2	2.75	1800	16 (23)	90–100	18–25
Chromite	4.7	400	14 (37)	90–100	18–25
Hematite	5.25	1670	35 (72)	100–110	18–25
Quartz 1 and 2	2.65	1700	50 (122 total)	75–80	18–25

It was originally envisioned that the feed pressure, PSD, water level and solids concentration would be held constant throughout the period of recirculation of the feed. This was difficult to practically achieve because the rig was left to run for 24 hours per day for several weeks and could not be monitored at all times. Owing to spillage, minor leaks and vaporization, the feed RD changed with time; the particle size and shape also changed due to recirculation attrition. The feed pressure fluctuated as the water level and RD changed. Therefore, it can be stated that the feed conditions did not remain entirely constant: the measured wear rates should be viewed within this framework.

The PSD of the fresh feed materials is presented in Figure 3.13. PSDs were not measured after recirculation because they constantly changed. The −3 mm scads, quartz and hematite had coarse PSDs, with P50 values of 1.2 mm, 0.72 mm and 1 mm, respectively. These materials were recirculated for the longest periods. The PSDs of chromite and the −1 mm scads were significantly finer.

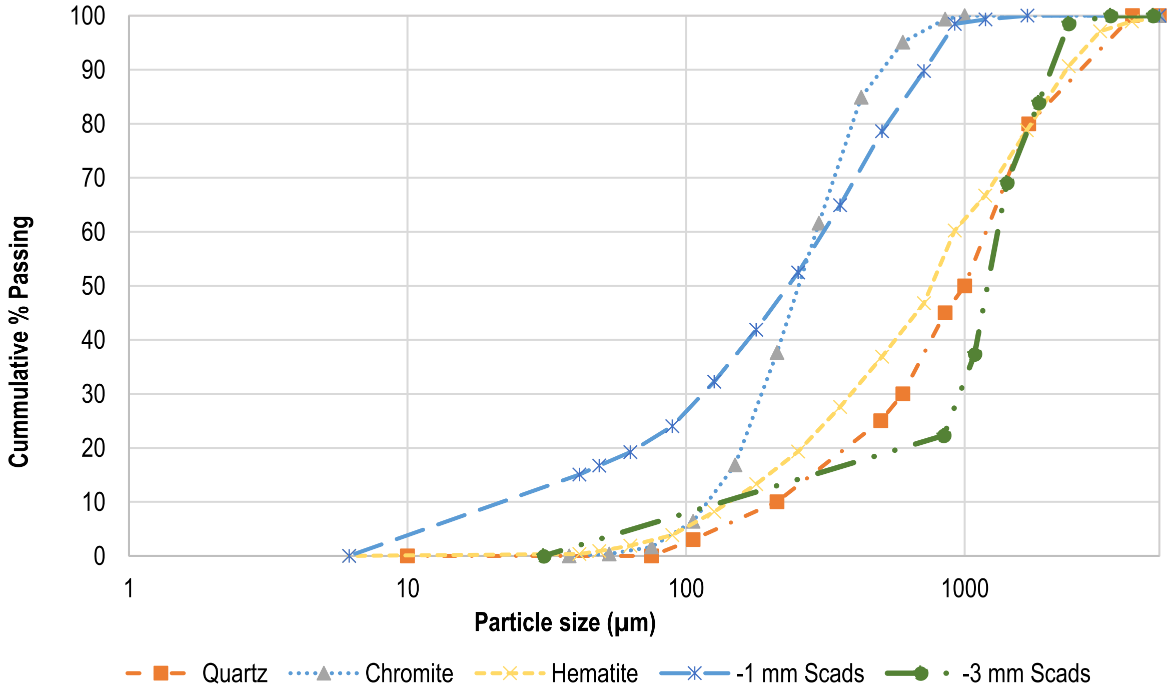

Figure 3.13: Initial particle size distribution of −1 mm scads (Scads 1), −3 mm scads (Scads 2), chromite, hematite and quartz feeds used to produce wear in the rig.

3.4.3 Phase C3

The test rig was modified after Phase C2 to install automatic samplers that could be used in the efficiency test. An overview of the activities of Phase C3 is illustrated in Figure 3.14.

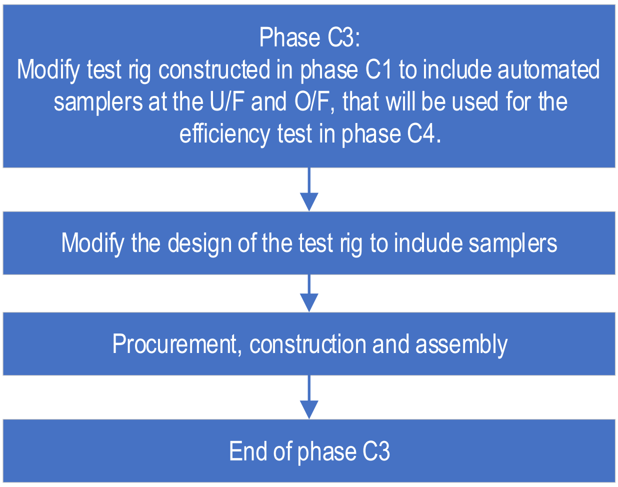

Phase C3:
Modify test rig constructed in phase C1 to include automated samplers at the U/F and O/F, that will be used for the efficiency test in phase C4.

Modify the design of the test rig to include samplers

Procurement, construction and assembly

End of phase C3

Figure 3.14: Summary of steps followed in Phase C3.

It was recommended (by Multotec Sampling) that samplers should be used for the hydrocyclone efficiency test. The basis for this recommendation was that samplers can reduce the bias relative to manual sampling and increase the precision (Stanley, 1987). Mechanical sampling is also less labour-intensive.

The overflow stream was sampled using a timed vezin sampler (Multotec 150-TVS-1/20) (Figure 3.15(**a**)). The underflow (spigot) stream was sampled using a cutter boom stacker (Multotec 150-BSS-20) (Figure 3.15(b)).

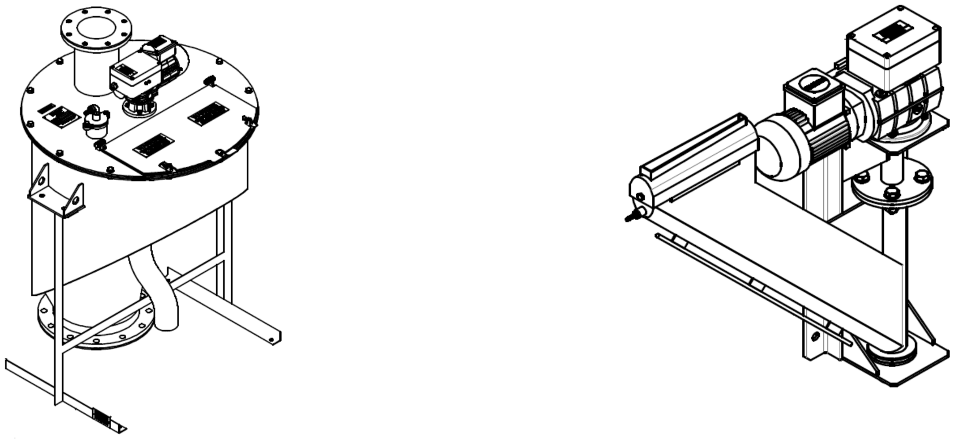

a)

b)

Figure 3.15: (a) Timed vezin sampler 150-TVS-1/20 used to sample the hydrocyclone overflow. (b) Cutter boom stacker 150-BSS-20 used to sample the underflow.

The conceptual design of the modified rig is illustrated in Figure 3.16. The timed vezin sampler is visible below the overflow pipe and the cutter boom stacker is seen below the spigot of the hydrocyclone.

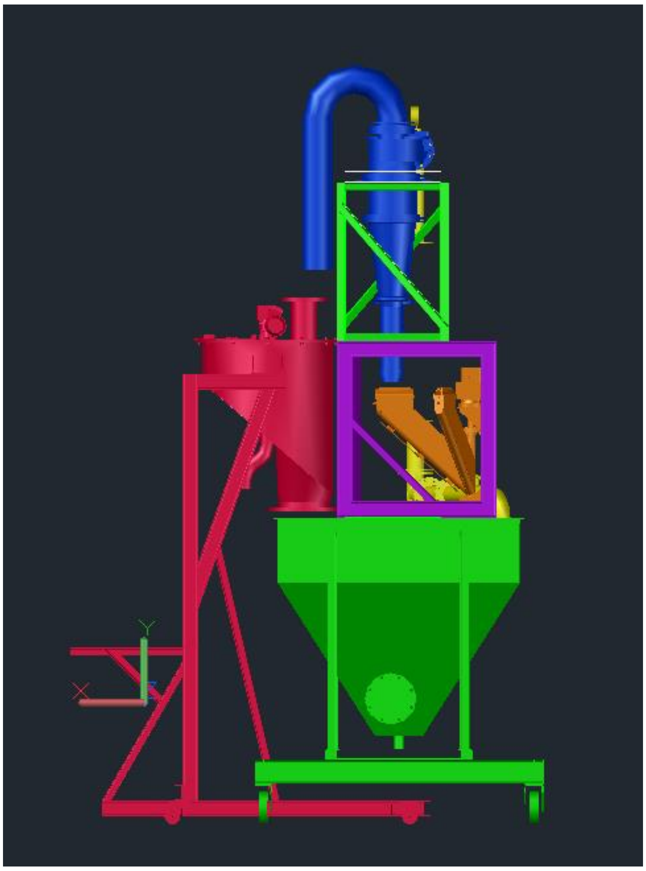

Figure 3.16: Timed vezin sampler 150-TVS-1/20 shown below the overflow pipe and cutter boom stacker 150-BSS-20 shown below the hydrocyclone spigot.

3.4.4 Phase C4

The modified test rig constructed in Phase C3 was used to compare the efficiency of the worn spigot (after 122 days of recirculation) with that of a new 50 mm spigot. An overview of Phase C4 is illustrated in Figure 3.17.

Both tests were carried out using the same hydrocyclone (HC250-15-1/A-B/50): only the effect of spigot wear on efficiency was evaluated. The rubber lining in the cone was replaced before conducting the efficiency test to ensure that spigot wear was the only geometric variable. The conditions used for the rig efficiency test are listed in Table 3.4. The operating conditions included pressure, feed density, motor speed and the amounts of water and solids added to the rig. The feed pressure fluctuated slightly (± 4 kPa).

The efficiency tests were carried out using homogenised silica that consisted of fine and coarse material that was blended at a mass ratio of 60:100, giving a combined feed with the PSD shown in Figure 3.18. Samples taken during the efficiency test are listed in Table 3.5.

Figure 3.17: Summary of steps followed in Phase C4.

Table 3.4: Efficiency test conditions for new and old HC250-15-1/A-B/50 spigot on modified test rig.

Parameter	New spigot	Old spigot	Comment
Motor speed	1250 rpm	1250 rpm	Maximum was 1480 rpm
Water mass	609 kg	609 kg	Amount of water added to the rig
Fine material	100 kg	100 kg	Fine quartz
Coarse material	60 kg	60 kg	Coarse quartz (Green Sands)
SG, silica	2.65	2.65	
Pressure	± 70 kPa	± 70 kPa	± 4 kPa fluctuation
U/F samples	3	3	35 cuts per bucket
O/F samples	3	3	10 cuts per bucket
Run time per bucket	± 70s	± 70s	35 and 10 cuts taken over 70 s
Vezin, time setting	5 s	5 s	actual was 7 s (controller error)
Boom, time setting	0.65 s	0.65 s	actual was 2 s
Boom cutter speed	0.54 m/s	0.54 m/s	at Radius 580mm, middle
Vezin speed	0.32 m/s	0.32 m/s	at Radius 230mm, middle
Cutter width	20 mm	20 mm	Single cutter
Actual feed RD	1.138	1.128	Standard deviations were 0.00467 (new) and 0.0011 (old)
Feed solids by mass	20.81%	20.81%	Calculated value (160 kg solids, 609 kg water)
Feed solids by mass	19.35%	18.16%	Measured value

Table 3.5: Samples taken during efficiency test.

Test	Sample	Comment
Old spigot (T1)	Feed sample 1 (T1F1)	Taken from bypass valve, not used in partition curve
	Feed sample 2 (T1F2)	Taken from bypass valve, not used in partition curve
	Feed sample 3 (T1F3)	Taken from bypass valve, not used in partition curve
	O/F sample 1 and U/F sample 1	Taken over 70 s with auto samplers
	O/F sample 2 and U/F sample 2	Taken over 70 s with auto samplers
	O/F sample 3 and U/F sample 3	Taken over 70 s with auto samplers
New spigot (T2)	Feed sample 1 (T2F1)	Taken from bypass valve, not used in partition curve
	Feed sample 2 (T2F2)	Taken from bypass valve, not used in partition curve
	Feed sample 3 (T2F3)	Taken from bypass valve, not used in partition curve
	O/F sample 1 and U/F sample 1	Taken over 70 s with auto samplers
	O/F sample 2 and U/F sample 2	Taken over 70 s with auto samplers
	O/F sample 3 and U/F sample 3	Taken over 70 s with auto samplers

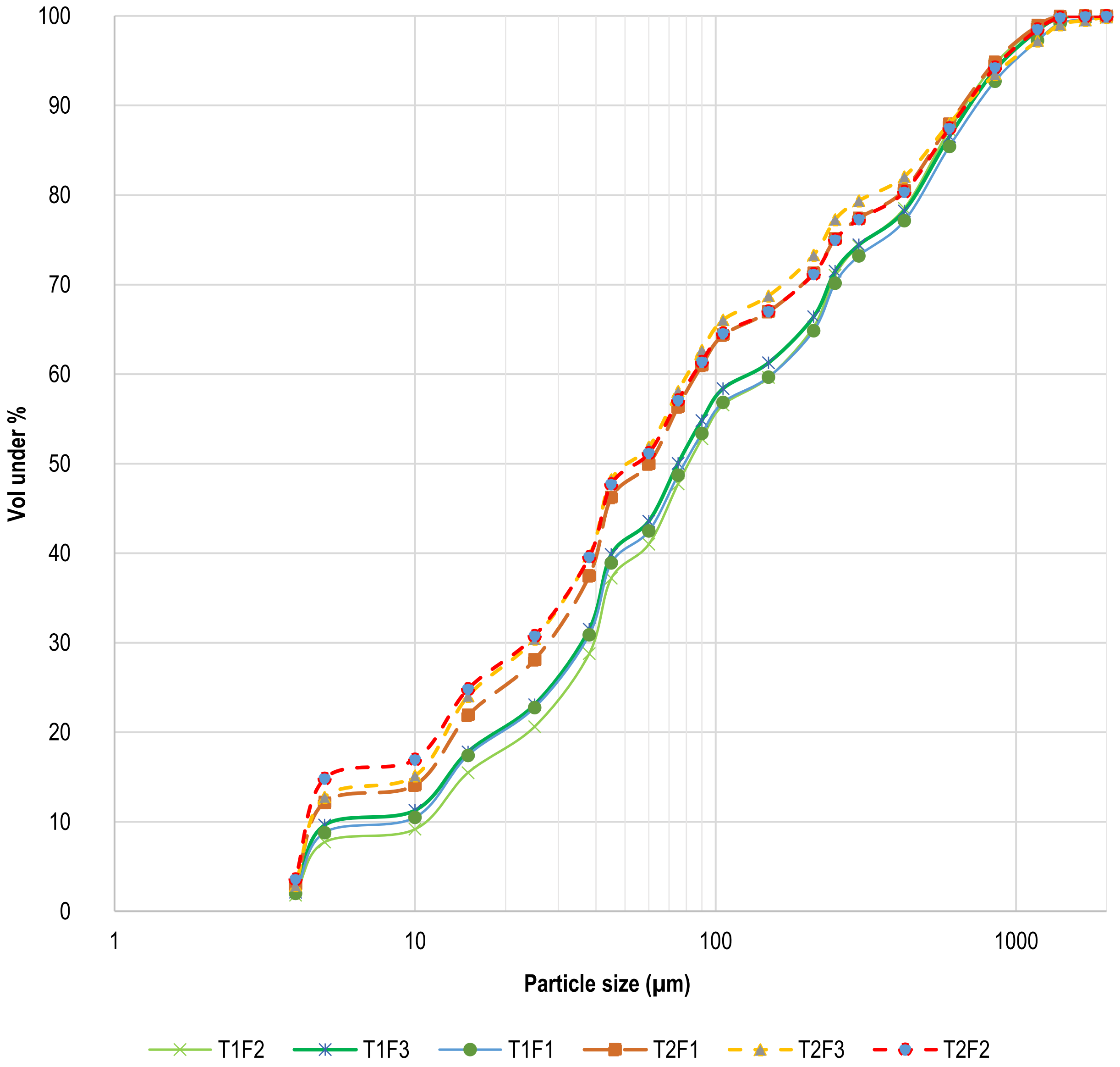

Figure 3.18: Particle size distribution of feed used for Tests 1 (T1, old spigot) and 2 (T2, new spigot). Three manual samples were taken for each test, F1, F2 and F3 (feed). Particle size distribution was measured using a Malvern Mastersizer.

Before the samples were taken, the feed RD was calculated and monitored from a sample taken from the bypass valve until a relatively constant value was measured for three consecutive samples (standard deviation of ± 0.001). Thereafter, three feed samples were manually taken from the bypass valve. The underflow samples were taken automatically using the boom cutter over a time interval of 70 s; 35 cuts were taken. The overflow was simultaneously automatically sampled by the timed vezin, but only ten cuts were taken over 70 s. This process was repeated three times. The same process was followed for the worn spigot.

The overflow and underflow flowrates were calculated using Equation 3.1 (Multotec), which is based on the cutter speed of the sampler, the width of the cutter and the volume of the sample measured per cut:

$$Volume\ of\ sample\ (l) = \frac{Flowrate\left(\frac{m3}{h}\right) \times Cutter\ width\ (mm)}{3600 \times Cutter\ speed\ (m/s)} \tag{3.1}$$

Each sample was weighed, filtered, dried and weighed again to determine the percentage solids. The dried sample was then split into smaller sub-samples using a rotary splitter, one of which was analysed using a Malvern Mastersizer to determine the PSD.

The solids concentrations, flowrates and PSDs of the underflow and overflow were used to determine the mass of each size fraction in a sample. The mass of each size fraction of the feed could be calculated and the recovery of each size fraction to the under- and overflows determined. The corrected recovery curve was calculated using Equation 2.3, with a mathematical transformation method by selecting α_w to be the minimum recovery to the underflow. (The Kelsall method yielded inconclusive results due to the presence of a fish-hook effect.)

3.5 Phase D: Wear Analysis of VV165

3.5.1 Phase D1

An overview of the activities of Phase D1 is illustrated in Figure 3.19.

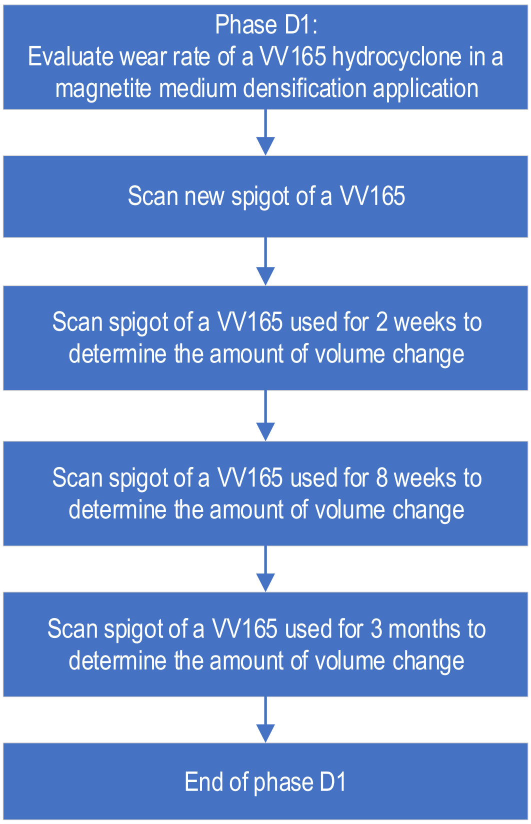

Figure 3.19: Summary of steps followed in Phase D1.

Exxaro requested an investigation of the wear rate of 165 mm Dc polyurethane (Multotec, VV165) densification cyclones (Figure 3.20). These cyclones are used for magnetite densification at Grootegeluk coal mine, Mpumalanga, South Africa. The plant was concerned about replacement rate of the hydrocyclones and wanted to determine the wear rate in this application. They were tested for wear after 14, 56 and 90 days in operation. The magnetite medium had a PSD of 80% passing 45 µm. Owing to size constraints, only the cyclones spigots were scanned, using the same micro-CT scanner shown in Figure 3.7, although the entire hydrocyclone was visually checked for any signs of wear. Different hydrocyclones of the same size and specification (VV165) were removed at different times to be scanned. These were replaced with new hydrocyclones during routine maintenance and this testing had minimal impact on the operational down-time.

Figure 3.20: VV165 hydrocyclone used as a medium densification cyclone.

CHAPTER 4: RESULTS AND DISCUSSION

4.1 Phase A: Material Properties

4.1.1 Phase A1

The measured material properties of NR are compared with those of PU (Elasturan 6055/114) in Table 4.1. The Shore A hardness, tensile strength and Young's modulus of PU were higher than those of NR. NR had higher ultimate elongation value and modulus of resilience. NR is an elastomeric polymer and its wear-resistance mechanism is based on its ability to deflect the energy of impinging particles (Stachowiak and Batchelor, 2014). PU had a higher tensile strength, higher Young's modulus and higher hardness. PU therefore has the advantage of not requiring a metal shell, unlike that of an NR-lined hydrocyclone.

Table 4.1: Material properties of vulcanized natural rubber compound and polyurethane Elasturan 6055/114 used in HC250-15-1/A-B/50 hydrocyclone.

Property	Unit	NR	PU
Density	SG	1.1	1.12
Hardness	Shore A	51	87.5
Tensile strength*	MPa	19	42.2
Young's modulus*	MPa	0.8	9.2
Ultimate elongation*	%	1216	913
Abrasion (DIN)	mm^3	100	37
Modulus of resilience*	MPa	7.5	5
Surface roughness, Sa	µm	1.1	3.24
Static friction coefficient		0.12	0.25

**Tensile test graphs and results are shown in Appendix D.*

The DIN abrasion value listed in Table 4.1 (amount of material lost) was higher for NR, but it has been reported that NR compounds can last longer than PU in certain applications (Jones, 2011). These data showed that the DIN test does not give a reliable method to compare the wear resistance of polymers in a slurry erosion environment.

Surface roughness profiles of sampled areas of NR and of the thermosetting PU (Elasturan 6055/114) are shown in Figure 4.1 and Figure 4.2, respectively. The surface roughness (Sa = 1.1 µm) of NR was relatively smooth compared with that of PU (Sa = 3.24 µm). Other surface profile properties are listed in Table B.2 in Appendix B.

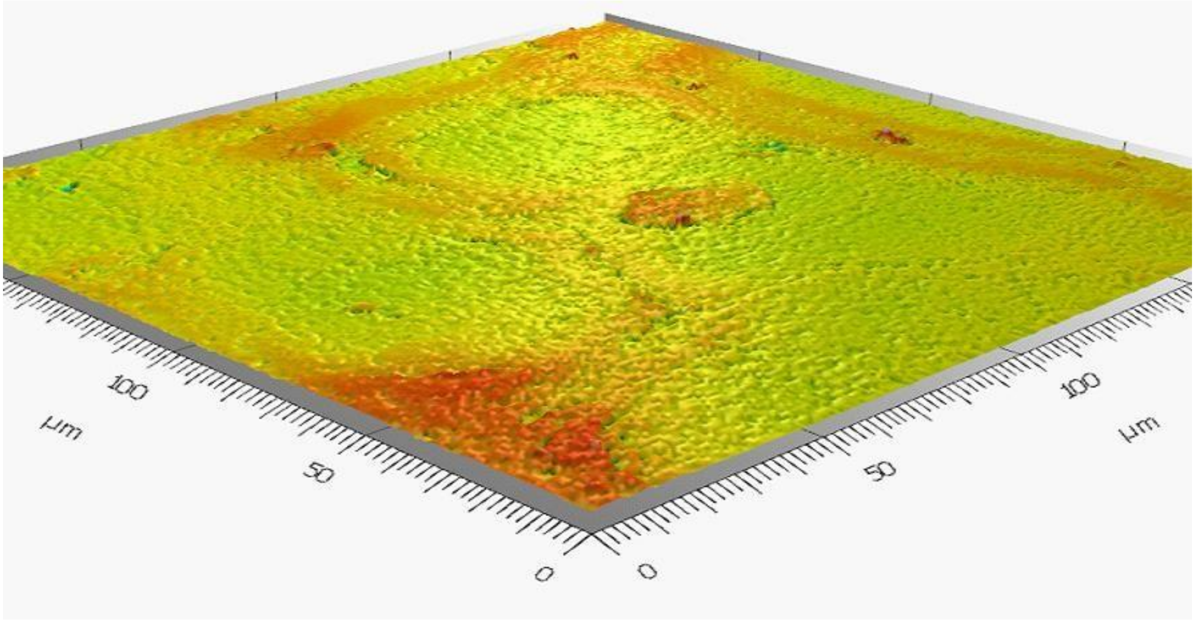

Figure 4.1: Three-dimensional view of rubber surface showing relative roughness, measured by optical profilometry.

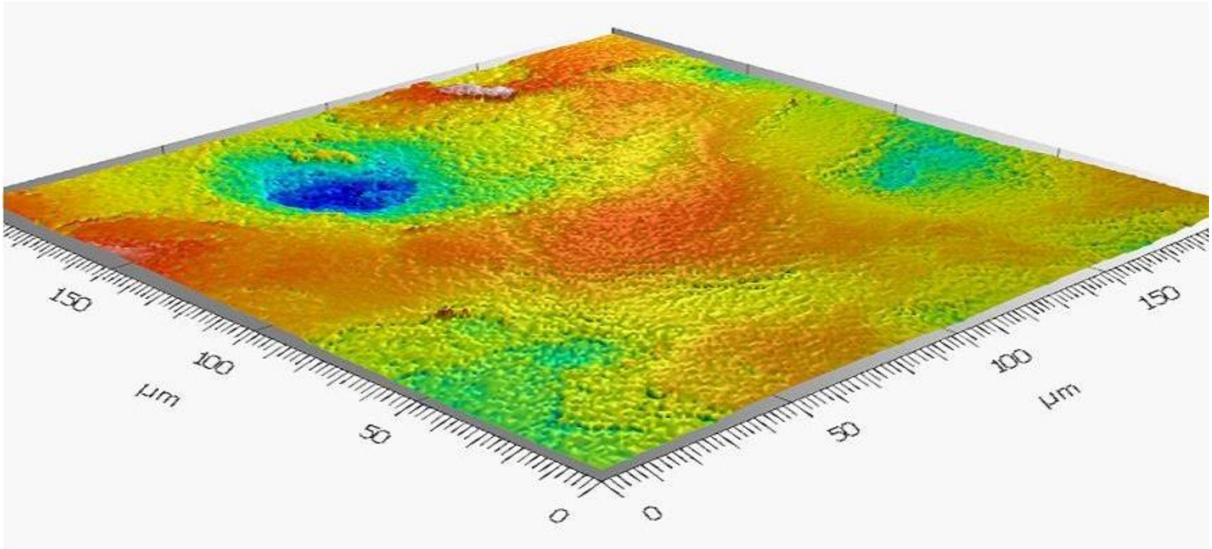

Figure 4.2: Three-dimensional view of polyurethane surface showing relative roughness, measured by an optical profilometry.

4.1.2 Phase A2

Abrasion tests on vulcanized NR with different hardness values were carried out. The ASTM D5963 test method was selected based on its availability, rather than on its suitability for erosive wear applications. The test methods recommended in Section 2.5 could not be conducted, because they were not readily available or up to standard at the time of testing.

The abrasion resistance of four vulcanized NR samples was tested using a rotary drum abrader similar to that illustrated in Figure 2.20. The results of material loss as a function of the Shore A hardness are shown in Figure 4.3. The best abrasion resistance (two-body mode) was given by the NR with a Shore A value of 42, which was the softest sample tested. The hardness value of the rubber lining in the HC250 hydrocyclone was Shore A 51, as shown in Table 4.1.

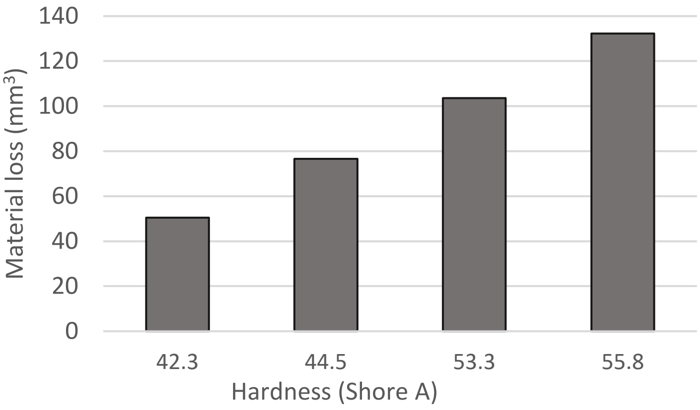

Figure 4.3: Effect of Shore A hardness for different vulcanized natural rubbers on rotary drum abrader material loss according to ASTM D5963.

These results corresponded to the findings observed in Figure 2.29, which showed that a softer NR, with a lower Young's modulus, displayed the highest erosion resistance when using the jet erosion test (Arnold and Hutchings, 1991). However, a suitable rubber should also have the properties listed in Table 2.6, most notably a high gouging resistance (Arnold and Hutchings, 1991; Xie et al., 2019). It has been observed that relatively soft NR compounds (with IRHD hardness ~ 38) are used in very abrasive slurry applications (such as ferrochrome slag processing) with very good results; however, wear life is reported to be highly application-specific and NR has not worked equally well for all applications.

In future work, it is suggested to test various NR compounds with different mechanical properties, preferably using an in-situ hydrocyclone test or a laboratory wear test, such as the SJE, Coriolis or slurry pot (ASTM G119) tests, to yield conclusive results concerning optimisation of the wear life of NR, based on the low-angle erosive wear that is applicable to hydrocyclone applications (Xie *et al.*, 2019). It is also suggested to use sharp and large abrasive particles to test gouging resistance. The same methods can be used to compare the performance other polymers (such as the BASF PU Elasturan range listed in appendix E table E.1

4.2 Phase B: Quantifying Wear

4.2.1 Phase B1

Photographs of wear on worn-out hydrocyclone components are shown in Figure 4.4 to 4.6. The images in Figure 4.4 and Figure 4.5 were taken of a VV350 PU hydrocyclone in a −0.5 mm feed coal classification application; those in Figure 4.6 were taken of the same type of hydrocyclone in a −3 mm feed ferrochrome classification application.

Figure 4.4 to 4.6 (see also Figure 4.7) show that a helicoidal wear pattern formed on selected components. These helicoidal grooves resembled the flow pattern typically found in hydrocyclones (Flintoff and Kuehl II, 2011). The wear grooves also resembled low-impingement-angle (~20°) wear grooves, as illustrated by Figure 2.25 (Xie *et al*., 2015). It was visually observed that the highest wear generally occurred at the spigot (Figure 4.5); the area of second-highest wear was at the cone and connection points of the cone and spigot (or lower cone, if present), as shown in Figure 4.4. In some cases (as observed for coal applications), the vortex finder also showed a high amount of wear, as displayed in Figure 4.5(a). These observations are consistent with the findings of Olson and Turner (2002).

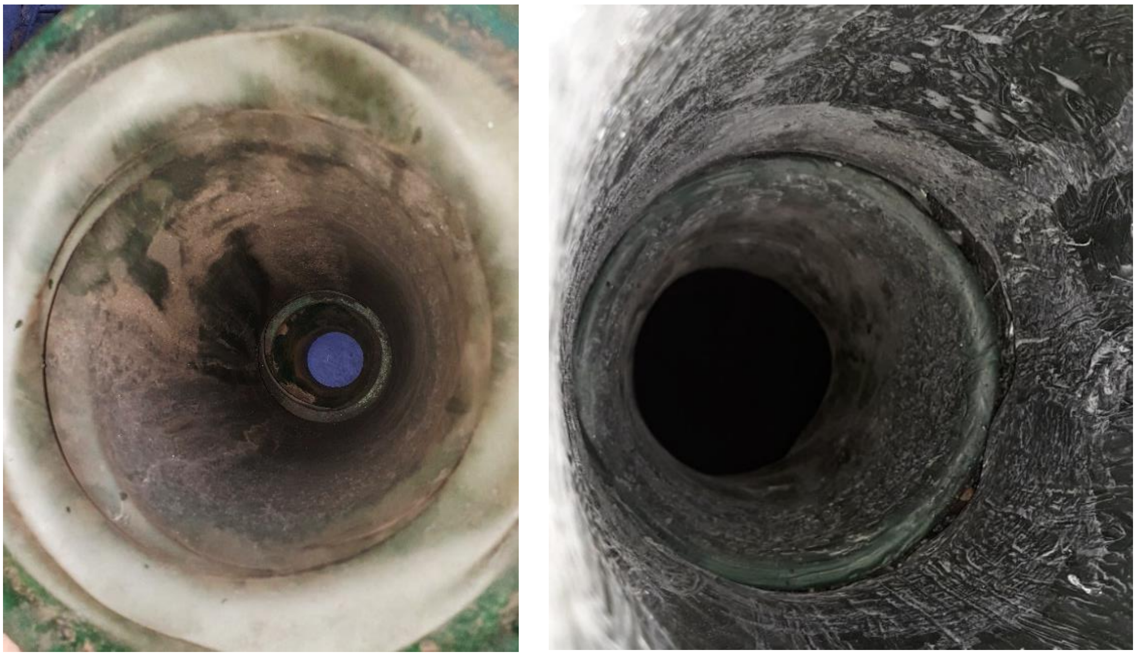

a) b)

Figure 4.4: Photographs of wear of a VV350 cyclone used in a coal application. (a) Upper connection point of lower cone; (b) connection point between lower cone and spigot.

a) b)

Figure 4.5: Photographs of wear of a VV350 cyclone used in a coal application. (a) Worn vortex finder (note that there is only significant wear visible on the vortex finder and not on the inlet or barrel), (b) inside the spigot.

a)

b)

Figure 4.6: Photographs of wear of a VV350 cyclone used in a ferrochrome application, showing the wear within the polyurethane spigot.

The higher wear in the spigot and lower cone (or bottom of cone if there was no lower cone) could relate to the findings shown in Figure 2.4 (Ghodrat *et al*., 2013) and Figure 2.7 (Chang *et al*., 2011), which showed that the lower regions of a hydrocyclone experienced a much higher solids concentration and therefore a larger number of impinging particles. The particle size is also larger in this region and therefore requires a smaller critical velocity to cause wear (Iwai and Nambu, 1997). The reasons for higher wear rates (relative to the barrel and inlet) observed at the vortex finder could be related the higher tangential and axial velocities observed at the vortex finder (Ghodrat *et al*., 2013; Wang and Yu, 2010), with the higher velocity being the driving force for wear based on the power-law relationship between velocity and wear (Stachowiak and Batchelor, 2014).

4.2.2 Phase B2

A preliminary investigation was carried out to determine whether it would be feasible to analyse and quantify hydrocyclone wear using micro-CT scans. The first proof-of-concept scan, shown in Figure 4.7, was performed on a worn lower cone of a Multotec VV range PU hydrocyclone (origin unknown). Spatial thickness distributions, density and volume measurements were easily calculated using the 3D rendering software VGSTUDIO MAX. This experiment confirmed that the use of a micro-CT scan makes quantification of exact wear profiles possible.

The second proof-of-concept scan was performed on a randomly selected new VV250 PU lower cone, shown in Figure 4.8. In this case, X-ray scatter occurred at the upper section (larger diameter) of the lower cone due to steel reinforcement within this section and the inability of the X-rays produced by the 225 kV X-ray source to penetrate the higher density metal. Therefore, it was determined that, owing to size restrictions on the sample of 400 mm × 400 mm (Hoffman and Beer, 2012) and X-ray scatter, it would not be feasible to fully analyse lower cone wear in a Dc 250 mm hydrocyclone using the Nikon XT H 225 ST micro-CT scanner.

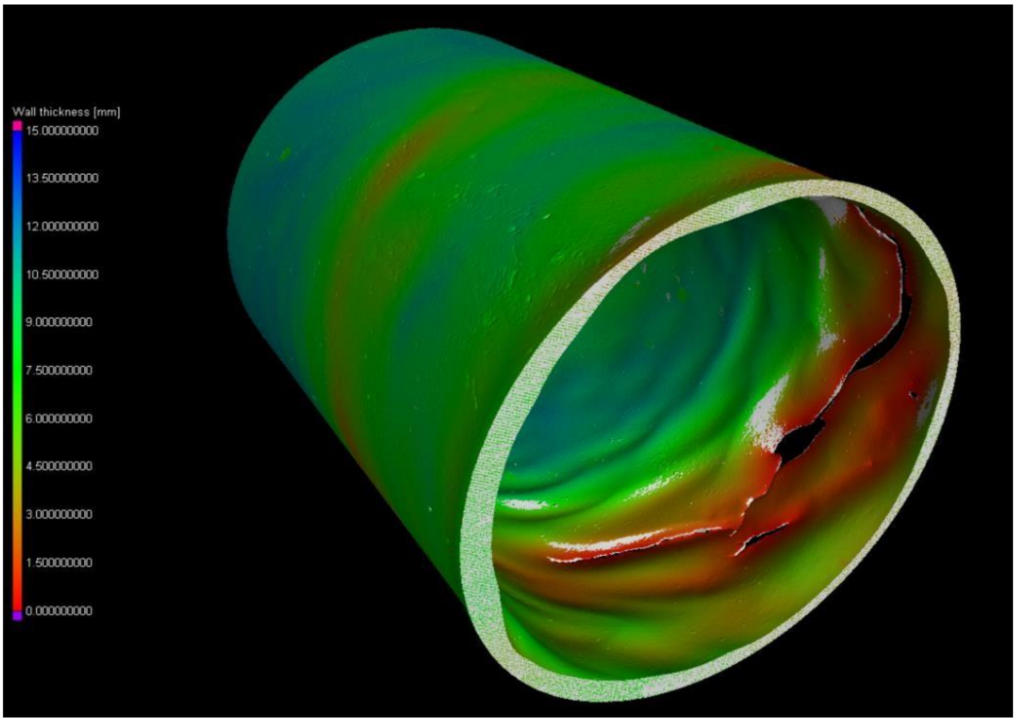

Figure 4.7: Microcomputed tomography scan (3D rendered object) of a worn lower cone, indicating the spatial distribution of the wall thickness (mm).

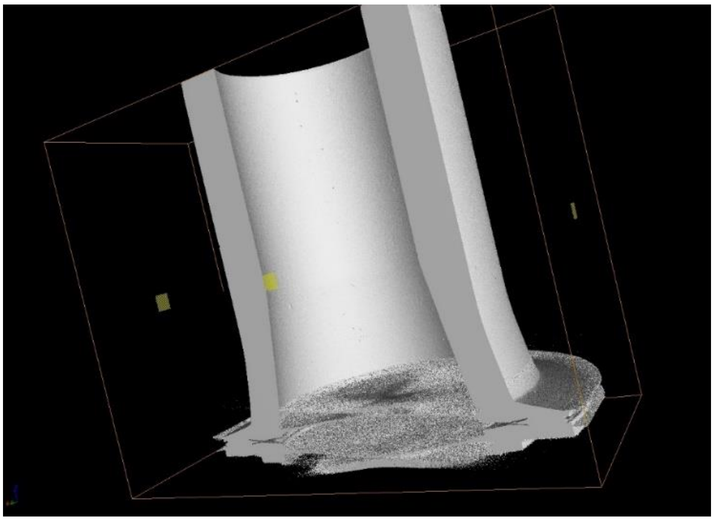

Figure 4.8: Shows the microcomputed tomography scan (3D rendered object) of a new VV250 PU lower cone. X-ray scatter is clearly visible.

The third proof-of-concept scan was carried out on a randomly selected new hand-cast PU (Elasturan 6055/114) spigot of a HC250 hydrocyclone, displayed in Figure 4.9. Numerous clearly visible voids were observed. It is known that hand-cast parts can be prone to various casting defects, as listed in Table E.5 in Appendix E (Clavier, 2008). Void formation is a function of the pouring technique, cleanliness of the mould, temperature (seasonal influence), viscosity, reaction temperature (exothermicity), mould and sprue design (Clavier, 2008). These factors should be taken into consideration to minimize void formation in hand-cast parts, because they could potentially lead to a lower wear life.

Figure 4.9 illustrates that the entire spigot could be scanned and analysed: the wear analyses carried out in Phases C2 and D1 therefore focused on the spigot.

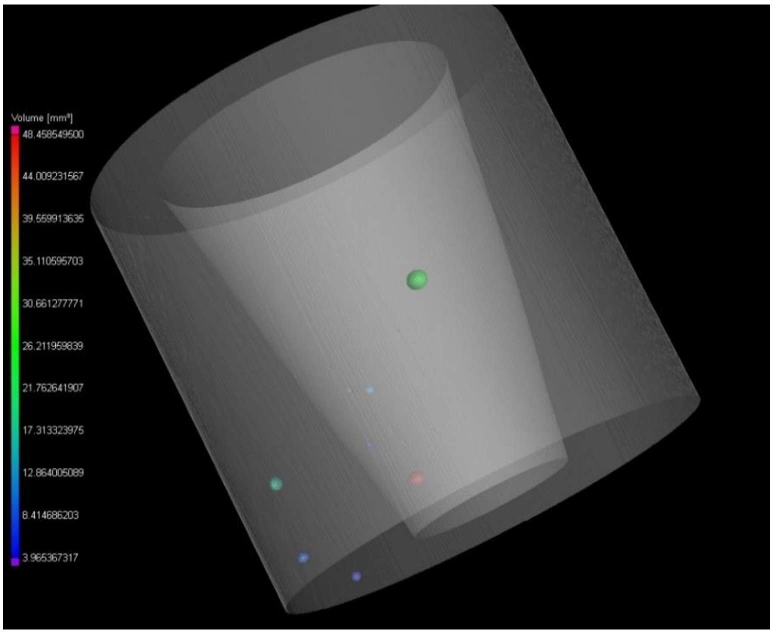

Figure 4.9: Microcomputed tomography scan of a hand-cast PU thermosetting (Elasturan 6055/114) 35 mm spigot with internal voids visible. The void sizes are indicated by the colour spatial distribution, with void sizes given in mm³.

4.3 Phase C: Wear and Efficiency Analysis of HC250 Hydrocylcone

4.3.1 Phase C1

The test rig that was constructed during Phase C1 is displayed in Figure 4.10.

a) *b)*

Figure 4.10: HC250-15-1/A-B/50 hydrocyclone test rig after construction, showing (a) front and (b) side views.

4.3.2 Phase C2

The wear produced and quantified in the HC250 hydrocyclone is discussed below. Micro-CT scans focused on the PU spigot; other parts of the hydrocyclone did not show signs of wear, based on visual inspection undertaken every 10 to 20 days (Figure 4.11). The only exception was the NR lower cone, which showed a significant wear scar that was visually detected after 72 days in recirculation.

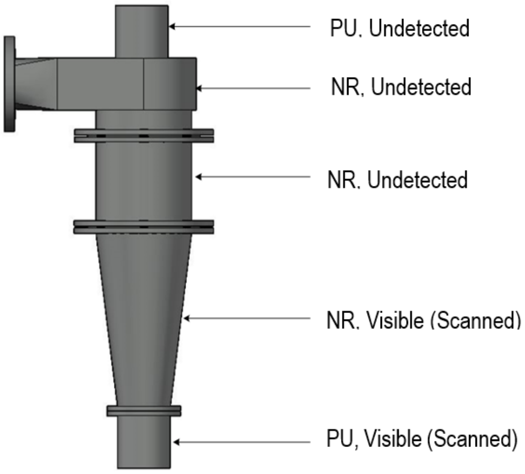

Figure 4.11: Schematic of different parts and materials of HC250-15-1/A-B/50 test rig and macroscopic indication of visible wear after 122 days of operation.

The inner spigot volumes for the four scans carried out after different operating periods (Table 3.2) are displayed in Figure 4.12; an enlarged image is shown in Figure 4.13 that shows the different wear durations. Figure 4.13 shows that if the operating period duration increased, the inner volume of the spigot increased due to wear.

The wear duration, percentage wear volume loss and wear rate (volume-based) are listed in Table 4.2. The volume loss was calculated from the difference in the spigot inner volume with time. The wear rate was calculated for the period between each scan (e.g., scan 4: (824 966 mm^3 – 795 708 mm^3)/33 days) = 887 mm^3/day).

Table 4.2: Effect of feed material and operating time on spigot inner volume and wear.

Material	Scan	Time (day)	Total (day)	Inner volume (mm^3)	Wear volume loss (%)	Wear rate (mm^3/day)
New spigot	1	0	0	725764	0	0
Scads 1	NM*	7	7	NM	NM	NM
Scads 2	NM	16	23	NM	NM	NM
Chromite	NM	14	37	NM	NM	NM
Hematite ore	2	35	72	777 905	7.18	724
Quartz 1	3	17	89	795 708	9.64	1047
Quartz 2	4	33	122	824 966	13.67	887

**NM – Not measured: the spigot was not scanned due to lack of availability*

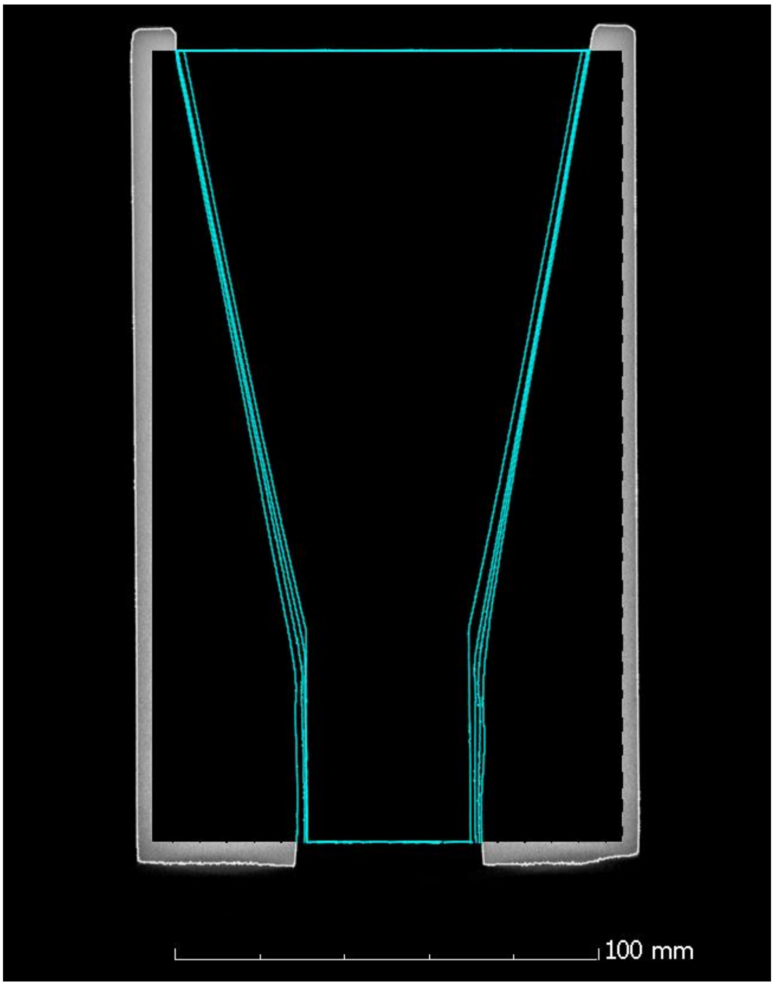

Figure 4.12: Orthographic view of a section of the wear profile within the spigot.

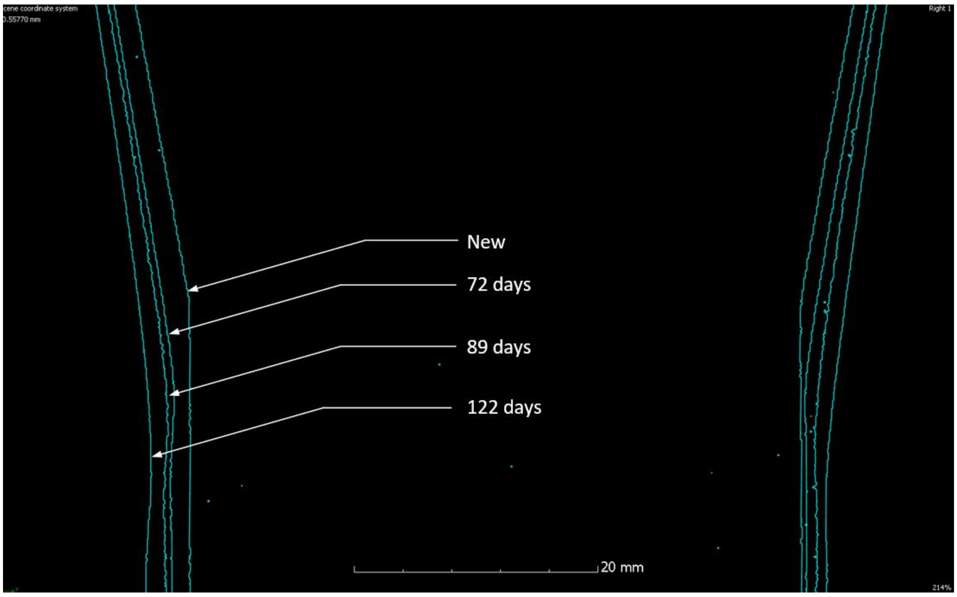

Figure 4.13: Enlarged view of the wear profile within the spigot that shows how the profile changed with time.

Table 4.2 shows that 13.67% of spigot volume was lost after 122 days (at this point the spigot had an inner diameter of 55 mm, i.e., a 5 mm increase from the new condition of 50 mm). The total volume lost by the spigot is plotted against time in Figure 4.14.

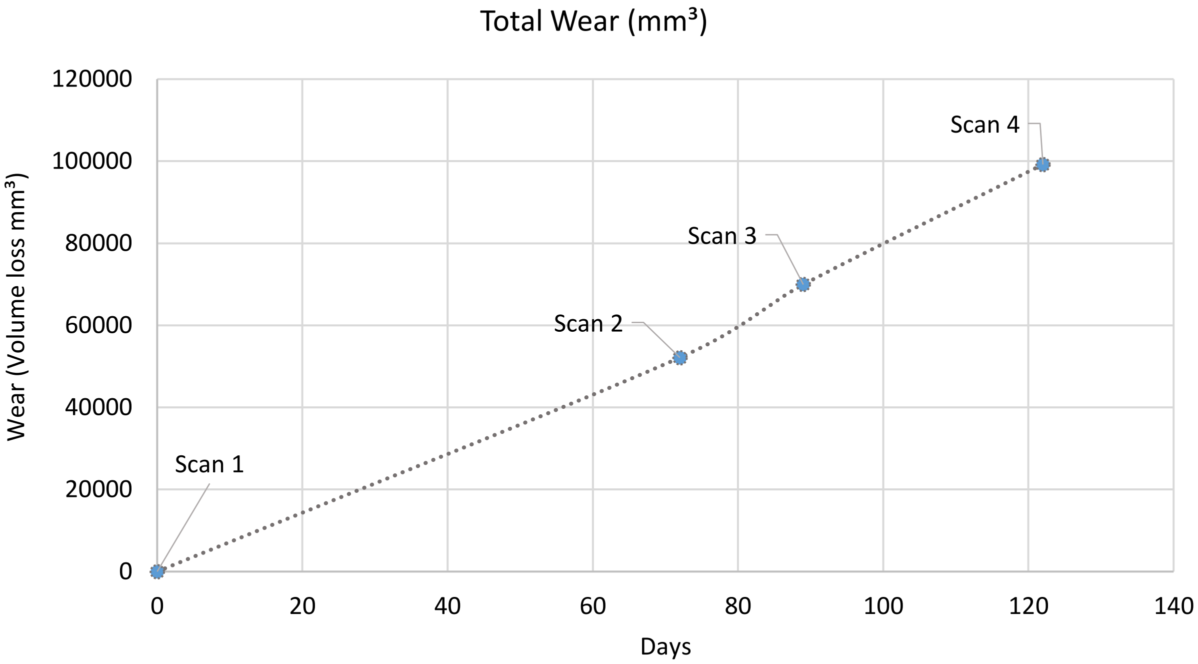

Figure 4.14: Total wear volume (as determined by microcomouted tomography) as a function of operating time.

Owing to the fact that different materials were used to produce the wear, no attempt was made to fit a model to the data points in Figure 4.14. The wear rates listed in Table 4.2 are illustrated in Figure 4.15.

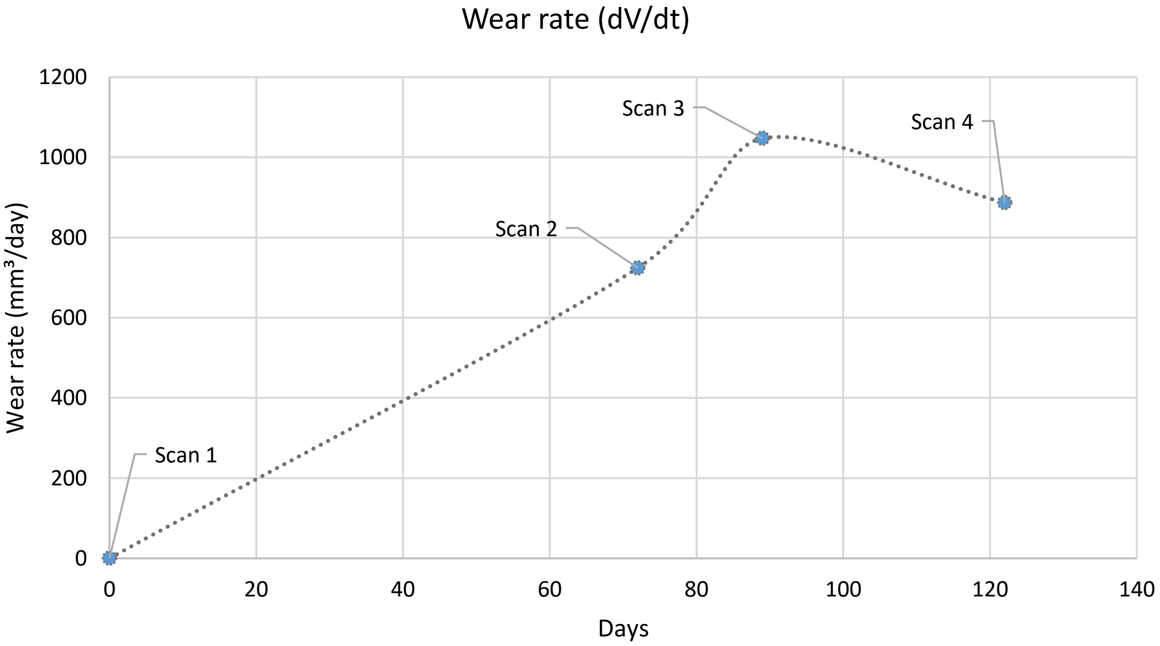

Figure 4.15: Calculated wear rate as a function of time. Note that betweens Scan 1 and 2, feed samples of scads, chromite and hematite were used to produce wear; between Scans 2 and 4, only quartz was used.

The wear rates produced by the recirculating rig were relatively low compared with those observed in highly abrasive applications (such as −3 mm ferrochrome slag), where spigot replacement often occurs from 14 to 30 days, depending on the spigot size and the application.

The most obvious difference between the test rig and industrial applications was that material was recirculated in the test rig. In industrial mineral classification applications, particles experience a much shorter retention time because material leaves the process with the tailings or concentrate and new material is constantly added (such as in a classification or tailings cyclone).

Figure 4.16 shows a photograph of (A) the fresh quartz feed used in the test rig and (B) the quartz particles after 3 days of recirculation in the rig. The particles became more spherical and smaller after a relatively short period (3 days) of recirculation. This result correlates with the findings illustrated in Figure 2.42 (Miller and Schmidt, 1987), which showed that particle roundness increased with extent of recirculation.

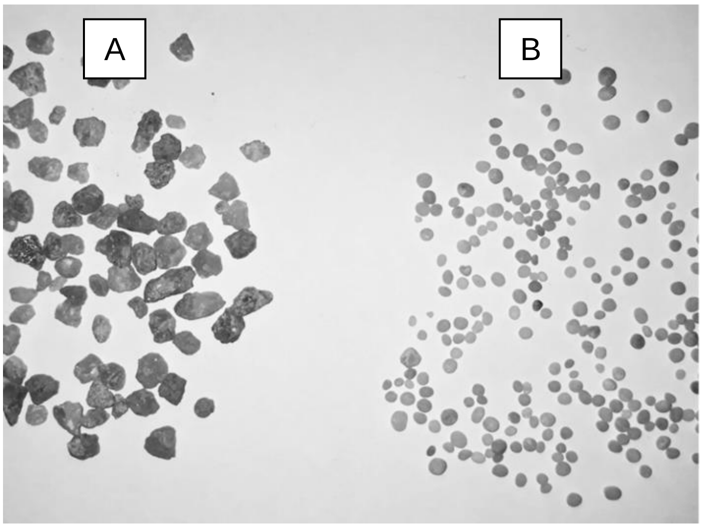

Figure 4.16: (A) Fresh quartz feed and (B) quartz particles after 3 days of recirculation.

Figure 4.15 shows that the wear rate for Scan 4 was lower than that of Scan 3, although the conditions remained the same (refer to Table 3.3, Quartz 1 and 2). The most likely reason for this is that the time between Scan 3 and 4 was longer, leading to more particle smoothening and a larger reduction in size; hence, the lower average wear rate over the 33-day period. This result relates to the findings of Walker and Hambe (2014), who showed that the wear rate decreased with an increase in particle roundness. It is also suggested that the significant influence of particle shape on wear can be directly related to the findings of Xie *et al.* (2019), who showed that polymers are more sensitive to particle shape, because gouging can more readily occur in the presence of large angular particles. These results highlight that particle shape is one of the primary driving forces of erosive wear in polymers, because particle shape influences the ability of a particle to transfer energy to the substrate material as higher localized applied stresses are applied (Desale *et al.*, 2006).

After 72 days of running different abrasive materials through the rig, with hematite being the last material, the NR wear lining showed a large singular wear groove. The lining was therefore removed and sectioned for destructive testing by analysis using a stereo-microscope and the micro-CT scanner. The single large (+8 mm width) wear groove located at the bottom of the cone is shown in Figure 4.17. The area of the cone that contained the large wear groove displayed in Figure 4.17 was cut out and scanned at a higher resolution to investigate the interior of the material. Side and top views of section A–A are shown in Figure 4.18(a) and (b), respectively.

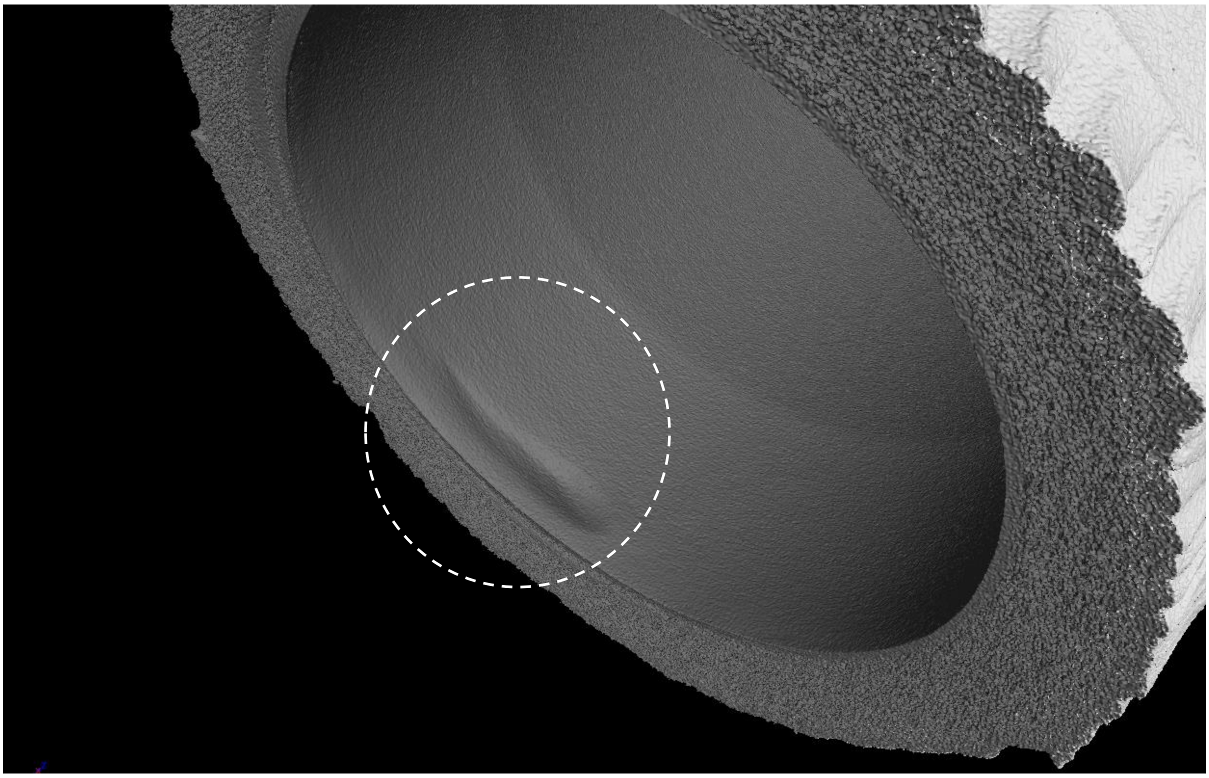

Figure 4.17: Microcomputed-tomography scan of HC250-15-1/A-B/50 vulcanized NR wear lining at the bottom of the cone.

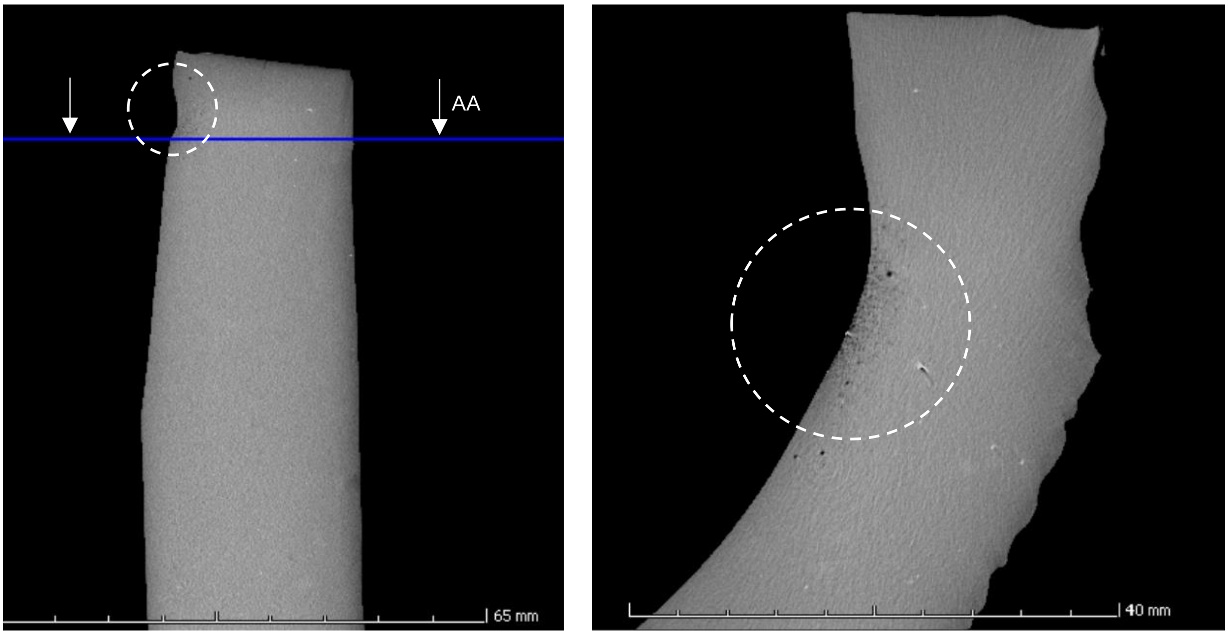

a) *b)*

Figure 4.18: Micro*computed tomography* scans of HC250-15-1/A-B/50 vulcanized NR wear lining section of the cone, showing (a) side and (b) the top views of the wear groove shown in *section A–A.*

Figure *4.18* shows that higher porosity was present within the encircled localized area of the large wear groove, as displayed in Figure *4.18*(b) and the enlarged image shown in Figure 4.19. Therefore, it can be stated that the large singular wear groove was caused by high localized porosity in that area. Porosity is a manufacturing defect that can be minimised by optimizing the compression-moulding process (Clavier, 2008).

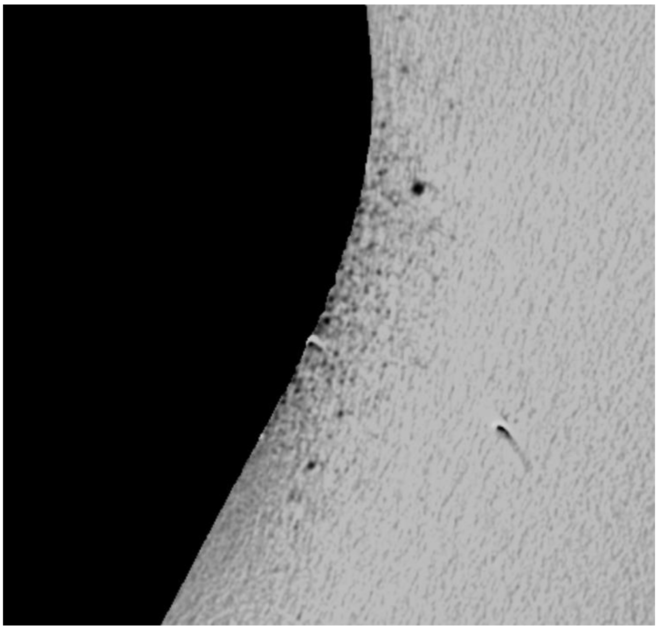

Figure 4.19: Enlarged view of circled area of interest shown in Figure 4.18*(b).*

Other smaller wear sites (scars) on the NR wear lining were also observed throughout the cone. One of these is indicated by the ellipsoid in Figure 4.20. The slurry flow direction is evident based on the orientation of the wear scar ‘tail’, as indicated by the arrow in Figure 4.20. It would be reasonable to suggest that the abrasive particles first formed a gouge or chip (indicated by A in Figure 4.20) in the material and then the tail (indicated by B) formed by low-angle impinging particles that collided with the edge of the gouge. This wear mechanism relates to that illustrated in Figure 2.27, but, in the latter case, the notch was caused by a gouge or chip in the material that increased in size as wear progressed (Arnold and Hutchings, 1991). The pattern also resembled that of low-angle wear in an SJE test (Xie *et al.*, 2015).

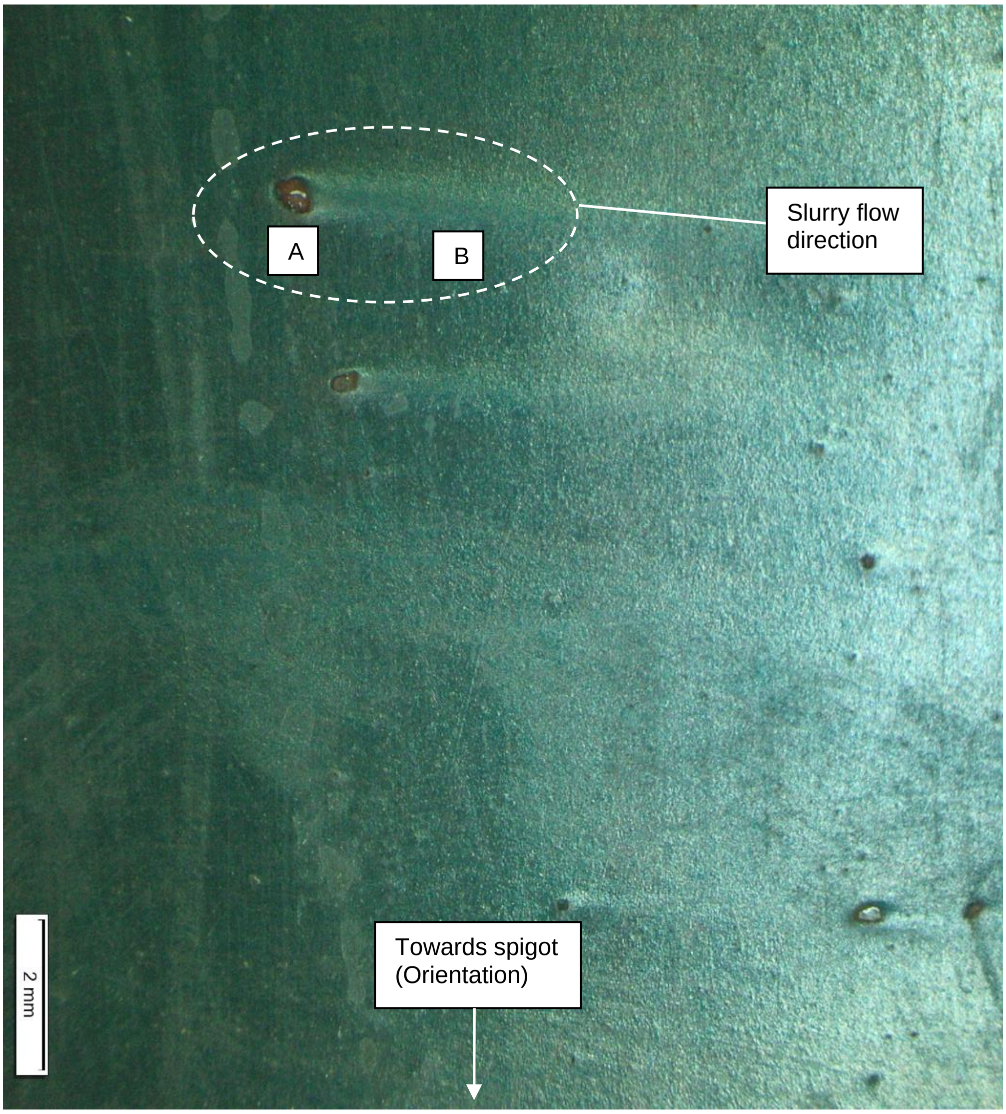

Figure 4.20: Image taken using an Olympus SZX7 stereomicroscope of smaller wear scars on NR wear lining of the lower cone, with the respective orientation relative to the spigot and the slurry flow direction indicated by the arrow. A wear scar is highlighted by the ellipsoid.

Figure 4.21(a) shows an enlarged micrograph of the wear scar located at position A in Figure 4.20. Using stereo-microscopy, it was observed that material degradation occurred at the interface of A and B in Figure 4.21. Figure 4.22 illustrates a schematic representation of the devulcanization that was observed at the interface of A and B in Figure 4.21. The degraded interface contained a sticky yellow residue, shown in Figure 4.21(b) B. This observation relates to the findings that chemical attack can be accelerated by the presence of cracking and increased stress caused by impinging particles on the surface layer of a polymer, as illustrated in Figure 2.33 (Stachowiak and Batchelor, 2014).

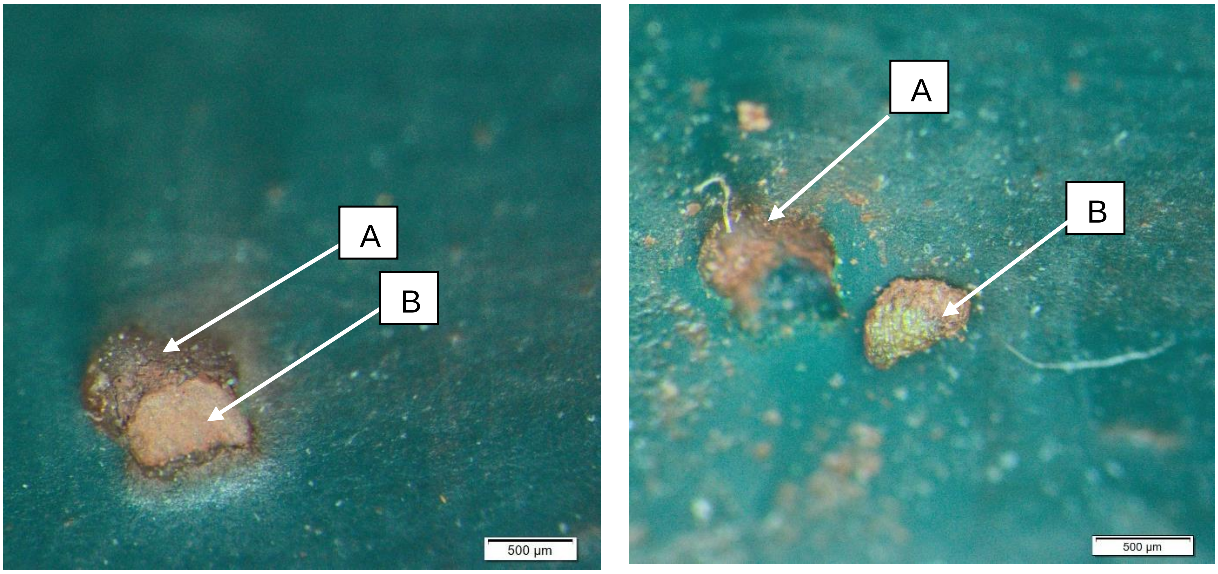

a) *b)*

Figure 4.21: Micrographs taken using an Olympus SZX7 stereomicroscope of a wear site that showed evidence of devulcanization occurring within a localized area.

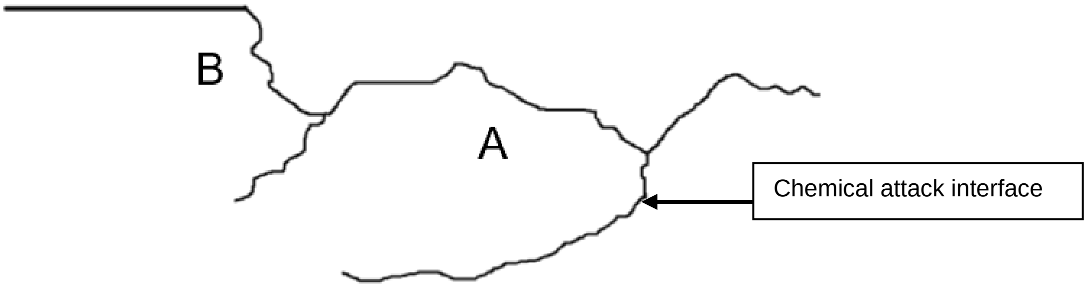

Figure 4.22: Side-view illustration of stereomicroscope observations of Figure 4.21.

4.3.3 Phase C3

Figure 4.23 shows the test rig after modifications were made to add automatic samplers at the underflow and overflow. The position of the hydrocyclone had to be lifted considerably to install the timed vezin and boom stacker. It was important to obtain the correct height between the cutter boom stacker and the underflow to get a complete crosscut of the spraying discharge during sampling.

Figure 4.23: Photograph of test rig after installation of automatic samplers.

4.3.4 Phase C4

The efficiency test results for the new and worn spigots are summarized in Table 4.3; corrected partition curves for the worn spigot are displayed in Figure 4.24. Three combined samples were taken at both the under- and overflows (three U/F and three O/F samples) and the respective plots are shown on the partition curve for each test. The corrected partition curves of the new spigot test is displayed in Figure 4.25 (only two curves are shown due to inconclusive results obtained for the third sample (jagged curve shown in Figure F.11 in Appendix F)).

The reason why the fish-hook effect occurred in both tests shown in Figure 4.24 and Figure 4.25 can be related to the feed PSD. The feed included both very fine and coarse silica and had a very wide PSD, as shown Figure 3.18. As mentioned in Section 2.3.5, the fish-hook phenomenon occurs in applications where both larger particles and ultra-fine (−10 µm) particles are present (Schubert, 2010).

The imperfection (IMP) values of the corrected partition curves for both tests are listed in Table 4.3. The measured RD values, calculated flowrates, mass and water split, and fish-hook height and width are also given.

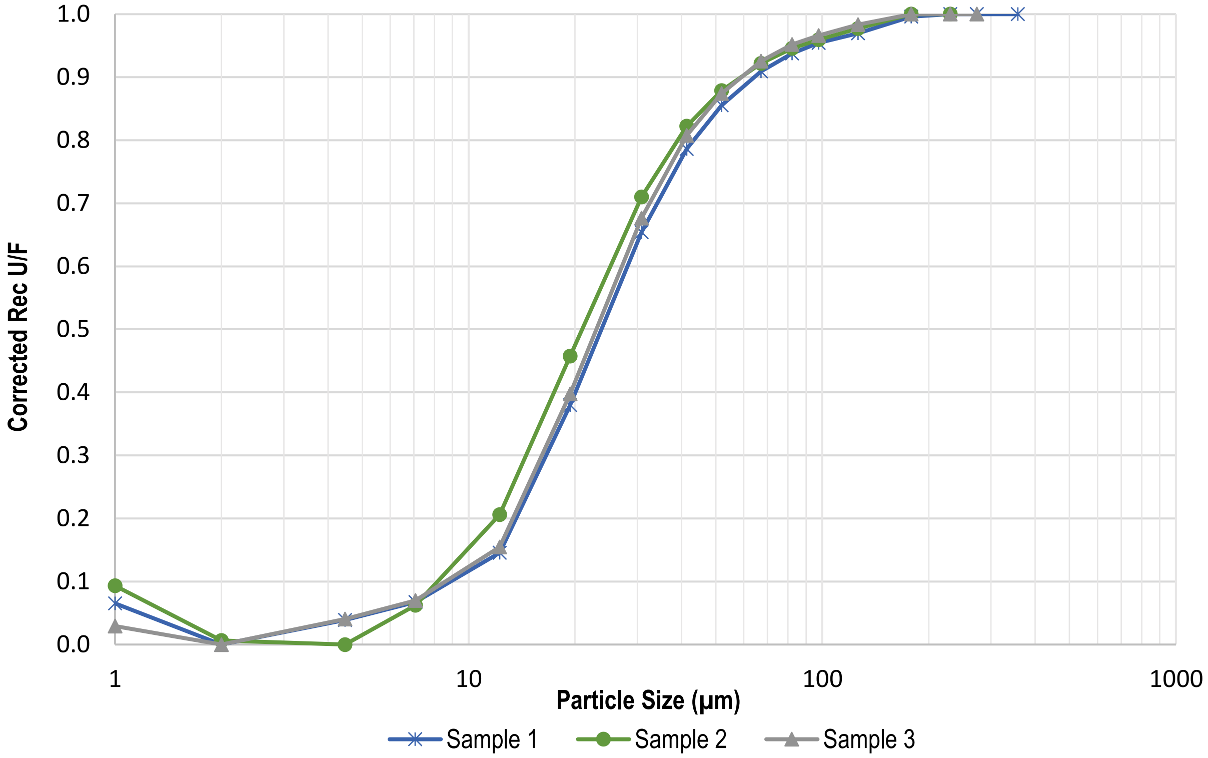

Figure 4.24: Corrected partition curve of worn spigot test according to the results of Samples 1, 2 and 3.

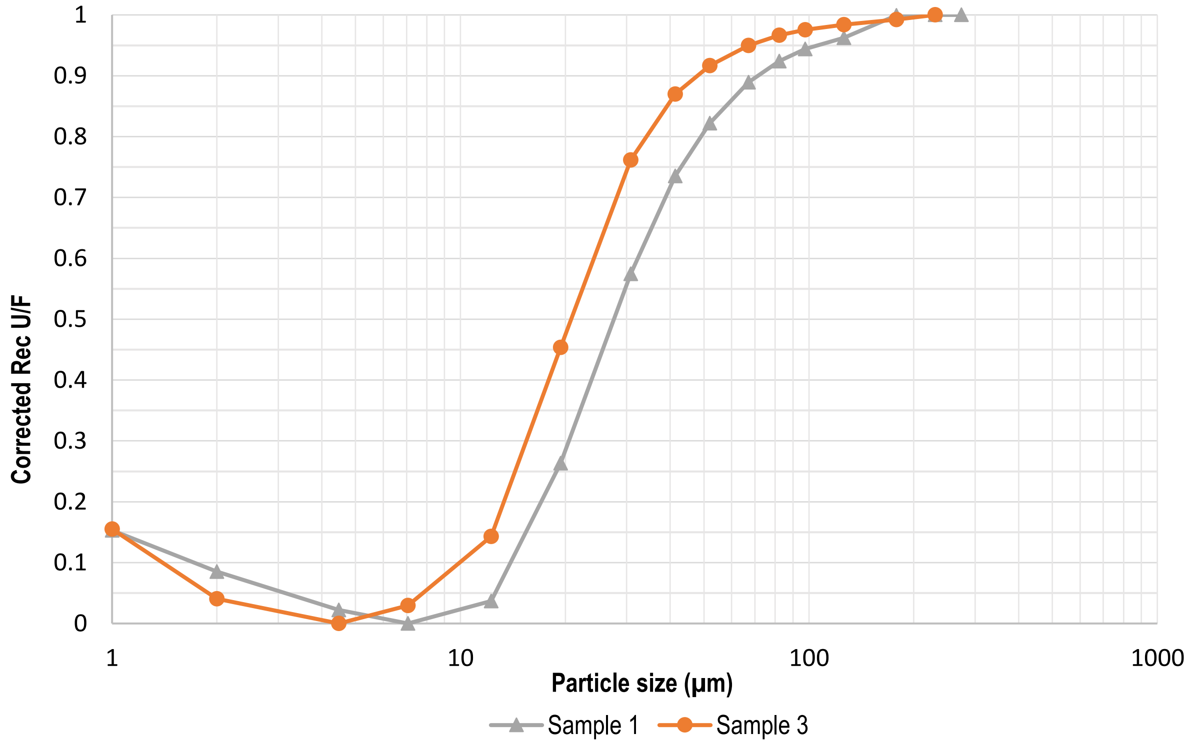

Figure 4.25: Corrected partition curve for the new spigot test for Samples 1 and 3. (Sample 2 omitted due to data point outliers).

Table 4.3: Summary of results of efficiency test for the new and worn spigots.

Parameter	Worn spigot (122 days)	New spigot (50 mm)
Feed RD	1.138	1.137
O/F RD	1.034	1.053
U/F RD	1.183	1.359
Flowrate O/F	38.8 t/h	42.6 t/h
Flowrate U/F	17.1 t/h	12.4 t/h
Feed pressure	70 kPa (± 4 kPa fluctuation)	70 kPa (± 4 kPa fluctuation)
Solids mass split to U/F	67.36%	60%
Water split to U/F	25.97%	15%
Cut size (d50c)	23.1 µm	24.6 µm
Average IMP (corrected)	0.48	0.39
δ (hook height)	0.03–0.09	0.15
$C+D$ (hook width)	2 µm	4.5–7 µm

Table 4.3 shows that the cut size for the worn spigot was slightly lower than that of the new spigot. This could be related to the fact that the worn spigot had a diameter of 55 mm while the new spigot had a diameter of 50 mm. According to the Plitt model, a larger spigot diameter will lead to a smaller cut size (Gupta and Yan, 2016).

The imperfection of the new spigot was lower than that of the worn spigot. This showed that the new spigot achieved a sharper cut (less misplaced material between partition factors 0.75 and 0.25) and, based on this metric, operated at a higher efficiency. Another important observation was the large difference between the relative densities produced at the underflow: the new spigot discharged at a much higher RD (1.359 compared with 1.183). This relates to the finding in the literature that states that spigot wear typically leads to lower underflow RDs (Olson and Turner, 2002). The worn spigot had a 13.7% larger inner volume, and therefore a larger water and solids split (to underflow) was observed. Lower efficiency (imperfection) values in a hydrocyclone could lead to lower mineral recoveries in a circuit (such as misplacement of valuable mineral to the overflow or underflow). The offset in RD could also have a negative impact, as in the case of a densification cyclones where a high underflow RD is desired. Monitoring of wear in hydrocyclones is therefore of critical importance in certain applications.

Another important observation is that the fish-hook effect was observed to be greater for the new spigot, based on the hook height δ and width C. Therefore, the amount of misplaced ultrafine material was greater for the new spigot; the worn spigot had greater efficiency in separating the ultrafine particles (−10 µm). This showed that a larger mass pull of water to the underflow will not always lead to greater misplacement of ultrafines (−10 µm), as suggested by the Kellsal method (Flintoff and Kuehl II, 2011). It is not known why the new spigot showed a greater fishook effect, but this could be related to the presence of a slight step between the spigot inlet and the cone outlet of the hydrocyclone, so the diameter of the spigot inlet could possibly have been slightly larger than the cone outlet, leading to turbulence.

Wear in the spigot, shown in Figure 4.12 was very homogenous (even), perhaps due to the feed recirculation, and did not resemble some of the uneven wear patterns observed in the industry (refer to Figure 4.4 to Figure 4.6). Wear observed in industry is also not only limited to the spigot, but also includes other parts of the hydrocyclone. This could likely lead to worse separation efficiency and misplacement, as suggested by Olson and Turner (2002).

4.4 Phase D: Wear Analysis of VV165 Hydrocyclone

4.4.1 Phase D1

The inner spigot volumes measured for a new VV165 spigot and individual spigots analysed after two weeks, eight weeks and three months in operation are listed in Table 4.4. A larger inner volume relative to a new spigot is related to the amount of spigot material lost due to wear. (Note that a larger outlet radius does not directly correlate to a larger inner spigot volume.)

Table 4.4: Inner spigot volume as a function of time in operation for commercial VV165 hydrocyclone.

Operating time	Colour (Figure 4.26)	Inner spigot volume (mm^3)	Radius at outlet (mm)	Difference relative to new spigot (%)
New	red	197 926	15.58	0
2 weeks*	blue	199 771	16.20	0.009
8 weeks	yellow	198 422	16.01	0.003
3 months	green	199 076	16.24	0.006

**Note: four different spigots from the same application that had been in use for different times were analysed.*

The spigot inner volumes for the different operating times are superimposed in Figure 4.26. The data of Table 4.4 and Figure 4.26 indicate that there was no significant percentage difference in void volume (differences observed are due to the fact that different hydrocyclones were scanned and therefore slight manufacturing deviations between the spigots are present). Therefore, it was concluded that no significant wear occurred after three months. The reason for this is that the magnetite feed material was less than 45 µm in size and these particles were not large enough to cause significant wear within the observed time period. These results correlate with findings that there is a critical velocity at which wear will occur for a specific particle size of feed material (Iwai and Nambu, 1997). If the average particle velocity is constant, a critical diameter will be required to cause wear. It can therefore be stated that the magnetite medium at a size of −45 µm is below the critical diameter required to cause wear within three months at the particle velocity applied (particle velocity relates to the feed pressure and flowrate of the feed into the hydrocyclone (Zhang *et al.*, 2017)).

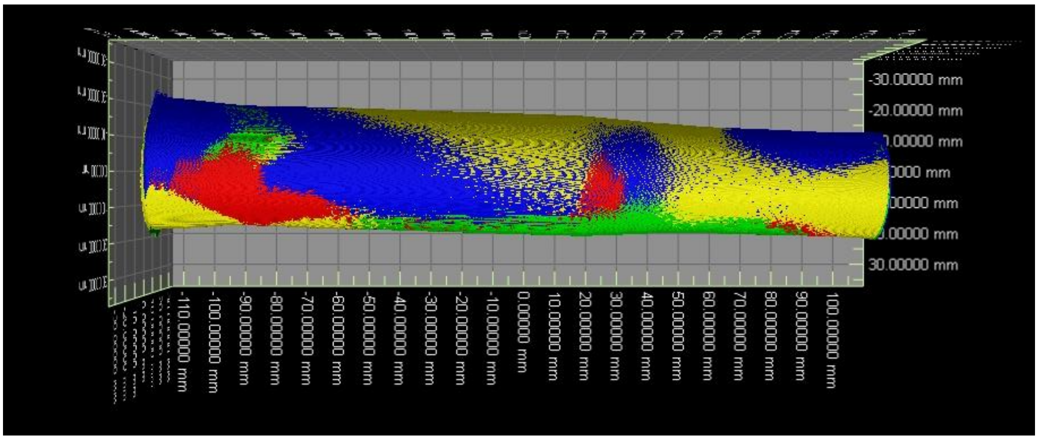

Figure 4.26: Inner volumes of VV165 spigots after different operating times superimposed on each other. Red = new, blue = 2 weeks, yellow = 8 weeks, green = 3 months in operation.

In commercial application, it was observed that the losses in efficiency were not caused by wear, but by occasional operational problems, such as blocking of the feed inlet by oversized material. Excessive gravity feed pressures also led to mechanical failure of the hydrocyclone and some spigots were missing. Images of inlet blocking and spigot blocking by oversized material are displayed in Figure 4.27.

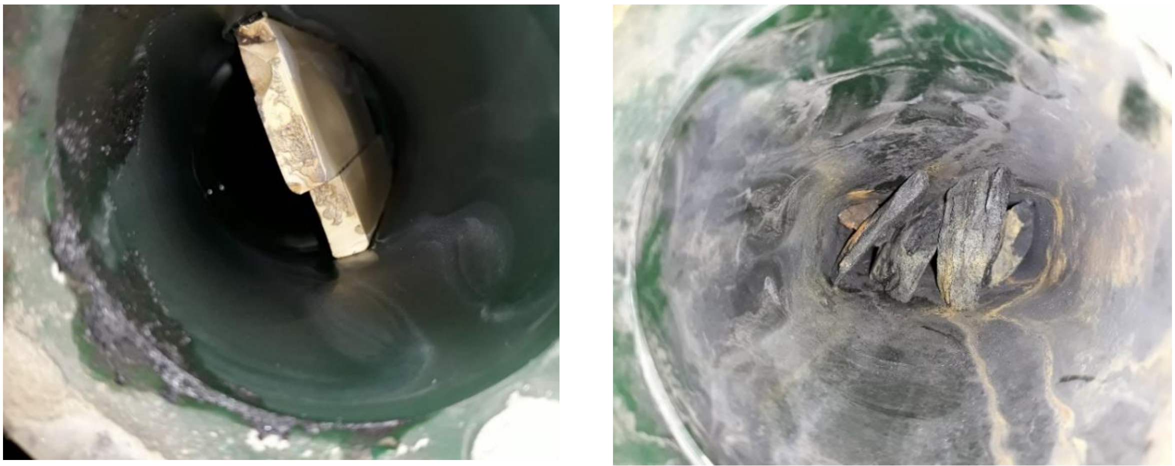

a) *b)*

Figure 4.27: Photographs of (a) blocked spigot on a VV350 hydrocyclone in a coal application and (b) blocked inlet of VV165 magnetite densification cyclone.

CHAPTER 5: CONCLUSIONS AND RECOMMENDATIONS

5.1 Conclusions

The highest amount of wear in a hydrocyclone was observed to occur at the spigot; the second-highest wear was observed in the lower conical section. In some cases, the vortex finder also showed significant wear. The driving force for the higher wear rate in lower regions of a hydrocyclone could be related to the increased solids concentration and coarser PSD in this region. It is suggested that the increased wear rate at the vortex finder is due to the higher axial and tangential flow velocities of the particles within this region (Phase B1).

It was found that micro-CT technology (using a Nikon XT H 225 ST instrument) can be used to quantify and investigate hydrocyclone wear and is a useful method to evaluate sub-surface defects in polymer component manufacturing (Phase B2).

The change in spigot volume of a HC250-15-1/A-B/50 hydrocyclone in a recirculating rig was measured over 122 days using micro-CT: a 13.76% loss in spigot volume was measured due to wear. This wear rate observed over the 122-day period was relatively low compared with that of highly abrasive applications, due to particle smoothening and a reduction in particle size with material recirculation. It was found that particle shape and size have a very significant influence on the wear rate: a decrease in particle size and angularity reduced the wear rate. It was observed that porosity, attributed to compression-moulding manufacturing defects, caused accelerated wear within a localized area of the cone NR lining of the HC250-15-1/A-B/50 hydrocyclone. The rubber lining showed signs of chemical attack at smaller wear scar locations, which can be related to the fact the impinging particles can lead to cracking and stress that create preferential sites for chemical attack and material degradation (Stachowiak and Batchelor, 2014) (Phase C2).

Results of the efficiency test showed that the worn spigot gave lower separation efficiency based on the IMP value: worn spigot 0.48; new spigot 0.39. The cut size remained almost unchanged: 23.1 µm for the worn spigot and 24.6 µm for the new component. Spigot wear did, however, lead to a significant change in the underflow RD: the worn spigot gave an U/F RD of 1.183, whilst the new spigot gave 1.359. This result confirmed previous findings that spigot wear leads to lower underflow RDs (Olson and Turner, 2002). Although the worn spigot recovered a larger amount of water to the underflow, the fines misplacement and fish-hook size were greater for the new spigot. It is suggested that an offset in underflow RD and reduced efficiency due to wear could lead to process control offsets and lower recovery (Phase C4).

The wear in a 165 mm Dc Multotec VV165 densification cyclone in commercial operation was investigated using micro-CT technology. No detectable wear occurred within a three-month operating period. The particle size of the magnetite medium (−45 µm) was below the critical diameter required to cause wear at the particle velocity in operation (Iwai and Nambu, 1997). It was also observed that the losses in efficiency were not related to wear, but to operational problems, such as excessive feed pressures and inlet blocking (Phase D1).

5.2 Recommendations

Based on the material test results (Phases A1 and A2), it is suggested to test different polymers (NR and PU) using an in-situ hydrocyclone wear test or suitable laboratory wear test method. The tests should evaluate the influence of particle and feed properties on the wear rate of the selected materials. The results can be used to optimize material selection for specific slurry wear applications.

To avoid premature wear in localized areas, it is suggested to occasionally sample and monitor the amount of internal porosity after casting and compression moulding, using a suitable non-destructive test method.

The impact of wear in the hydrocyclone cone and vortex finder (with new and worn spigots) on hydrocyclone efficiency should be investigated.

REFERENCES

Arnold, J. C. and Hutchings, I. M. (1991) ‘The erosive wear of elastomers’, *Journal of Natural Rubber Research*, 6(4), pp. 241–256.

Arnold, J. C. and Hutchings, I. M. (1993) ‘Erosive wear of rubber by solid particles at normal incidence’, *Wear*, 161(1–2), pp. 213–221. doi: 10.1016/0043-1648(93)90472-X.

ASTM International (2015a) ‘D5963 - 04 Standard Test Method for Rubber Property—Abrasion Resistance (Rotary Drum Abrader)’, *ASTM*, 1(Reapproved), pp. 1–9. doi: 10.1520/D5963-04R15.2.

ASTM International (2015b) ‘G190 -15 Standard Guide for Developing and Selecting Wear Tests’, *ASTM*, 1, pp. 1–5. doi: 10.1520/G0190-06.2.

ASTM International (2015c) *G75-15 Standard Test Method for Determination of Slurry Abrasivity (Miller Number) and Slurry Abrasion Response of Materials (SAR Number)*, *ASTM*. doi: 10.1520/G0075-07.2.

ASTM International (2016a) ‘G105 - 16 Standard Test Method for Conducting Wet Sand / Rubber Wheel Abrasion Tests’, *ASTM*, 1, pp. 1–9. doi: 10.1520/G0105-02R07.2.

ASTM International (2016b) ‘G65 - 16 Standard Test Method for Measuring Abrasion Using the Dry Sand / Rubber Wheel’, *ASTM*, 1, pp. 1–12. doi: 10.1520/G0065-04R10.2.

Azimian, M. and Bart, H. J. (2016) ‘Numerical analysis of hydroabrasion in a hydrocyclone’, *Petroleum Science*, 13(2), pp. 304–319. doi: 10.1007/s12182-016-0084-7.

Budinski, K. G. (2007a) ‘Alternatives to Testing: Modeling and Simulation’, in *Guide to Friction, Wear, and Erosion Testing*. West Conshohocken: ASTM International, p. 19,20. doi: 10.1016/0164-1212(90)90093-2.

Budinski, K. G. (2007b) ‘Erosion Testing’, in *Guide to Friction, Wear, and Erosion Testing*. West Conshohocken: ASTM International, pp. 86–93.

Budinski, K. G. (2007c) ‘Plastic/Elastomer Wear’, in *Guide to Friction, Wear, and Erosion Testing*. ASTM International, p. 11.

Buschow, K. H. ., Cahn, R. ., Flemings, M., Ilschner, B., Kramer, E. and Mahajan, S. (2001) ‘NDT techniques: computed tomography’, in *Encyclopedia of Materials: Science and Technology*. Volume 2. Oxford: Elsevier, pp. 6006–6009. doi: 10.1016/b0-08-043152-6/01055-x.

Chang, Y., Ilea, C., Aasen, L. and Hoffmann, A. (2011) ‘Particle flow in a hydrocyclone investigated by positron emission particle tracking’, *Chemical Engineering Science*, 66(18), pp. 4203–4211. doi: 10.1016/j.ces.2011.06.001.

Ciesielski, A. (1999) *An Introduction to Rubber Technology*. 1st edn. Shawbury: Rapra Technology LTD.

Clavier, R. (2008) ‘Nuclear Magnetic Resonance’, in *Characterization and Analysis of Polymers*. 1st edn. Hoboken, p. 171.

Clemitson, I. R. (2008) *Castable Polyurethane Elastomers*. 1st edn. Boca Raton: CRC Press.

Cortie, M. B., McEwan, J. J. and Enright, D. P. (1996) ‘Materials selection in the mining industry: Old issues and new challenges’, *SAIMM*.

Davailles, A., Climent, E., Bourgeois, F. and Majumder, A. K. (2012) ‘Analysis of swirling flow in hydrocyclones operating under dense regime’, *Minerals Engineering*, 31, pp. 32–41. doi: 10.1016/j.mineng.2012.01.012.

Desale, G. R., Gandhi, B. K. and Jain, S. C. (2006) ‘Effect of erodent properties on erosion wear of ductile type materialsfect of erodent properties on erosion wear of ductile type materials’, *Wear*, 261(7–8), pp. 914–921. doi: 10.1016/j.wear.2006.01.035.

Dueck, J., Farghaly, M. and Neesse, T. (2014) ‘The theoretical partition curve of the hydrocyclone’, *Minerals Engineering*, 62, pp. 25–30. doi: 10.1016/j.mineng.2013.10.004.

Dunne, R., Honaker, R. and Popplewell, G. (2019) ‘Dense medium seperation’, in *SME Mineral Processing & Extractive Metallurgy Handbook*. Colorado: SME, pp. 827–828.

Flintoff, B. and Kuehl II, R. (2011) ‘Classification by screens and cyclones’, in *SME Mining Engineering Handbook*. 3rd edn. Englewood: SME, p. 26.

Frosell, T., Fripp, M. and Gutmark, E. (2015) ‘Investigation of slurry concentration effects on solid particle erosion rate for an impinging jet’, *Wear*, 342–343, pp. 33–43. doi: 10.1016/j.wear.2015.08.003.

Ghodrat, M., Kuang, S. B., Yu, A. B., Vince, A., Barnett, G. D. and Barnett, P. J. (2013) ‘Computational study of the multiphase flow and performance of hydrocyclones: effects of cyclone size and spigot diameter’, *Industrial & Engineering Chemistry Research*, 52(45), pp. 16019–16031. doi: 10.1021/ie402267b.

Giltrow, J. P. (1970) ‘a Relationship between abrasive wear and the cohesive energy of materials’, *Wear*, 15(1), pp. 71–78.

Gupta, A. and Yan, D. S. (2016) *Mineral processing design and operations: an introduction*. 2nd edn. Amsterdam: Elsevier.

Gupta, R., Singh, S. N. and Sehadri, V. (1995) ‘Prediction of uneven wear in a slurry pipeline on the basis of measurements in a pot tester’, *Wear*, 184(2), pp. 169–178. doi: 10.1016/0043-1648(94)06566-7.

de Haan, A. B. and Bosch, H. (2013) *Industrial Separation Processes*. Berlin, Boston: De Gruyter. doi: 10.1515/9783110306729.

Hoffman, J. W. and Beer, F. C. D. E. (2012) ‘Characteristics of the micro-focus X-ray tomography facility (MIXRAD) at Necsa in South Africa’, in *18th World Conference on Nondestructive Testing*. Ndt, pp. 16–20.

Holmberg, K., Kivikytö-Reponen, P., Härkisaari, P., Valtonen, K. and Erdemir, A. (2017) ‘Global energy consumption due to friction and wear in the mining industry’, *Tribology International*. Elsevier, 115, pp. 116–139. doi: 10.1016/J.TRIBOINT.2017.05.010.

Iwai, Y. and Nambu, K. (1997) ‘Slurry wear properties of pump lining materials’, *Wear*, 210(1–2), pp. 211–219. doi: 10.1016/S0043-1648(97)00055-0.

Jacobs, B. E. A. (1991) *Design of Slurry Transport Systems*. Barking: CRC Press.

Jacobs, J. and Testa, M. S. (2014) ‘Causes, assessment, prediction, prevention, and remediation’, in Jacobs, J. and Testa, M. S. (eds) *Acid Mine Drainage, Rock Drainage, and Acid Sulfate Soils Remediation*. 1st edn. New Jersey: John Wiley & Sons, Inc., pp. 3–8.

Jafari, A., Dehghani, K., Bahaaddini, K. and Abbasi Hataie, R. (2018) ‘Experimental comparison of abrasive and erosive wear characteristics of four wear-resistant steels’, *Wear*. Elsevier B.V., 416–417(September), pp. 14–26. doi: 10.1016/j.wear.2018.09.010.

Jones, L. C. (2011) ‘Low angle scouring erosion behaviour of elastomeric materials’, *Wear*. Elsevier, 271(9–10), pp. 1411–1417. doi: 10.1016/J.WEAR.2010.12.057.

Lin, C. L., Miller, J. D. and Lin, C. L. (2009) ‘High resolution x-ray micro-CT (HRXMT)—advances in 3D particle characterization for mineral processing operations’, in *Recent Advances in Mineral Processing Plant Design*. 1st edn. Littleton: SME, pp. 48–59.

Lindroos, V., Markku, T., Ari, L. and Teruaki, M. (2010) ‘Automated surface inspection’, in *Handbook of Silicon Based MEMS Materials and Technologies*. Oxford: William Andrew Publishing, pp. 209–220. doi: 10.2307/j.ctt1d8hbgx.17.

Llewellyn, R. J., Yick, S. K. and Dolman, K. F. (2004) ‘Scouring erosion resistance of metallic materials used in slurry pump service', *Wear*, 256(6), pp. 592–599. doi: 10.1016/j.wear.2003.10.002.

MacDonald, D., Bowden, A. and Kurtz, S. M. (2009) 'MicroCT Analysis of Wear and Damage in UHMWPE', in *UHMWPE Biomaterials Handbook*. Elsevier, pp. 511–518. doi: 10.1016/B978-0-12-374721-1.00034-1.

Maurice, N. and Kenneth, C. (2003) 'Principles of Mineral Processing', *SME*, p. 573. doi: ISBN 0-87335-167-3.

Miller, J. and Schmidt, F. (eds) (1987) *Slurry Erosion: Uses, Applications, and Test Methods*. West Conshohocken: ASTM International. doi: 10.1520/STP946-EB.

Moore, M. A. (1974) 'The relationship between the abrasive wear resistance, hardness and microstructure of ferritic materials', *Wear*, 28(1), pp. 59–68. doi: 10.1016/0043-1648(74)90101-X.

Nageswararao, K. (2016) 'Modelling of hydrocyclone classifiers: A critique of "bypass" and corrected efficiency', *Powder Technology*, 297, pp. 106–114. doi: 10.1016/j.powtec.2016.04.016.

Olson, T. J. and Turner, P. A. (2002) 'Hydrocyclone selection for plant design', in *Mineral Processing Plant Design, Practice and Control Proceedings*. Littleton: SME, pp. 880–893. Available at: http://www.knovel.com/web/portal/browse/display?_EXT_KNOVEL_DISPLAY_bookid=3931&VerticalID=0.

Raine, D. (2017) *Newtonian Mechanics - A Modelling Approach*. 1st edn. Boston: Mercury learning and information.

Ramirez, J. (2012) *SURFACE ROUGHNESS STATISTICAL ANALYSIS USING 3D PROFILOMETRY*. California. Available at: http://nanovea.com/App-Notes/roughness-statistical-analysis.pdf (Accessed: 6 September 2017).

Reyence (2017) *Area Roughness Parameters*. Available at: http://www.keyence.com/ss/products/microscope/roughness/surface/parameters.jsp (Accessed: 6 September 2017).

Richardson, J. F. and Harker, J. H. (2002) 'Chemical engineering-Volume 2: Particle Technology and Separation Processes', *Chemical Engineering Science*, 2, p. 1183. doi: 10.1016/0009-2509(60)80030-9.

Robinson, L. and Garcia, J. (2015) 'Drilling fluid processing', in *IADC Drilling Series - Drillers Knowledge Book - Creative Solutions for Today's Drilling Challenges*. 1st edn. Houston: International Association of Drilling Contractors (IADC), pp. 228–260.

Schubert, H. (2010) 'Which demands should and can meet a separation model for hydrocyclone classification ?', *International Journal of Mineral Processing*, 96, pp. 14–26. doi: 10.1016/j.minpro.2010.04.003.

Stachowiak, G. W. and Batchelor, A. W. (2014) *Engineering Tribology*. 4th edn. Trans Tech Publications Ltd. doi: 10.1016/C2011-0-07515-4.

Stanley, G. G. (1987) *The Extractive Metallurgy of Gold in South Africa, Volume 2*. Johannesburg: South African Institute of Mining and Metallurgy.

Thakur, P. (2017) 'Fluid flow in pipes and boreholes', *Advanced Reservoir and Production Engineering for Coal Bed Methane*, pp. 91–104. doi: 10.1016/b978-0-12-803095-0.00007-7.

Walker, C. I. and Hambe, M. (2014) 'Influence of particle shape on slurry wear of white iron', *Wear*. Elsevier, 332–333, pp. 1021–1027. doi: 10.1016/j.wear.2014.12.029.

Wang, B. and Yu, A. . (2010) 'Computational investigation of the mechanisms of particle separation and "' Fish-Hook '" phenomenon in hydrocyclones', *AIChE*, 56(7), pp. 1703–1715. doi: 10.1002/aic.

White, F. M. (2009) *Fluid Mechanics*. New York: MCGraw Hill. doi: 10.1111/j.1549-8719.2009.00016.x.Mechanobiology.

Wills, B. and Napier-Munn, T. (2006) *Wills' Mineral Processing Technology*. 7th edn. Oxford: Elsevier.

Xie, Y., Jiang, J. (Jimmy) and Islam, M. A. (2019) 'Elastomers and plastics for resisting erosion attack of abrasive/erosive slurries', *Wear*. Elsevier B.V., 426–427(August 2018), pp. 612–619. doi: 10.1016/j.wear.2019.01.123.

Xie, Y., Jiang, J. (Jimmy), Tufa, K. Y. and Yick, S. (2015) 'Wear resistance of materials used for slurry transport', *Wear*, 332–333, pp. 1104–1110. doi: 10.1016/j.wear.2015.01.005.

Xu, P., Wu, Z., Mujumdar, A. S. and Yu, B. (2009) 'Innovative hydrocyclone inlet designs to reduce erosion-induced wear in mineral dewatering processes', *Drying Technology*, 27(2), pp. 201–211. doi: 10.1080/07373930802603433.

Zhang, C., Cui, B., Wei, D., Zhao, Q., Luo, N. and Feng, Y. (2017) 'Predicting the optimum range of feed flow rate in a hydrocyclone using the method combined flow pattern and equation model', 319, pp. 279–288.

Zhang, C., Wei, D., Cui, B., Li, T. and Luo, N. (2017) 'Effects of curvature radius on separation behaviors of the hydrocyclone with a tangent-circle inlet', *Powder Technology*, 305, pp. 156–165. doi: 10.1016/j.powtec.2016.10.002.

Zhang, H., Zhou, L. Y. and Zhang, Z. (2015) 'Transparent wear-resistant multifunctional polymeric nanocoatings', in *Multifunctionality of Polymer Composites: Challenges and New Solutions*. Elsevier Inc., pp. 573–587. doi: 10.1016/B978-0-323-26434-1.00018-0.

Zhang, S. W., Deguo, W. and Weihua, Y. (1995) 'Investigation of abrasive erosion of polymers', *Journal of Materials Science*, 30(18), pp. 4561–4566. doi: 10.1007/BF01153063.

Zhang, Y., Pu, C., Feihua, J. and Kejun, D. (2017) 'Understanding the separation of particles in a hydrocyclone by force analysis', *Powder Technology*. Elsevier, 322, pp. 471–489. doi: 10.1016/J.POWTEC.2017.09.031.

Declaration on plagiarism

UNIVERSITY OF PRETORIA

Faculty of Engineering, the Built Environment and Information Technology Department of Materials Science and Metallurgical Engineering

The University places great emphasis upon integrity and ethical conduct in the preparation of all written work submitted for academic evaluation.

While academic staff teach you about systems of referring and how to avoid plagiarism, you too have a responsibility in this regard. If you are at any stage uncertain as to what is required, you should speak to your lecturer before any written work is submitted.

You are guilty of plagiarism if you copy something from a book, article or website without acknowledging the source and pass it off as your own. In effect you are stealing something that belongs to someone else. This is not only the case when you copy work word-by-word (verbatim), but also when you submit someone else's work in a slightly altered form (paraphrase) or use a line of argument without acknowledging it. You are not allowed to use another student's past written work. You are also not allowed to let anybody copy your work with the intention of passing it off as his/her work.

Students who commit plagiarism will lose all credits obtained in the plagiarised work. The matter may also be referred to the Disciplinary Committee (Students) for a ruling. Plagiarism is regarded as a serious contravention of the University's rules and can lead to expulsion from the University.

The declaration which follows must be appended to all written work submitted for Literature Survey NSC412 and NSC421. No written work will be accepted unless the declaration has been completed and attached.

I (full names)	Simeon Combrink
Student number	12214282
Topic of work	Hydrocyclones

Declaration

1. I understand what plagiarism is and am aware of the University's policy in this regard.
2. I declare that this report is my own original work. Where other people's work has been used (from a printed source, internet or any other source), this has been properly acknowledged and referenced in accordance with departmental requirements.
3. I have not used another student's past written work to hand in as my own.
4. I have not allowed, and will not allow, anyone to copy my work with the intention of passing it off as his or her own work.

Signature _____________S.C.

APPENDIX A: ASTM TEST PROCEDURES

A.1 ASTM D5963 Test Procedure

10.1 The test shall be carried out at 23 6 5°C (73 6 9°F) and no sooner than 16 h after vulcanization or forming of the test compounds.

10.2 The density of the rubbers to be tested shall be determined using a hydrostatic method (see Test Methods D297 or ISO 2781). 10.3 Method A—Test Run:

10.3.1 Method A is run with a non-rotating test piece, using Standard Rubber #1 as reference.

10.3.2 Prior to each test, any debris left on the abrasive sheet from a previous abrasion test shall be removed by vigorous brushing, blowing, or suction. If necessary, the sheet may be cleaned by running a blank test with the Standard Rubber in case the sheet has been smeared by a test piece from the previous test.

10.3.3 First, at least three test runs shall be made with the Standard Rubber, followed by a maximum of ten runs (see Note 4 with one or more rubbers to be tested (test series). This shall be followed by at least another three runs with the Standard Rubber.

NOTE 4—Do not split tests of one test rubber. Run nine tests, and so forth, if that completes the tests for a test rubber.

10.3.4 When more than one rubber is to be tested, the test runs for each rubber shall be carried out consecutively. Only one test run per test rubber piece is permitted.

10.3.5 At least three test pieces and, for referee purposes, ten test pieces shall be run. The results shall be expressed as the mean value.

10.3.6 The test pieces shall be weighed to the nearest 1 mg and firmly fixed into the holder so that it protrudes 2.0 6 0.2 mm (0.08 6 0.008 in.) from the opening of the holder. Turn the vacuum on if it is provided. The swivel arm is moved into starting position and the automatic test run is started (see Note

5). NOTE 5—A preparatory run to hollow-grind the test piece is not necessary.

10.3.7 There shall be no vibration in the test piece holder during the run. After completing an abrasion path of 40 m

(131.2 ft), the test piece shall automatically disengage from the abrasive sheet.

10.3.8 The test piece is reweighed to the nearest 1 mg. Test pieces that have heated up during testing shall be conditioned to room temperature prior to weighing. Any loose material shall be removed from the test piece prior to weighing.

10.3.9 If there is a considerable loss in mass (400 mg or more per 40 m (131.2 ft) abrasion path), the test may be run by stopping the abrasion drum approximately halfway through the test, readjusting the test piece to protrude 2.0 6 0.2 mm (0.08 6 0.008 in.) from the opening of the holder and then complete the run. Care shall be taken that the test piece does not abrade

to a thickness of less than 5 mm (0.2 in.).

10.3.10 If very high mass losses are encountered (600 mg or more per 40 m (131.2 ft) abrasion path), it may be necessary to terminate the test after an abrasion path of 20 m (65.6 ft). This shall be noted in the test report and the volume loss reported for an abrasion distance of 40 m (131.2 ft) by multiplying the value by two.

10.4 Method B—Test Run:

10.4.1 Method B is run with a rotating test piece. This applies to the test rubber as well as the Standard Rubber. Standard Rubber #1 is used as reference.

10.4.2 All other test conditions are the same as described in

10.5 Method C—Test Run:

10.5.1 Method C is run with a non-rotating test piece. This applies to the test rubber as well as the Standard Rubber. Standard Rubber #2 is used as reference.

10.5.2 All other test conditions are the same as described in

10.3.

10.6 Method D—Test Run:

10.6.1 Method D is run with a rotating test piece. This applies to the test rubber as well as the Standard Rubber. Standard Rubber #2 is used as reference.

10.6.2 All other test conditions are the same as described in 10.3.

A.2 ASTM G76 Test Procedure

11.1 Establish and measure the particle velocity and particle flow specified. Adjust equipment controls to obtain proper velocity and flow conditions before inserting test specimens. Particle flowrate values are determined by collecting and subsequently weighing the abrasive exiting from the nozzle for a measured time period.

11.2 Prepare the specimen surface if required to achieve uniformity and adequate finish. Grinding through a series of abrasive papers to 400 grit is usually adequate so long as all surface scale is removed. A surface roughness of 1 µm (40 µin.) rms or smaller is recommended. Clean the specimen surface carefully. Weigh on an analytical balance to 60.01 mg.

11.3 Mount the specimen in proper location and orientation in the apparatus. Subject the specimen to particle impingement for a selected time interval, measured to an accuracy of 5 s. Remove the specimen, clean carefully, reweigh and calculate the mass loss.

11.4 Repeat this process to determine at least four points for a total time of at least 10 min and plot those values as mass loss

versus elapsed time. Suitable times would be 2, 4, 8, and 16 min for a material such as Type 1020 steel. Steady state erosion should result after 1 to 2 min, depending on the material. Two examples of measured erosion versus time curves are shown in Fig. 5.

11.5 The steady state erosion rate (see Terminology G 40) is determined from the slope of the mass loss versus time plot. The average erosion value is calculated by dividing erosion rate ($mg \cdot min^{-1}$) by the abrasive flowrate ($g \cdot min^{-1}$) and then dividing by the specimen density ($g \cdot cm^{-3}$). Report the average erosion value as ($mm3 \cdot g^{-1}$).

11.6 Repeat 11.1 at the end of a series of tests

A.3 ASTM G65 Test Procedure

9.1 *Cleaning*—Immediately prior to weighing, clean the specimen with a solvent or cleaner and dry. Take care to remove all dirt or foreign matter or both from the specimen. Dry materials with open grains (some powder metals or ceramics) to remove all traces of the cleaning solvent, which may have been entrapped in the material. Steel specimens having residual magnetism should be demagnetized or not used.

9.2 Weigh the specimen to the nearest 0.001 g (0.0001 g for Procedure C).

9.3 Seat the specimen securely in the holder and add the proper weights to the lever arm to develop the proper force pressing the specimen against the wheel. This may be measured accurately by means of a spring scale which is hooked around the specimen and pulled back to lift the specimen away from the wheel. A wedge should be placed under the lever arm so that the specimen is held away from the wheel prior to start of test. (See Fig. 2.)

9.4 Set the revolution counter to the prescribed number of wheel revolutions.

9.5 *Sand Flow and Sand Curtain*—The rate of sand flow through the nozzles shall be between 300 g (0.66 lb)/min and 400 g (0.88 lb)/min. Do not start the wheel rotation until the proper uniform curtain of sand has been established (see Fig. 9 and Note 3).

9.5.1 The dwell time between tests shall be the time required for the temperature of the rubber wheel to return to room temperature. For Procedure B the dwell time shall be at least 30 min.

9.6 Start the wheel rotation and immediately lower the lever arm carefully to allow the specimen to contact the wheel.

9.7 When the test has run the desired number of wheel revolutions, lift the specimen away from the wheel and stop the sand flow and wheel rotation. The sand flowrate should be measured before and after a test, unless a consistent flowrate has been established.

9.8 Remove the specimen and reweigh to the nearest 0.001 g (0.0001 g for Procedure C).

9.8.1 *Wear Scar*—Observe the wear scar and compare it to the photographs of uniform and nonuniform wear scars in Fig.

11. A nonuniform pattern indicates improper alignment of the rubber rim to the test specimen or an unevenly worn rubber wheel. This condition may reduce the accuracy of the test.

9.9 *Preparation and Care of Rubber Wheels*—Dress the periphery of all new rubber wheels and make concentric to the bore of the steel disk upon which the rubber is mounted. The concentricity of the rim shall be within 0.05 mm (0.002 in.)

A.4 ASTM D412 Test Procedure

12.1 Determination of Tensile Stress, Tensile Strength and Yield Point—Place the dumbbell or straight specimen in the grips of the testing machine, using care to adjust the specimen symmetrically to distribute tension uniformly over the cross section. This avoids complications that prevent the maximum strength of the material from being evaluated. Unless otherwise specified, the rate of grip separation shall be 500 6 50 mm/min (20 ± 2 in./min). Start the machine and note the distance between the bench marks, taking care to avoid parallax. Record the force at the elongation(s) specified for the test and at the time of rupture. The elongation measurement is made preferably through the use of an extensometer, an autographic mechanism or a spark mechanism. At rupture, measure and record the elongation to the nearest 10 %. See Section 13 for calculations.

12.2 Determination of Tensile Set—Place the specimen in the grips of the testing machine described in 6.1 or the apparatus shown in Fig. 1, and adjust symmetrically so as to distribute the tension uniformly over the cross section. Separate the grips at a rate of speed as uniformly as possible, that requires 15 s to reach the specified elongation. Hold the specimen at the specified elongation for 10 min, release quickly without allowing it to snap back and allow the specimen to rest for 10 min. At the end of the 10 min rest period, measure the distance between the bench marks to the nearest 1 % of the original between bench mark distance. Use a stop watch for the timing operations. See Section 13 for calculations.

12.3 Determination of Set-After-Break—Ten minutes after a specimen is broken in a normal tensile strength test, carefully fit the two pieces together so that they are in good contact over the full area of the break. Measure the distance between the bench marks. See Section 13 for calculations.

A.5 ASTM D2240 Test Procedure

9.2.1 Care shall be exercised to minimize the exposure of the instrument to environmental conditions that are adverse to the performance of the instrument, or adversely affect test results.

9.2.2 Place the specimen on a flat, hard, horizontal surface. Hold the durometer in a vertical position with the indentor tip at a distance from any edge of the specimen as described in Section 6, unless it is known that identical results are obtained when measurements are made with the indentor at a lesser distance.

9.2.3 Apply the presser foot to the specimen, maintaining it in a vertical position keeping the presser foot parallel to the specimen, with a firm smooth downward action that will avoid shock, rolling of the presser foot over the specimen, or the application of lateral force. Apply sufficient pressure to assure firm contact between the presser foot and the specimen.

9.2.4 For any material covered in 1.1, after the presser foot is in contact with the specimen, the indicated reading shall be recorded within 1 6 0.1 s, or after any period of time agreed upon among laboratories or between supplier and user. If the durometer is equipped with a maximum indicator, the maximum indicated reading shall be recorded within 1 6 0.1 s of the cessation of initial indentor travel. The indicated hardness reading may change with time.

9.2.5 Make five determinations of hardness at different positions on the specimen at least 6.0 mm (0.24 in.) apart and calculate the arithmetic mean, or alternatively calculate the median. The means of calculating the determinations shall be reported according to 10.2.8.

9.3 It is acknowledged that durometer readings below 20 or above 90 are not considered reliable. It is suggested that readings in these ranges not be recorded.

9.4 Manual operation (handheld) of a durometer will cause variations in the results attained. Improved repeatability may be obtained by using a mass, securely affixed to the durometer and centered on the axis of the indentor. Recommended masses are 1 kg for Type A, B, E, and O durometers, 5 kg for Type C, D, and DO durometers, and 400 g for Type OO, OOO, and OOO-S durometers. The introduction of an additional mass on Type M durometers is not permitted. Further improvement may be achieved by the use of a durometer operating stand that controls the rate of descent of the durometer presser foot to the test specimen and incorporates the masses described above.

APPENDIX B: SURFACE ROUGHNESS MEASUREMENTS

Table B.1: Description and definition of parameters measured by a profilometer (Ramirez, 2012).

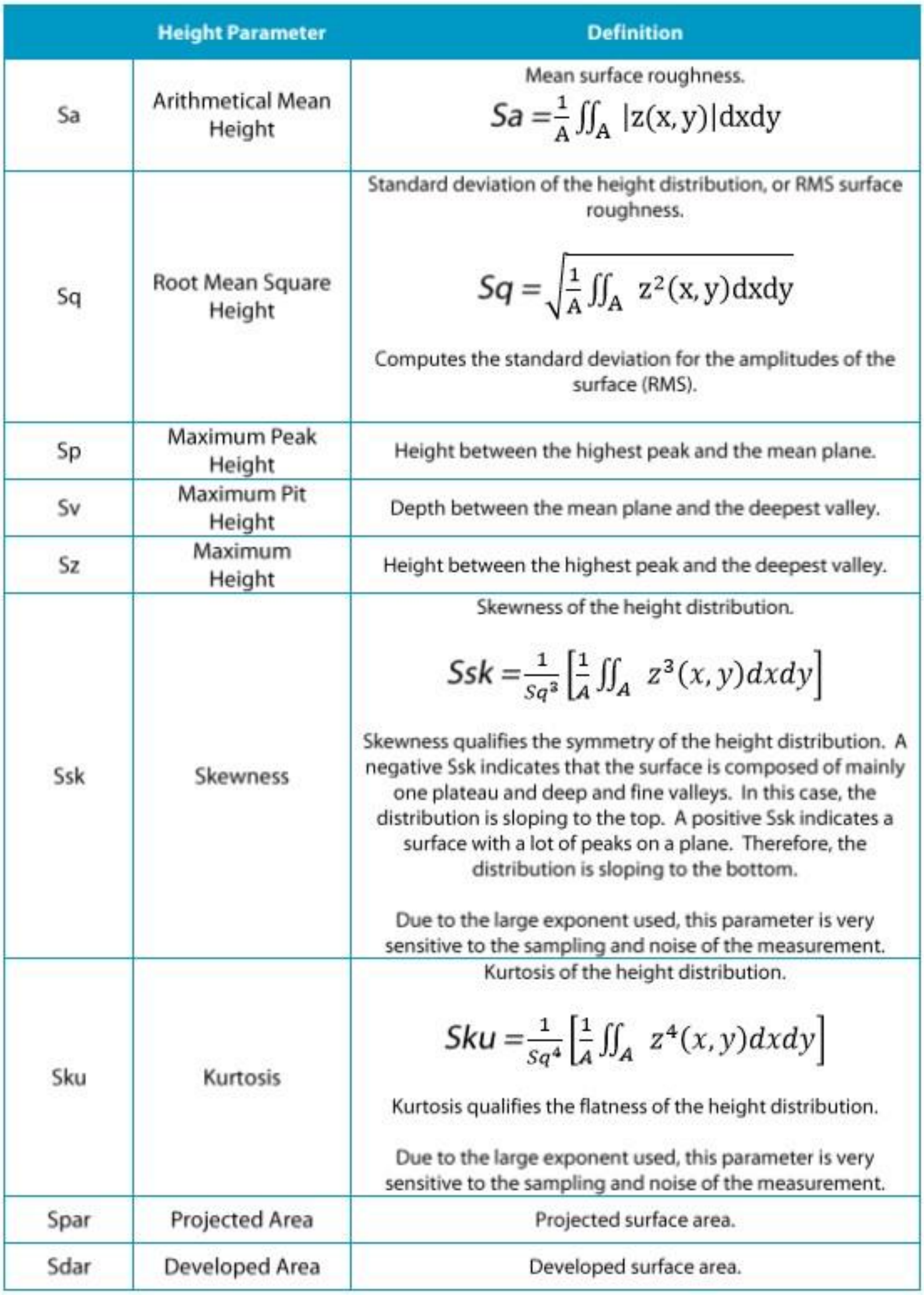

Height Parameter		Definition
Sa	Arithmetical Mean Height	Mean surface roughness. $Sa = \frac{1}{A}\iint_A \lvert z(x,y)\rvert dxdy$
Sq	Root Mean Square Height	Standard deviation of the height distribution, or RMS surface roughness. $Sq = \sqrt{\frac{1}{A}\iint_A z^2(x,y)dxdy}$ Computes the standard deviation for the amplitudes of the surface (RMS).
Sp	Maximum Peak Height	Height between the highest peak and the mean plane.
Sv	Maximum Pit Height	Depth between the mean plane and the deepest valley.
Sz	Maximum Height	Height between the highest peak and the deepest valley.
Ssk	Skewness	Skewness of the height distribution. $Ssk = \frac{1}{Sq^3}\left[\frac{1}{A}\iint_A z^3(x,y)dxdy\right]$ Skewness qualifies the symmetry of the height distribution. A negative Ssk indicates that the surface is composed of mainly one plateau and deep and fine valleys. In this case, the distribution is sloping to the top. A positive Ssk indicates a surface with a lot of peaks on a plane. Therefore, the distribution is sloping to the bottom. Due to the large exponent used, this parameter is very sensitive to the sampling and noise of the measurement.
Sku	Kurtosis	Kurtosis of the height distribution. $Sku = \frac{1}{Sq^4}\left[\frac{1}{A}\iint_A z^4(x,y)dxdy\right]$ Kurtosis qualifies the flatness of the height distribution. Due to the large exponent used, this parameter is very sensitive to the sampling and noise of the measurement.
Spar	Projected Area	Projected surface area.
Sdar	Developed Area	Developed surface area.

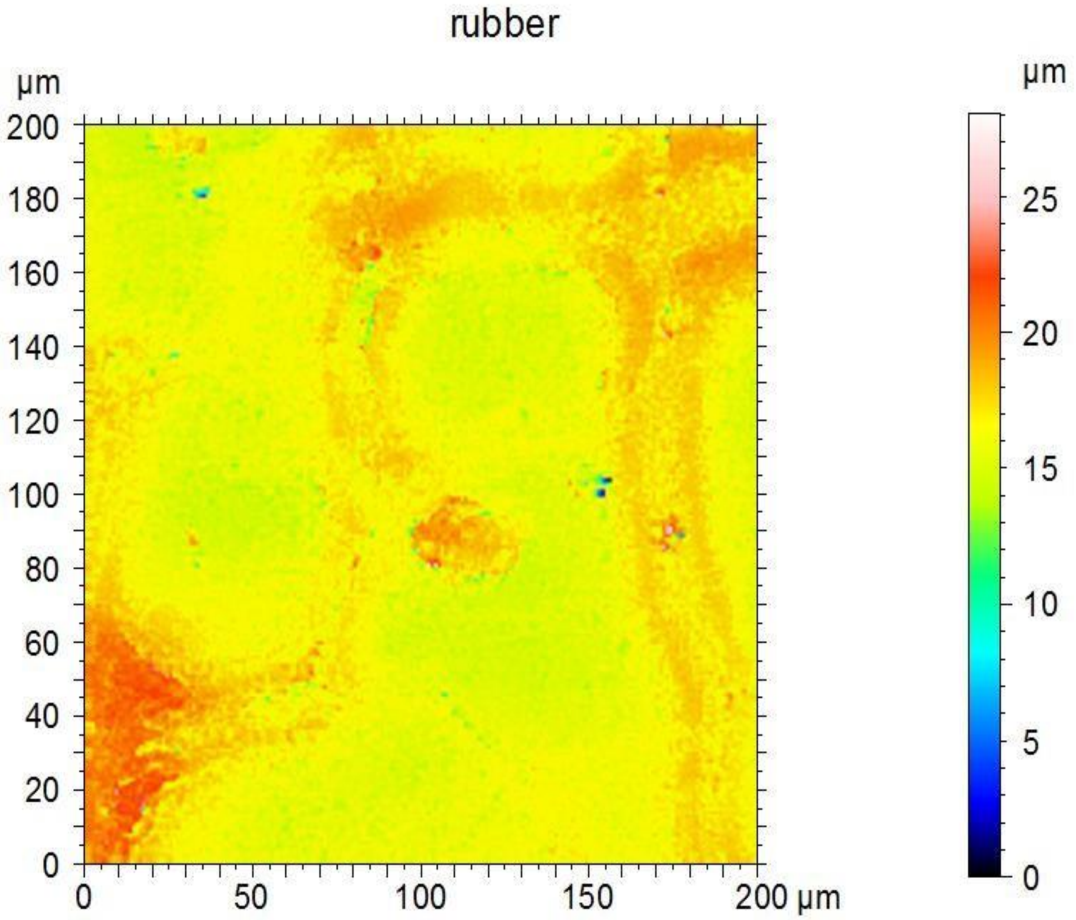

Figure B.1: Two-dimensional view of vulcanized NR SBR5 surface roughness, measured by an optical profilometer.

Table B.2: Surface roughness parameters for vulcanized natural rubber compound used as a rubber lining in a steel-encased hydrocyclone.

Height parameter	Value	Meaning
Sq	1.42 μm	Root-mean-square height
Ssk	0.66	Skewness
Sku	6.54	Kurtosis
Sp	11.54 μm	Maximum peak height
Sv	16.50 μm	Maximum pit height
Sz	28.05 μm	Maximum height
Sa	1.1 μm	Arithmetic mean height

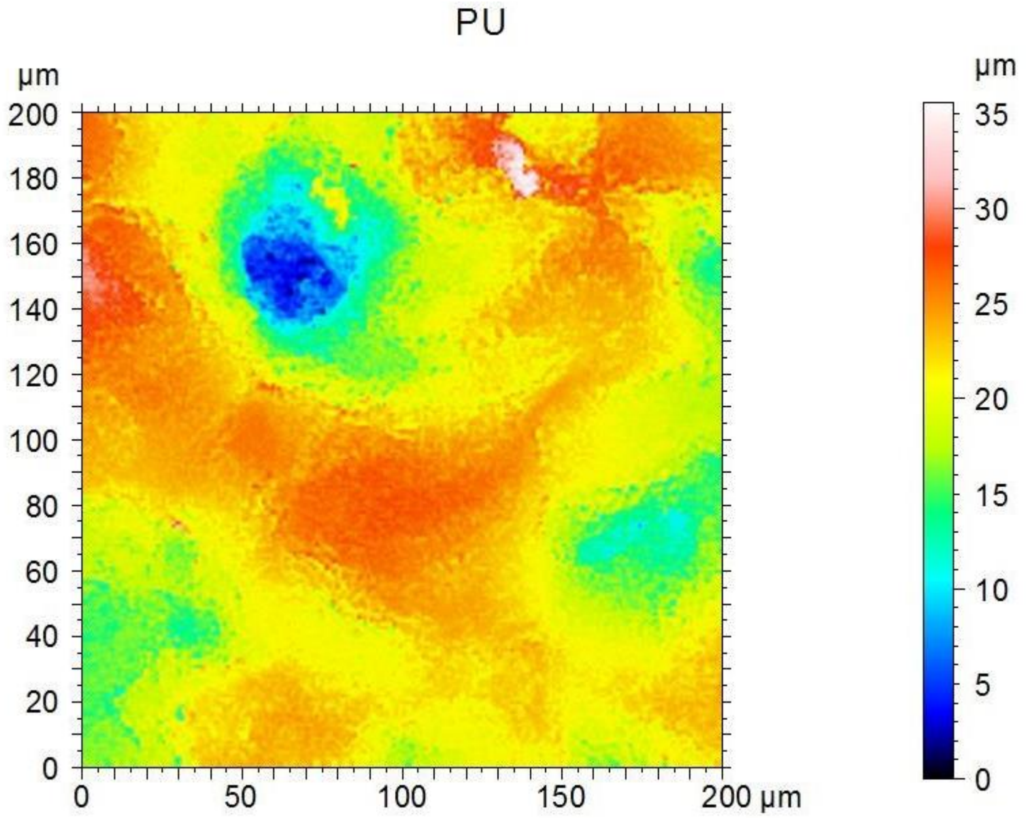

Figure B.2: Two-dimensional view of PU Elasturan 6055/114 surface roughness, measured by an optical profilometer.

Table B0.3: Surface roughness parameters for Elasturan 6055/114 polyurethane hydrocyclone material supplied by BASF.

Height parameter	Value	Meaning
Sq	4.25 µm	Root-mean-square height
Ssk	-1.01	Skewness
Sku	4.88	Kurlosis
Sp	14.74 µm	Maximum peak height
Sv	20.81 µm	Maximum pit height
Sz	35.556 µm	Maximum height
Sa	3.24 µm	Arithmetic mean height

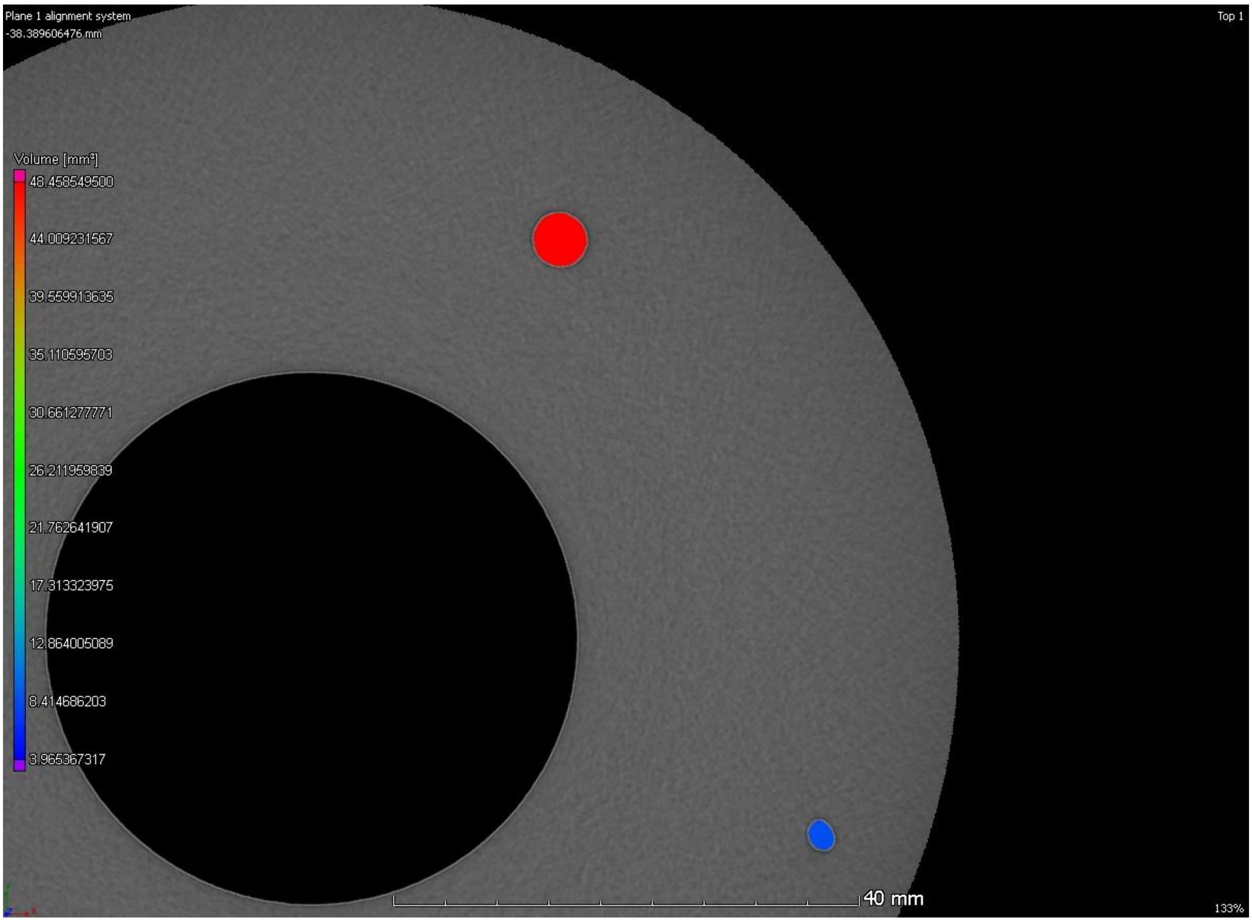

Figure B.3: Image of void volume in 35 mm spigot.

APPENDIX C: HARDNESS RESULTS

Table C.1: Hardness and DIN results for various vulcanized natural rubbers compounds

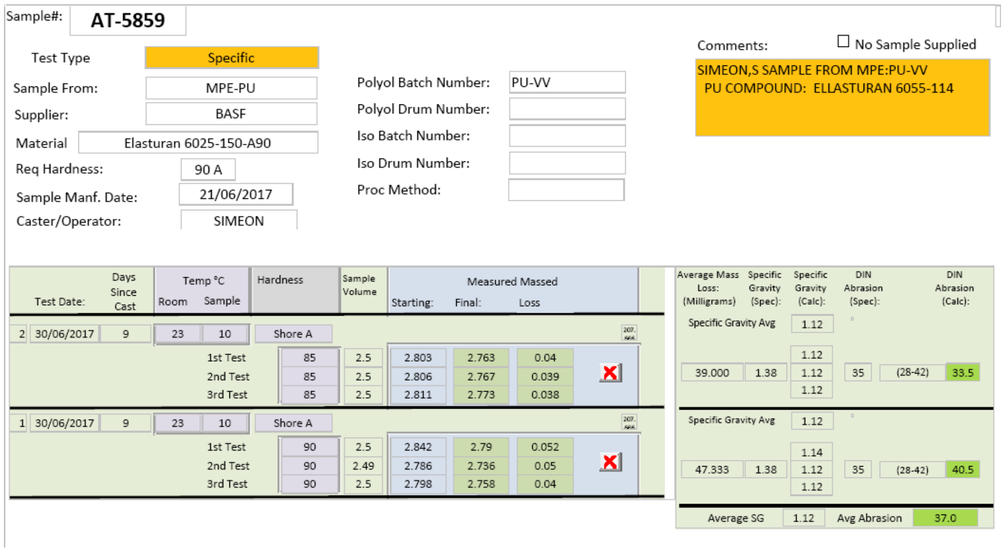

Sample#: **AT-5859**

Test Type: Specific
Sample From: MPE-PU
Supplier: BASF
Material: Elasturan 6025-150-A90
Req Hardness: 90 A
Sample Manf. Date: 21/06/2017
Caster/Operator: SIMEON

Polyol Batch Number: PU-VV
Polyol Drum Number:
Iso Batch Number:
Iso Drum Number:
Proc Method:

Comments: ☐ No Sample Supplied
SIMEON,S SAMPLE FROM MPE:PU-VV
PU COMPOUND: ELLASTURAN 6055-114

	Test Date:	Days Since Cast	Temp °C Room	Temp °C Sample	Hardness		Sample Volume	Measured Massed Starting:	Final:	Loss
2	30/06/2017	9	23	10	Shore A					
					1st Test	85	2.5	2.803	2.763	0.04
					2nd Test	85	2.5	2.806	2.767	0.039
					3rd Test	85	2.5	2.811	2.773	0.038
1	30/06/2017	9	23	10	Shore A					
					1st Test	90	2.5	2.842	2.79	0.052
					2nd Test	90	2.49	2.786	2.736	0.05
					3rd Test	90	2.5	2.798	2.758	0.04

Average Mass Loss: (Milligrams)	Specific Gravity (Spec):	Specific Gravity (Calc):	DIN Abrasion (Spec):		DIN Abrasion (Calc):
Specific Gravity Avg		1.12			
		1.12			
39.000	1.38	1.12	35	(28-42)	33.5
		1.12			
Specific Gravity Avg		1.12			
		1.14			
47.333	1.38	1.12	35	(28-42)	40.5
		1.12			

Average SG 1.12 Avg Abrasion 37.0

Rubber												
		Shore Hardness						Hardness	DIN			
Rubber type		Reading 1	Reading 2	Reading 3	Reading 4	Reading 5	**Average**	Loyiso	Reading 1	Reading 2	Reading 3	Average
Sample 1	Blue	43	42	42	42	43	42.25	50	53.3	52	46	50.43333
Sample 2	Red	44	45	44	45	45	44.5	52	77.8	78	74	76.6
Sample 3	Yellow (HC)	52	54	53	54	52	53.25	63	102.3	106.6	101.7	103.5333
Sample 4	Green	55	56	56	56	56	55.75	58	150.6	123	123	132.2

APPENDIX D: TENSILE TEST RESULTS

Table D.1: Tensile test results for Elasturan 6055/114 PU samples.

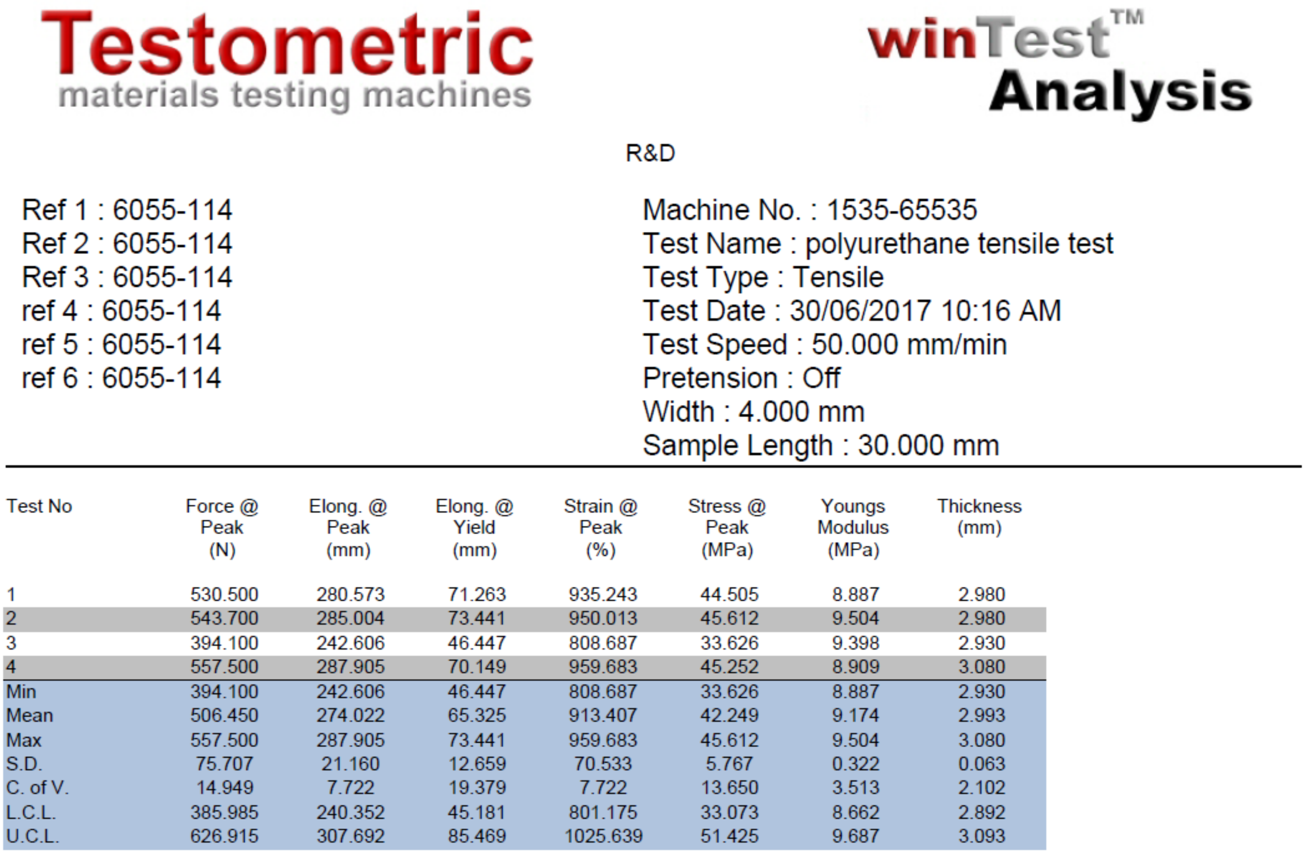

Testometric
materials testing machines

winTest™
Analysis

R&D

Ref 1 : 6055-114
Ref 2 : 6055-114
Ref 3 : 6055-114
ref 4 : 6055-114
ref 5 : 6055-114
ref 6 : 6055-114

Machine No. : 1535-65535
Test Name : polyurethane tensile test
Test Type : Tensile
Test Date : 30/06/2017 10:16 AM
Test Speed : 50.000 mm/min
Pretension : Off
Width : 4.000 mm
Sample Length : 30.000 mm

Test No	Force @ Peak (N)	Elong. @ Peak (mm)	Elong. @ Yield (mm)	Strain @ Peak (%)	Stress @ Peak (MPa)	Youngs Modulus (MPa)	Thickness (mm)
1	530.500	280.573	71.263	935.243	44.505	8.887	2.980
2	543.700	285.004	73.441	950.013	45.612	9.504	2.980
3	394.100	242.606	46.447	808.687	33.626	9.398	2.930
4	557.500	287.905	70.149	959.683	45.252	8.909	3.080
Min	394.100	242.606	46.447	808.687	33.626	8.887	2.930
Mean	506.450	274.022	65.325	913.407	42.249	9.174	2.993
Max	557.500	287.905	73.441	959.683	45.612	9.504	3.080
S.D.	75.707	21.160	12.659	70.533	5.767	0.322	0.063
C. of V.	14.949	7.722	19.379	7.722	13.650	3.513	2.102
L.C.L.	385.985	240.352	45.181	801.175	33.073	8.662	2.892
U.C.L.	626.915	307.692	85.469	1025.639	51.425	9.687	3.093

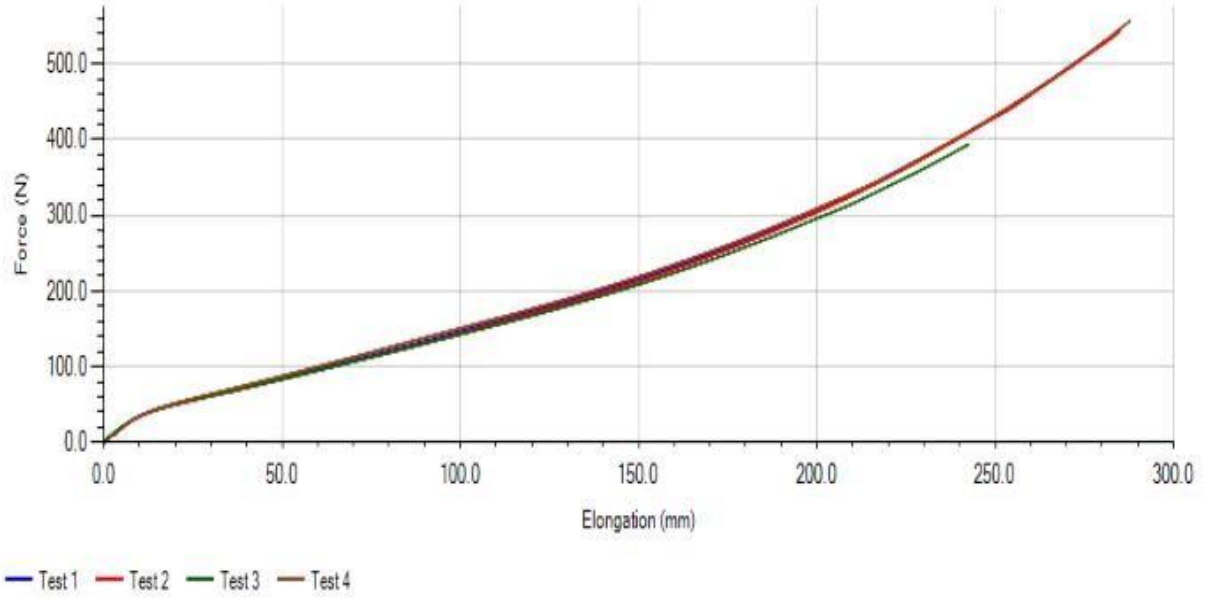

Figure D.1: Tensile test results for Elasturan 6055/114 PU samples.

Table D.2: Tensile test results for vulcanized NR VBR5 samples.

Testometric
materials testing machines

winTest™
Analysis

RUBBER HC tensile test

Ref 1 : COMP 4001 S1
Ref 2 : COMP 4001 S2
Ref 3 : COMP 4001 S3
ref 4 : COMP 4001 S4
ref 5 :
ref 6 :

Machine No. : 1535-65535
Test Name : polyurethane tensile test
Test Type : Tensile
Test Date : 02/08/2017 11:38 AM
Test Speed : 50.000 mm/min
Pretension : Off
Width : 4.000 mm
Sample Length : 30.000 mm

Test No	Force @ Peak (N)	Elong. @ Peak (mm)	Elong. @ Yield (mm)	Strain @ Peak (%)	Stress @ Peak (MPa)	Youngs Modulus (MPa)	Thickness (mm)
1	440.600	369.200	155.569	1230.667	19.670	0.774	5.600
2	447.800	374.572	143.889	1248.573	19.991	0.770	5.600
3	396.200	357.121	132.830	1190.403	17.688	0.777	5.600
4	415.100	357.823	130.300	1192.743	18.868	0.834	5.500
Min	396.200	357.121	130.300	1190.403	17.688	0.770	5.500
Mean	424.925	364.679	140.647	1215.597	19.054	0.789	5.575
Max	447.800	374.572	155.569	1248.573	19.991	0.834	5.600
S.D.	23.739	8.611	11.566	28.703	1.026	0.030	0.050
C. of V.	5.587	2.361	8.224	2.361	5.385	3.825	0.897
L.C.L.	387.151	350.977	122.243	1169.925	17.421	0.741	5.495
U.C.L.	462.699	378.381	159.051	1261.268	20.687	0.837	5.655

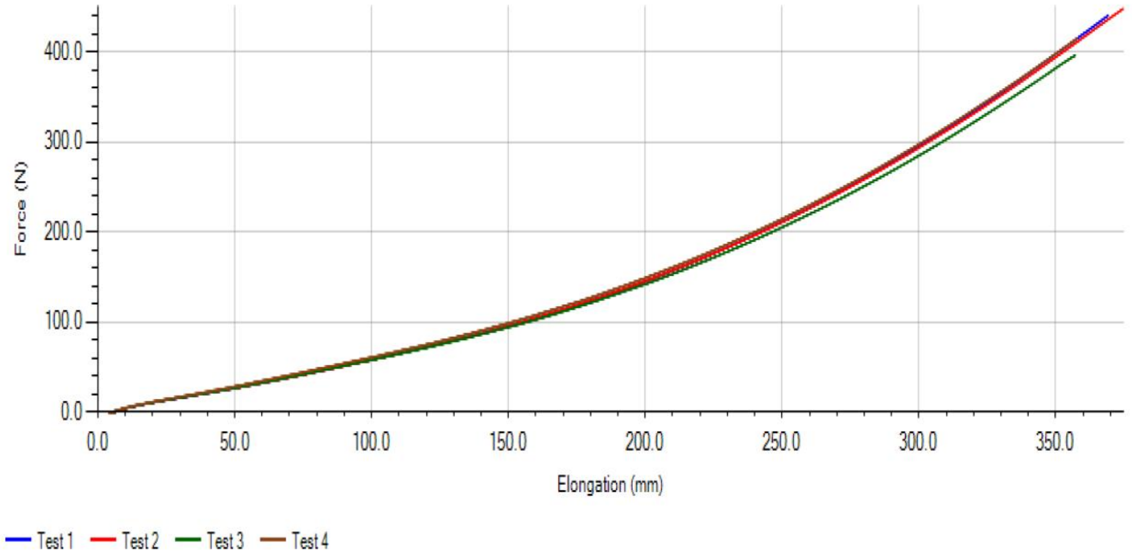

Figure D.2: Tensile test results for vulcanized NR VBR5 samples.

APPENDIX E: MATERIAL PROPERTIES

Table E.1. Elasturan (polyurethane) materials recommended for use in an erosive mining environment (BASF).

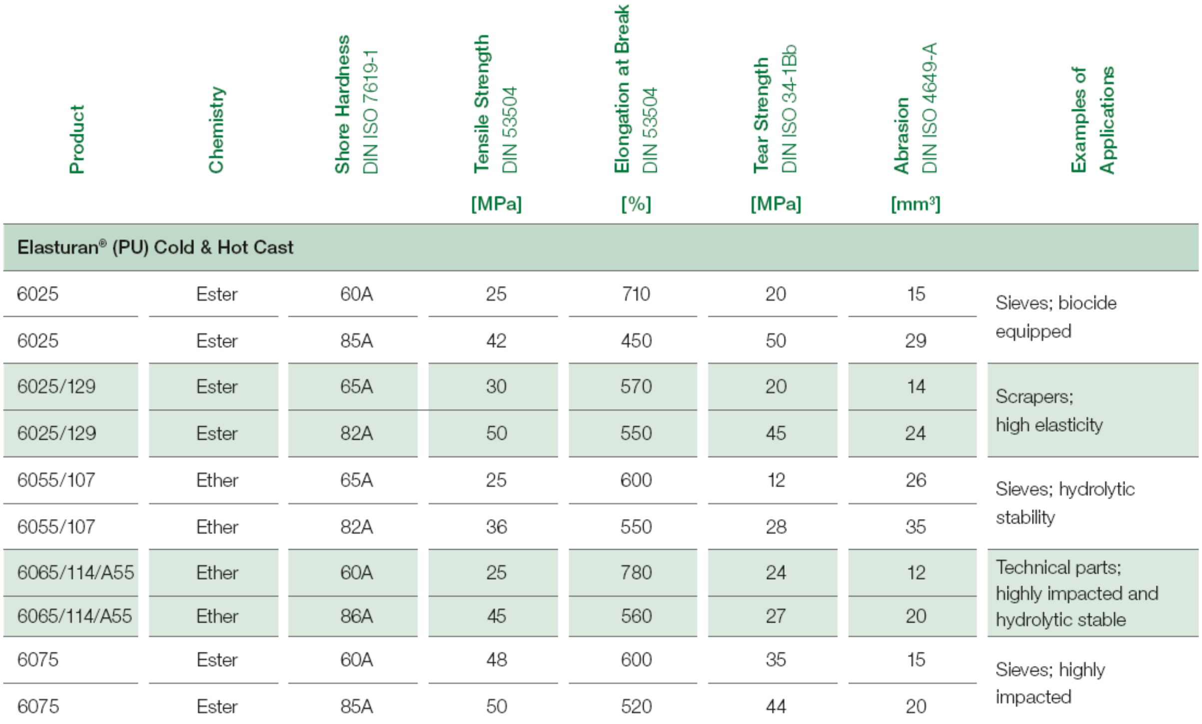

Product	**Chemistry**	**Shore Hardness** DIN ISO 7619-1	**Tensile Strength** DIN 53504 **[MPa]**	**Elongation at Break** DIN 53504 **[%]**	**Tear Strength** DIN ISO 34-1Bb **[MPa]**	**Abrasion** DIN ISO 4649-A **[mm^3]**	**Examples of Applications**
Elasturan® (PU) Cold & Hot Cast							
6025	Ester	60A	25	710	20	15	Sieves; biocide equipped
6025	Ester	85A	42	450	50	29	
6025/129	Ester	65A	30	570	20	14	Scrapers; high elasticity
6025/129	Ester	82A	50	550	45	24	
6055/107	Ether	65A	25	600	12	26	Sieves; hydrolytic stability
6055/107	Ether	82A	36	550	28	35	
6065/114/A55	Ether	60A	25	780	24	12	Technical parts; highly impacted and hydrolytic stable
6065/114/A55	Ether	86A	45	560	27	20	
6075	Ester	60A	48	600	35	15	Sieves; highly impacted
6075	Ester	85A	50	520	44	20	

Table E.2.: Material datasheet of Elasturan 6055/114 BASF, hand-cast PU.

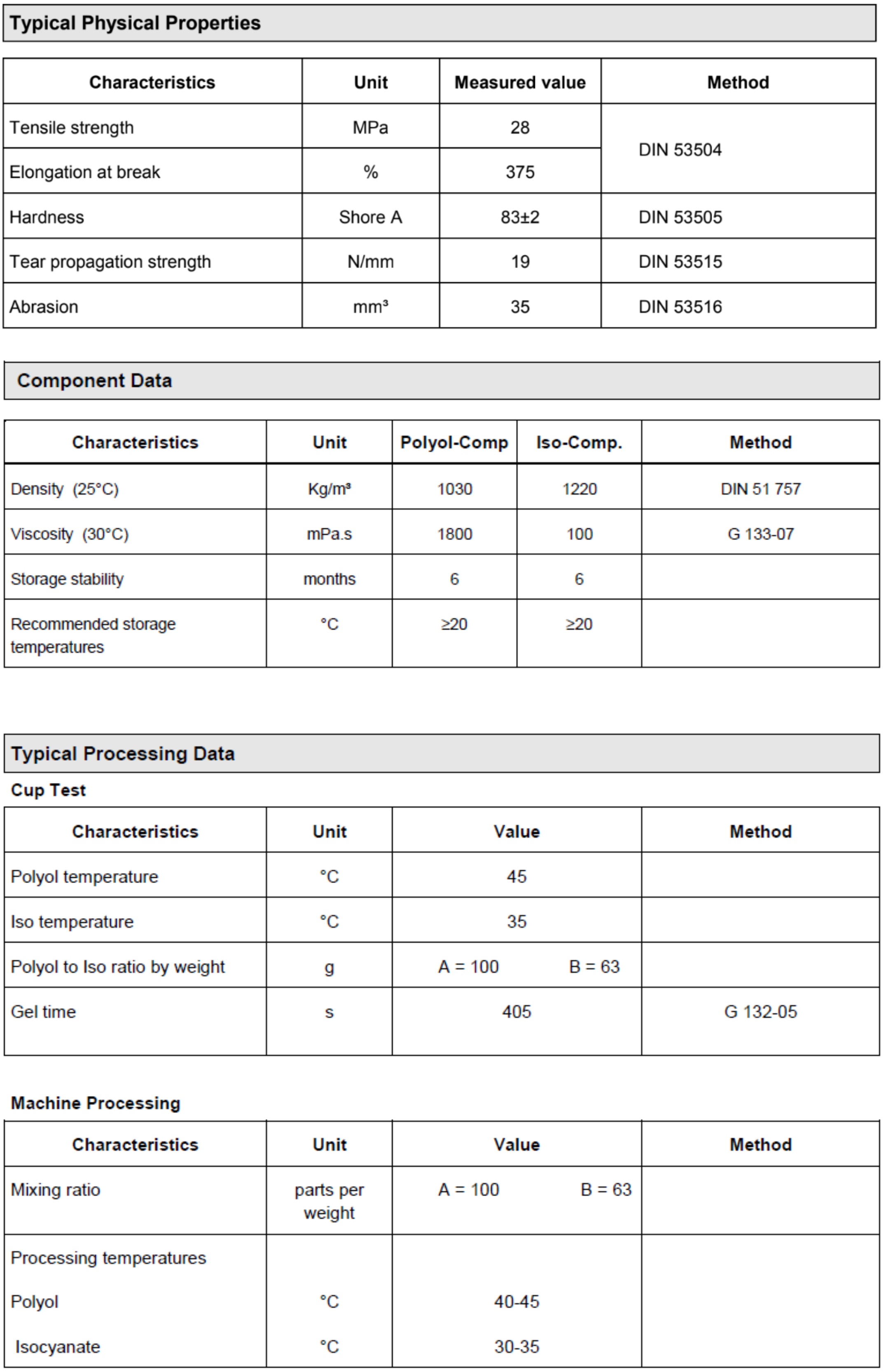

Typical Physical Properties

Characteristics	Unit	Measured value	Method
Tensile strength	MPa	28	DIN 53504
Elongation at break	%	375	
Hardness	Shore A	83±2	DIN 53505
Tear propagation strength	N/mm	19	DIN 53515
Abrasion	mm³	35	DIN 53516

Component Data

Characteristics	Unit	Polyol-Comp	Iso-Comp.	Method
Density (25°C)	Kg/m³	1030	1220	DIN 51 757
Viscosity (30°C)	mPa.s	1800	100	G 133-07
Storage stability	months	6	6	
Recommended storage temperatures	°C	≥20	≥20	

Typical Processing Data

Cup Test

Characteristics	Unit	Value	Method
Polyol temperature	°C	45	
Iso temperature	°C	35	
Polyol to Iso ratio by weight	g	A = 100 B = 63	
Gel time	s	405	G 132-05

Machine Processing

Characteristics	Unit	Value	Method
Mixing ratio	parts per weight	A = 100 B = 63	
Processing temperatures			
Polyol	°C	40-45	
Isocyanate	°C	30-35	

Table E.3: Material datasheet of Huntsman Irogran A85 thermoplastic polyurethane used for hydrocyclone injection moulding.

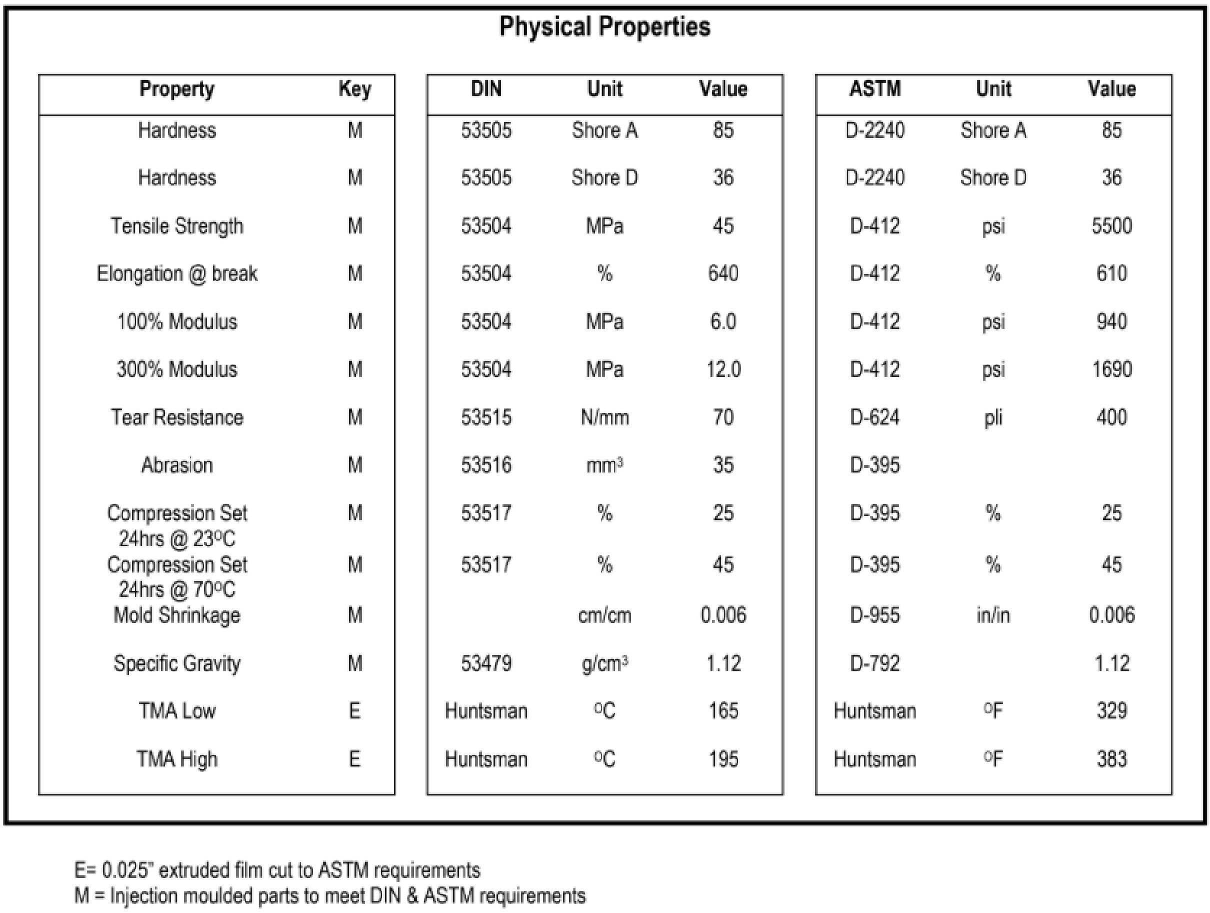

Physical Properties

Property	Key	DIN	Unit	Value	ASTM	Unit	Value
Hardness	M	53505	Shore A	85	D-2240	Shore A	85
Hardness	M	53505	Shore D	36	D-2240	Shore D	36
Tensile Strength	M	53504	MPa	45	D-412	psi	5500
Elongation @ break	M	53504	%	640	D-412	%	610
100% Modulus	M	53504	MPa	6.0	D-412	psi	940
300% Modulus	M	53504	MPa	12.0	D-412	psi	1690
Tear Resistance	M	53515	N/mm	70	D-624	pli	400
Abrasion	M	53516	mm^3	35	D-395		
Compression Set 24hrs @ 23°C	M	53517	%	25	D-395	%	25
Compression Set 24hrs @ 70°C	M	53517	%	45	D-395	%	45
Mold Shrinkage	M		cm/cm	0.006	D-955	in/in	0.006
Specific Gravity	M	53479	g/cm^3	1.12	D-792		1.12
TMA Low	E	Huntsman	°C	165	Huntsman	°F	329
TMA High	E	Huntsman	°C	195	Huntsman	°F	383

E= 0.025" extruded film cut to ASTM requirements
M = Injection moulded parts to meet DIN & ASTM requirements

Table E.4: Composition of natural rubber used for rubber lining of hydrocyclone.

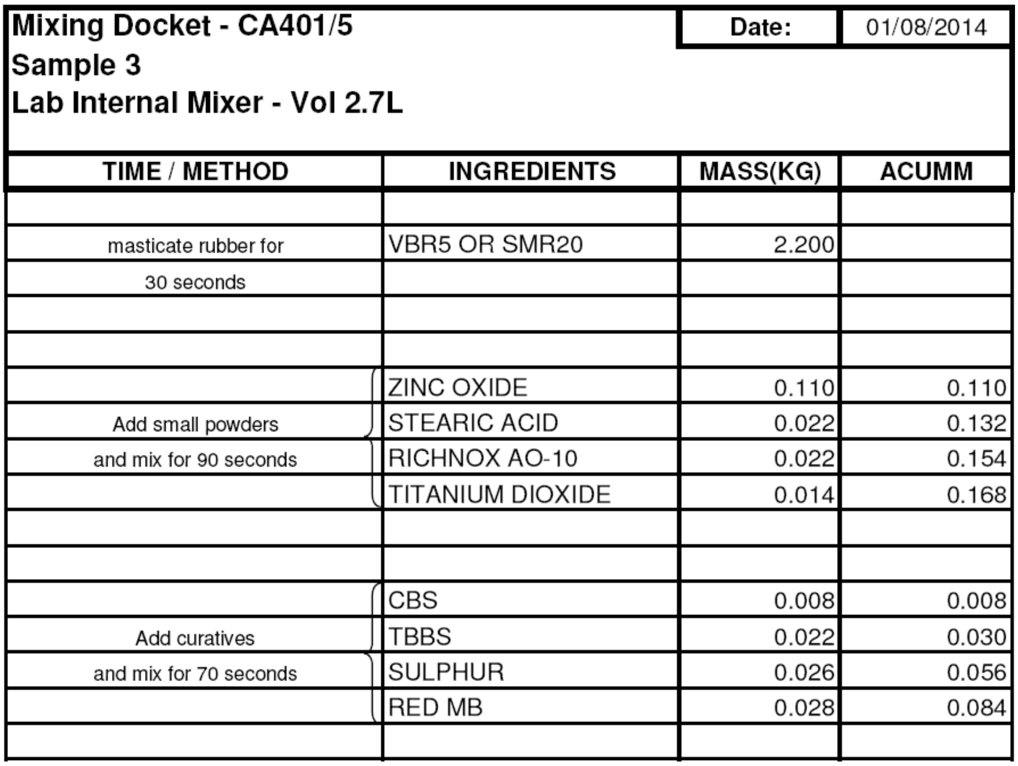

Mixing Docket - CA401/5
Sample 3
Lab Internal Mixer - Vol 2.7L

Date: 01/08/2014

TIME / METHOD	INGREDIENTS	MASS(KG)	ACUMM
masticate rubber for 30 seconds	VBR5 OR SMR20	2.200	
Add small powders and mix for 90 seconds	ZINC OXIDE	0.110	0.110
	STEARIC ACID	0.022	0.132
	RICHNOX AO-10	0.022	0.154
	TITANIUM DIOXIDE	0.014	0.168
Add curatives and mix for 70 seconds	CBS	0.008	0.008
	TBBS	0.022	0.030
	SULPHUR	0.026	0.056
	RED MB	0.028	0.084

Table E.5: Defects that can occur in polyurethane hand-casting (Clemitson, 2008).

Problem	Observation	Cause
Striations	Finished product	Poor mixing
		Off ratio
Voids in material	Fine bubbles	Moisture in system
	Small bubbles randomly in part	Pouring technique
		Dirty mould Temperature and viscosity
	Large voids	High exothermicity Temperature and viscosity
		Casting technique
		Dirty moulds.
		Mould design
Foaming	In solid materials	Moisture in curative
		Very moist prepolymer
High shrinkage	Level of material lower than design of moulds and vents	Incorrect temperature of mould and polyurethane
		High exotherm
		Wrong ratios
		System contaminated
Cracking of part	On demoulding	Low green strength
		Incorrect temperature of mould and polyurethane
		High exotherm
		Wrong ratios
		Poor mixing
		Casting technique
Wet spots	On surface of part	Poor mixing
		Off ratio
Physical properties	Low hardness, tensile strength and tear strength	Wrong curative ratios
		Prepolymer degraded
		Not fully cured
		Poor mixing

APPENDIX F: DETAILED EXPERIMENTAL RESULTS

F.1 New Spigot Efficiency Test

Table F.1: Efficiency test results: feed relative density of new spigot.

Feed RD New Spigot				
Mass + tare (kg)	Tare (kg)	Mass (kg)	Vol (l)	RD
2.10	0.48	1.62	1.42	1.14
2.03	0.48	1.55	1.36	1.14
2.16	0.48	1.68	1.47	1.15

Table F.2: Efficiency test results: underflow relative density using new spigot.

U/F RD New Spigot						
Mass + tare (kg)	Tare (kg)	Mass (kg)	Vol (l)	RD	Volume per cut (l)	U/F flowrate (m^3/h)
1.645	0.475	1.170	0.830	1.410	0.083	8.068
2.090	0.475	1.615	1.160	1.392	0.116	11.275
2.375	0.475	1.900	1.360	1.397	0.136	13.219

Table F.3: Efficiency test results: overflow relative density using new spigot.

O/F RD New Spigot						
Mass + tare (kg)	Tare (kg)	Mass (kg)	Vol (l)	RD	Volume per cut (l)	U/F flowrate (m^3/h)
1.945	0.475	1.470	1.400	1.050	0.700	40.320
1.970	0.475	1.495	1.420	1.053	0.710	40.896
2.145	0.475	1.670	1.600	1.044	0.800	46.080

Table F.4: Efficiency test results: underflow sample characteristics using new spigot.

U/F sample New Spigot						
Sample no.	Mass + tare (kg)	Tare (kg)	Slurry mass (kg)	Solids mass (kg)	Solids (%)	Malvern sample mass (g)
1	5.095	0.915	4.180	1.872	44.794	18.6
2	5.475	0.900	4.575	1.916	41.871	19.5
3	5.470	0.900	4.570	1.858	40.656	18.5

Table F.5: Efficiency test results: overflow sample characteristics using new spigot.

O/F sample New Spigot						
Sample no.	Mass + tare (kg)	Tare (kg)	Slurry mass (kg)	Solids mass (kg)	Solids (%)	Malvern sample mass (g)
1	8.475	0.930	7.545	0.613	8.130	6.2
2	8.225	0.900	7.325	0.593	8.090	6.0
3	8.235	0.900	7.335	0.580	7.907	6.7

Table F.6: Efficiency test results: Feed sample characteristics using new spigot.

Feed samples New Spigot						
Sample no.	Mass + tare (kg)	Tare (kg)	Slurry mass (kg)	Solids mass (kg)	Solids (%)	Malvern sample mass (g)
1.000	7.400	0.310	7.090	1.377	19.416	13.79
2.000	8.150	0.315	7.835	1.559	19.898	15.50
3.000	8.795	0.310	8.485	1.590	18.741	15.70

Table F.7: New spigot Malvern results

Feed sample - New Spigot			
Size (µm)	Sample 1 (vol % retained)	Sample 2 (vol % retained)	Sample 3 (vol % retained)
2000	0	0.014759	0.13442
1700	0	0.047241	0.348261
1400	0.049558	0.12087	0.498402
1180	1.018872	1.319583	1.787548
850	4.091709	4.238708	3.733855
600	6.934669	6.793599	5.505456
425	7.365134	7.127577	5.927079
300	3.134367	3.057382	2.696317
250	2.298474	2.26822	2.119362
212	3.845969	3.832898	3.943561
150	4.307435	4.179527	4.578299
106	2.609708	2.468509	2.678651
90	3.374822	3.157903	3.385092
75	4.643384	4.314575	4.577246
60	6.378213	5.903924	6.224831
45	3.741951	3.462047	3.642883
38	8.753778	8.129988	8.54168
25	9.362909	8.804202	9.267724
15	6.205819	5.94212	6.394852
10	7.782386	7.869434	8.888665
5	1.929471	2.141871	2.371125
4	9.202537	11.231819	9.889522
1	2.968835	3.573244	2.865169

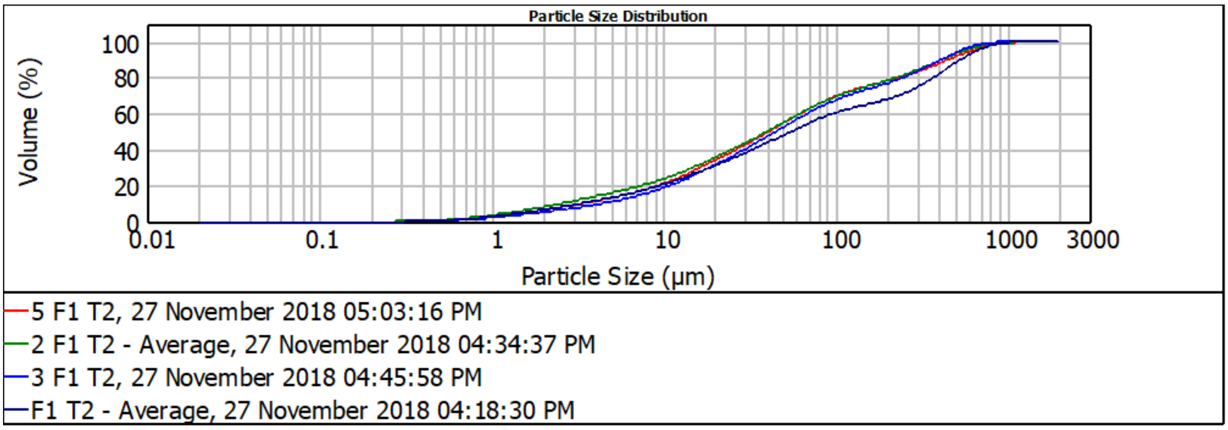

Figure F.1: Feed sample 1, new spigot, Malvern Mastersizer 2000 results.

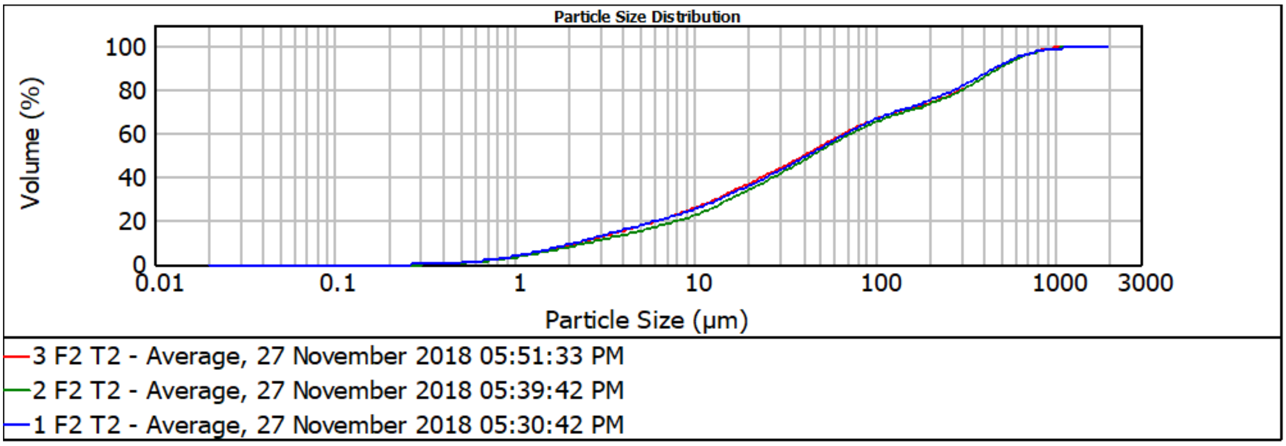

Figure F.2: Feed sample 2, new spigot, Malvern Mastersizer 2000 results.

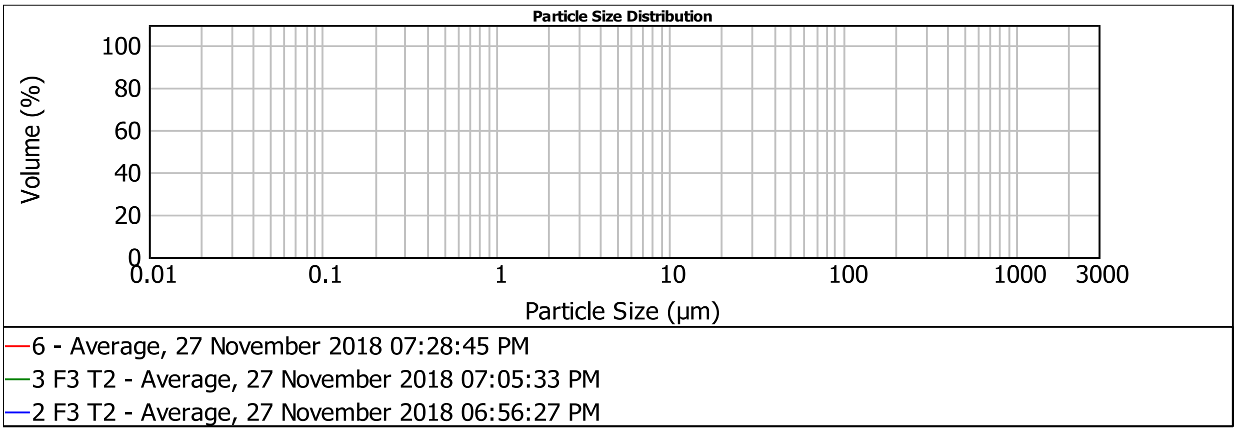

Figure F.3: Feed sample 3, new spigot, Malvern Mastersizer 2000 results.

Table F.8: New Spigot Malvern results

Underflow sample - New Spigot			
Size (µm)	Sample 1 (vol % retained)	Sample 2 (vol % retained)	Sample 3 (vol % retained)
2000	0.052326	0.018628	0.010968
1700	0.115524	0.044483	0.024787
1400	0.122348	0.051431	0.032627
1180	0.230268	0.137406	0.091246
850	0.359824	0.378384	0.230872
600	0.712261	0.708587	0.581693
425	0.728121	0.584866	0.57109
300	0.251578	0.138208	0.175983
250	0.266623	0.153767	0.205806
212	1.991356	1.663035	1.787481
150	6.973092	6.36685	6.464041
106	5.743382	5.336783	5.375639
90	8.193377	7.672973	7.727698
75	11.891184	11.232069	11.334705
60	16.179784	15.483128	15.67381
45	8.749851	8.508891	8.62904
38	16.007182	16.081557	16.280484
25	8.729344	9.623334	9.623473
15	2.765784	3.449507	3.409736
10	3.085654	3.865854	3.753161
5	0.831762	1.061859	0.962955
4	4.355435	5.503487	5.003475
1	1.66394	1.934913	2.04923

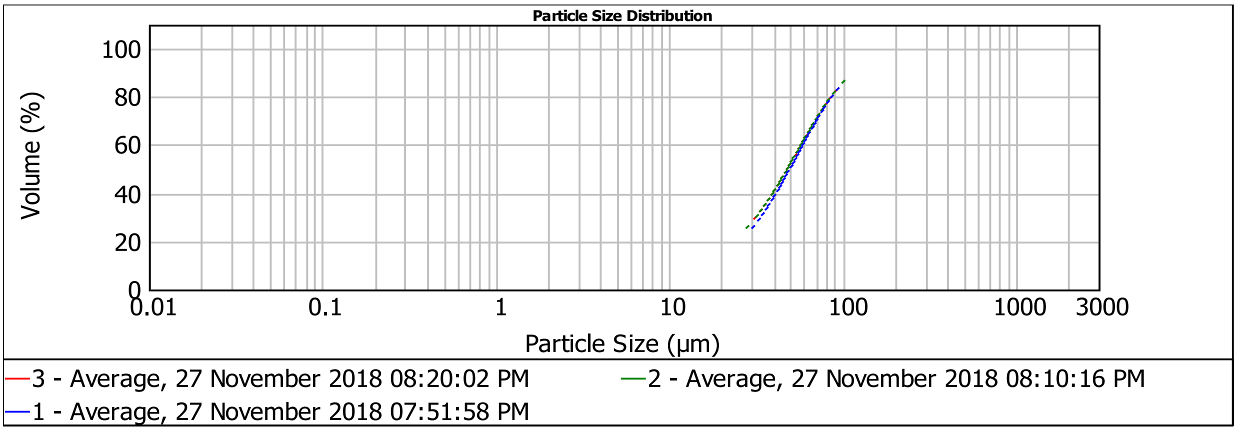

Figure F.4: Underflow, sample 1, new spigot Malvern Mastersizer 2000 results.

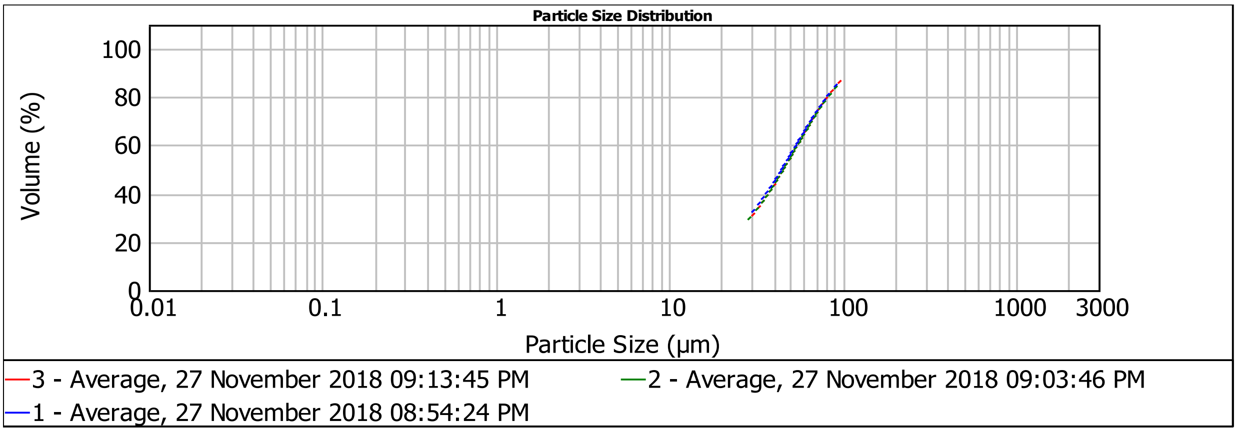

Figure F.5: Underflow, sample 2, new spigot Malvern Mastersizer 2000 results.

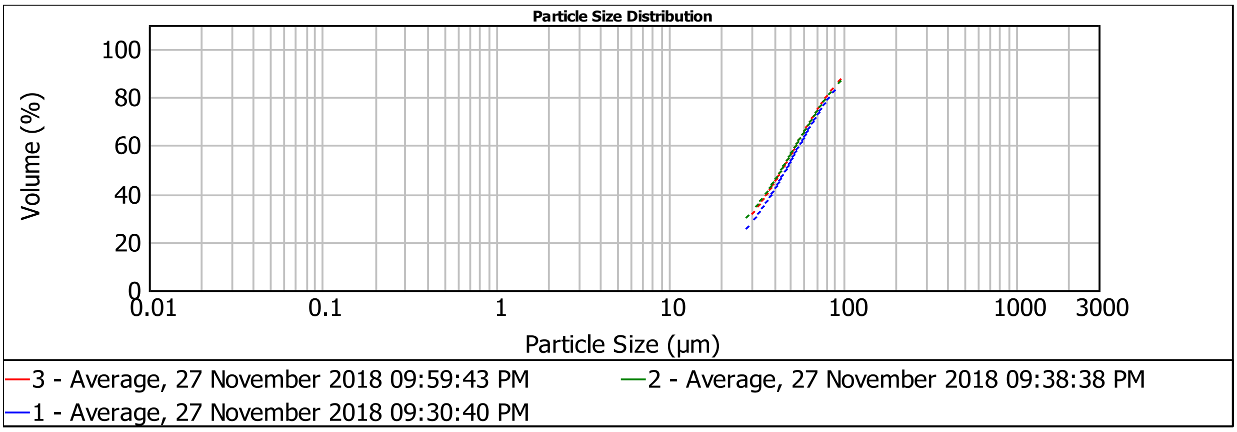

Figure F.6: Underflow, sample 3, new spigot Malvern Mastersizer 2000 results.

Table F.9*:* New spigot Malvern results

Overflow sample - New Spigot			
Size (µm)	Sample 1 (vol % retained)	Sample 2 (vol % retained)	Sample 3 (vol % retained)
2000	0	0	0
1700	0	0	0
1400	0	0	0
1180	0	0	0
850	0	0	0
600	0	0	0
425	0	0	0
300	0	0	0
250	0	0	0
212	0.001392	0.005689	0.017357
150	0.281812	0.204587	0.131247
106	0.359701	0.294293	0.169829
90	0.709425	0.590567	0.335144
75	1.557594	1.326524	0.743101
60	3.662823	3.141289	1.765312
45	3.232868	2.771202	1.580187
38	11.578604	9.971614	6.05674
25	18.297894	16.176846	11.962971
15	13.872864	12.789688	12.377777
10	17.972783	17.59996	22.537349
5	4.524927	4.773483	6.766304
4	18.594296	23.288828	28.451549
1	5.198084	7.06543	7.105133

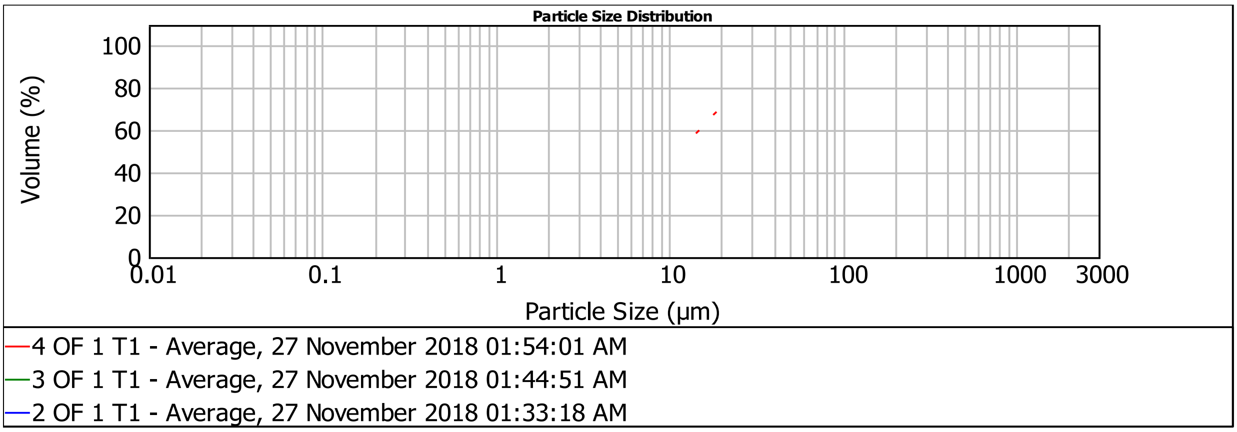

Figure F.7: Overflow, sample 1, new spigot Malvern Mastersizer 2000 results.

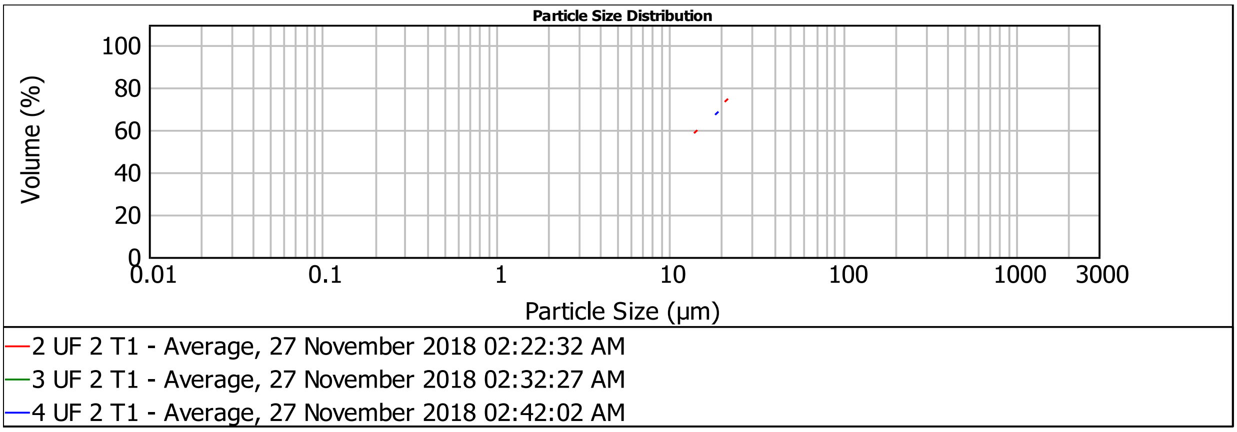

Figure F.8: Overflow, sample 2, new spigot Malvern Mastersizer 2000 results.

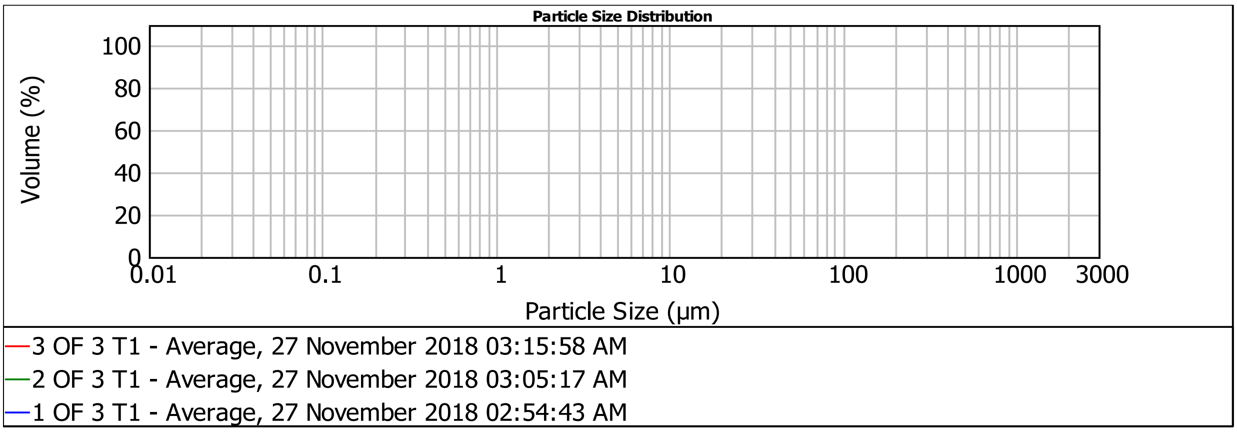

Figure F.9: Overflow, sample 3, new spigot Malvern Mastersizer 2000 results.

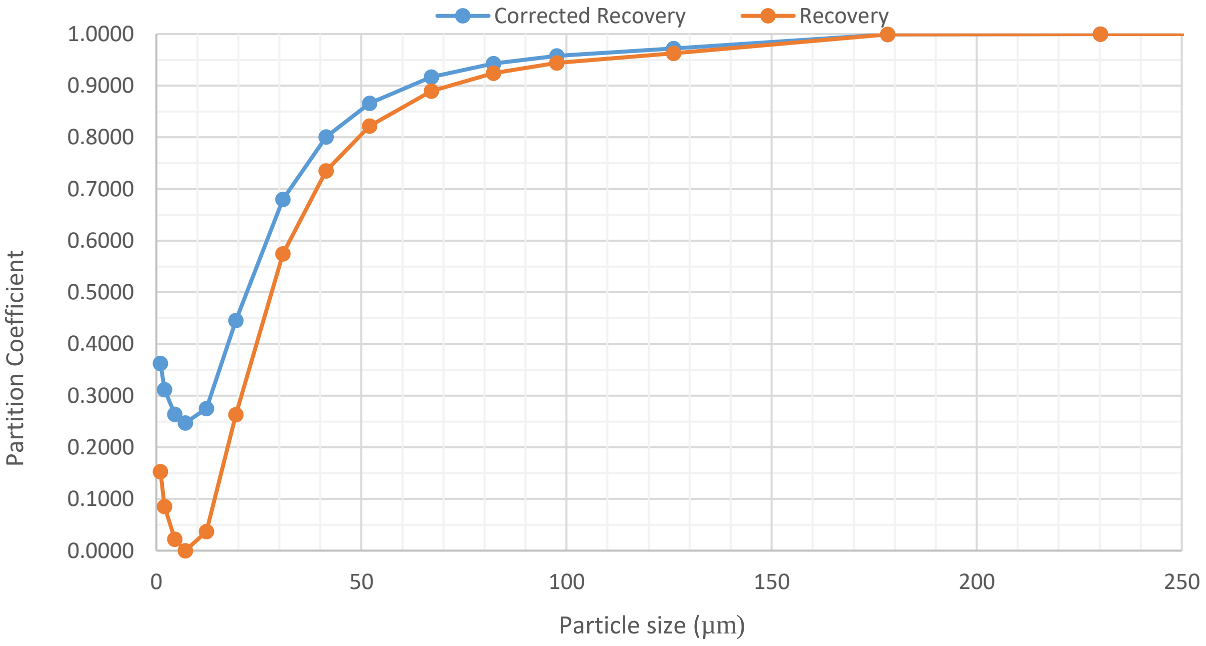

Figure F.10: Recovery to underflow and corrected recovery for new 50 mm spigot, Sample 1.

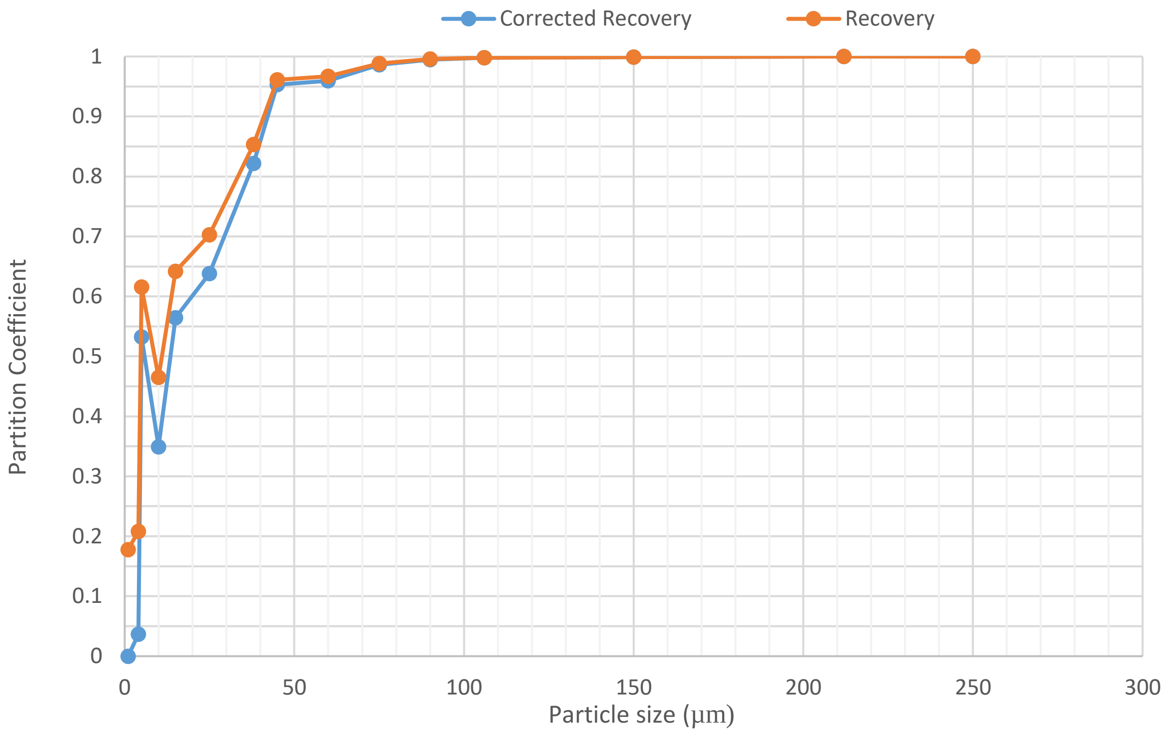

Figure F.11: Recovery to underflow and corrected recovery for new 50 mm spigot, Sample 2.

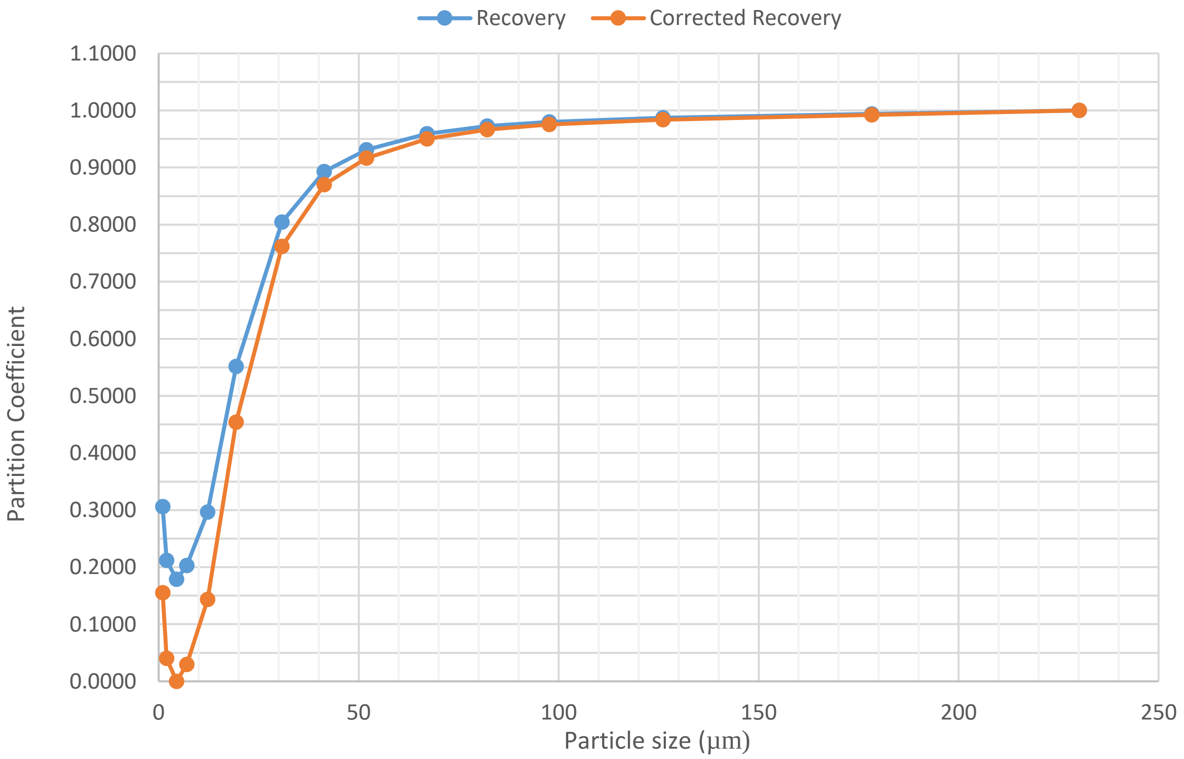

Figure F.12: Recovery to underflow and corrected recovery for new 50 mm spigot, Sample 3.

F.2 Worn Spigot Efficiency Test

Table F.10: Efficiency test results: feed relative density using worn spigot

Feed RD Worn Spigot				
Mass + tare (kg)	Tare (kg)	Mass (kg)	Vol (l)	RD
2.690	0.475	2.215	1.960	1.130
2.420	0.475	1.945	1.700	1.144
2.285	0.475	1.810	1.600	1.131
2.310	0.475	1.835	1.621	1.132

Table F.11: Efficiency test results: underflow relative density using worn spigot

U/F RD Worn Spigot						
Mass + tare (kg)	Tare (kg)	Mass (kg)	Vol (l)	RD	Volume per cut (l)	U/F flowrate (m^3/h)
2.42	0.48	1.94	1.59	1.22		
2.01	0.48	1.54	1.28	1.20	0.13	12.44
2.08	0.48	1.61	1.34	1.20	0.13	13.02

Table F.12: Efficiency test results: overflow relative density using worn spigot.

O/F RD Worn Spigot						
Mass + tare (kg)	Tare (kg)	Mass (kg)	Vol (l)	RD	Volume per cut (l)	U/F flowrate (m^3/h)
2.00	0.48	1.53	1.48	1.03	0.74	42.62
1.92	0.48	1.44	1.38	1.04	0.69	39.74
1.84	0.48	1.36	1.32	1.03	0.66	38.02

Table F.13: Efficiency test results: underflow sample characteristics using worn spigot

U/F samples Worn Spigot						
Sample no.	Mass + tare (kg)	Tare (kg)	Slurry mass (kg)	Solids mass (kg)	Solids (%)	Malvern sample mass (g)
1	7.20	0.92	6.28	1.62	25.72	6.39
2	6.99	0.90	6.09	1.46	23.90	14.17
3	7.04	0.90	6.14	1.52	24.76	15.24

Table F.14: Efficiency test results: overflow sample characteristics using worn spigot

O/F samples Worn Spigot						
Sample no.	Mass + tare (kg)	Tare (kg)	Slurry mass (kg)	Solids mass (kg)	Solids (%)	Malvern sample mass (g)
1	7.20	0.93	6.27	0.33	5.23	9.62
2	7.79	0.90	6.89	0.36	5.21	11.15
3	7.96	0.90	7.06	0.39	5.47	11.80

Table F.15: Efficiency test results: feed sample characteristics using worn spigot

Feed samples Worn Spigot						
Sample no.	Mass + tare (kg)	Tare (kg)	Slurry mass (kg)	Solids mass (kg)	Solids (%)	Malvern sample mass (g)
1	6.80	0.31	6.49	1.19	18.29	12.00
2	6.48	0.32	6.17	1.12	18.18	11.56
3	5.43	0.31	5.12	0.92	18.01	9.50

Table F.16: Worn spigot Malvern results.

Feed sample - Worn Spigot			
Size (µm)	Sample 1 (vol % retained)	Sample 2 (vol % retained)	Sample 3 (vol % retained)
2000	0.106	0.020	0.000
1700	0.282	0.063	0.052
1400	0.439	0.117	0.166
1180	1.905	1.098	1.398
850	4.558	4.075	4.448
600	7.279	7.354	7.411
425	8.313	8.761	8.296
300	3.906	4.184	3.800
250	3.066	3.309	2.942
212	5.303	5.759	5.084
150	5.191	5.648	5.152
106	2.815	3.060	2.862
90	3.485	3.784	3.572
75	4.654	5.045	4.794
60	6.228	6.720	6.446
45	3.565	3.816	3.707
38	8.019	8.413	8.379
25	8.128	8.153	8.402
15	5.345	5.150	5.282
10	6.930	6.310	6.538
5	1.689	1.443	1.648
4	6.808	5.914	7.484
1	1.986	1.803	2.137

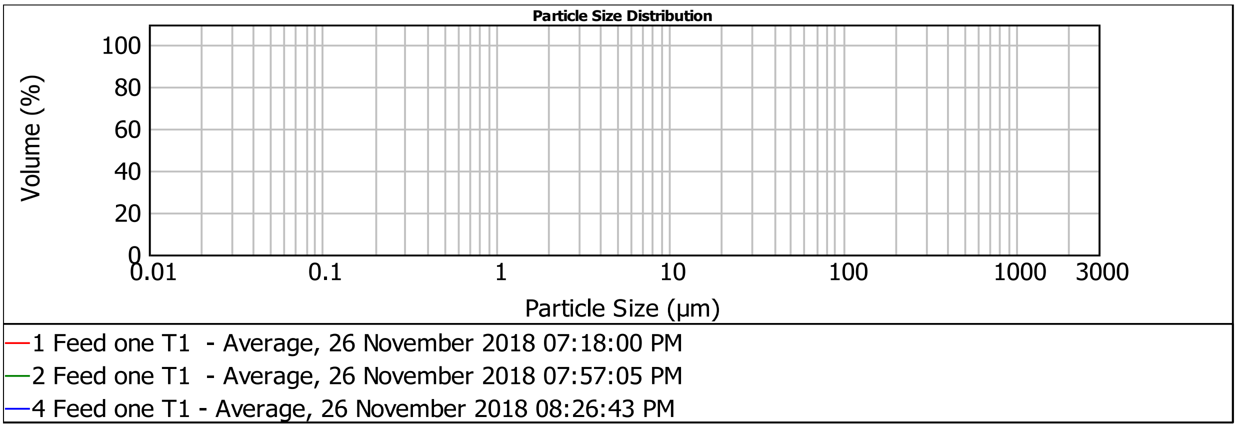

Figure F.13: Feed Sample 1, worn spigot, Malvern Mastersizer 2000 results.

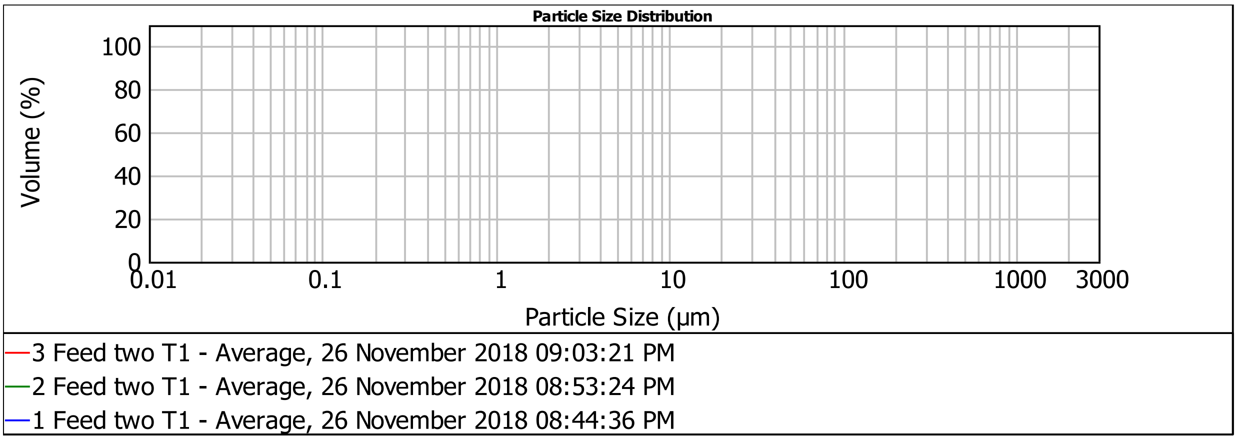

Figure F.14: Feed Sample 2, worn spigot, Malvern Mastersizer 2000 results.

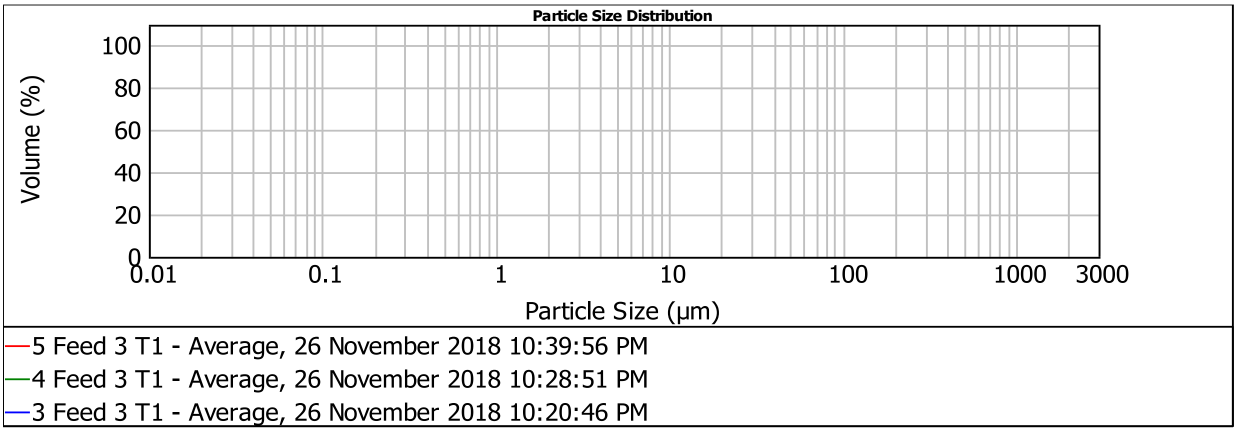

Figure F.15: Feed Sample 3, worn spigot, Malvern Mastersizer 2000 results.

Table F.17: Worn spigot Malvern results.

Under Flow samples - Worn Spigot			
Size (µm)	Sample 1 (vol % retained)	Sample 2 (vol % retained)	Sample 3 (vol % retained)
2000	0.014691	0.025689	0.047018
1700	0.037882	0.0615	0.117923
1400	0.064771	0.084075	0.168615
1180	0.262883	0.36527	0.504158
850	0.662571	0.943702	1.004974
600	1.123462	1.599295	1.519833
425	1.238381	1.816951	1.642009
300	0.573122	0.866171	0.770941
250	0.559902	0.801772	0.719718
212	2.31347	2.71807	2.52766
150	6.326481	6.529952	6.233403
106	5.022916	5.025114	4.828417
90	7.157367	7.088595	6.824563
75	10.511008	10.354961	9.977363
60	14.739444	14.527746	13.984782
45	8.302075	8.230028	7.901131
38	16.408326	16.497513	15.74628
25	10.777304	11.075662	10.575314
15	4.061332	3.983194	4.152242
10	3.802331	2.984268	4.133546
5	0.832995	0.543587	0.939242
4	3.746671	2.697329	4.122519
1	1.460615	1.179556	1.558349

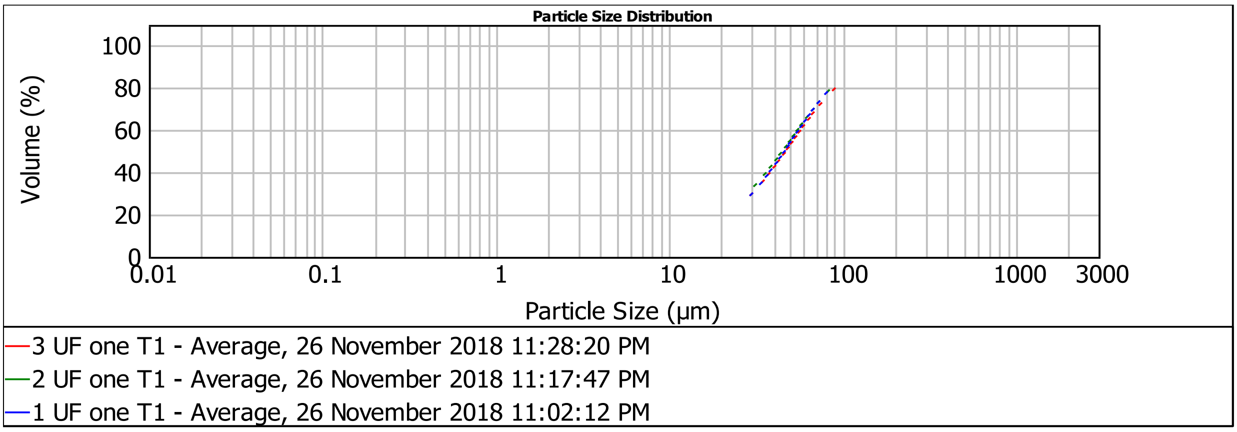

Figure F.16: Underflow Sample 1, worn spigot Malvern Mastersizer 2000 results.

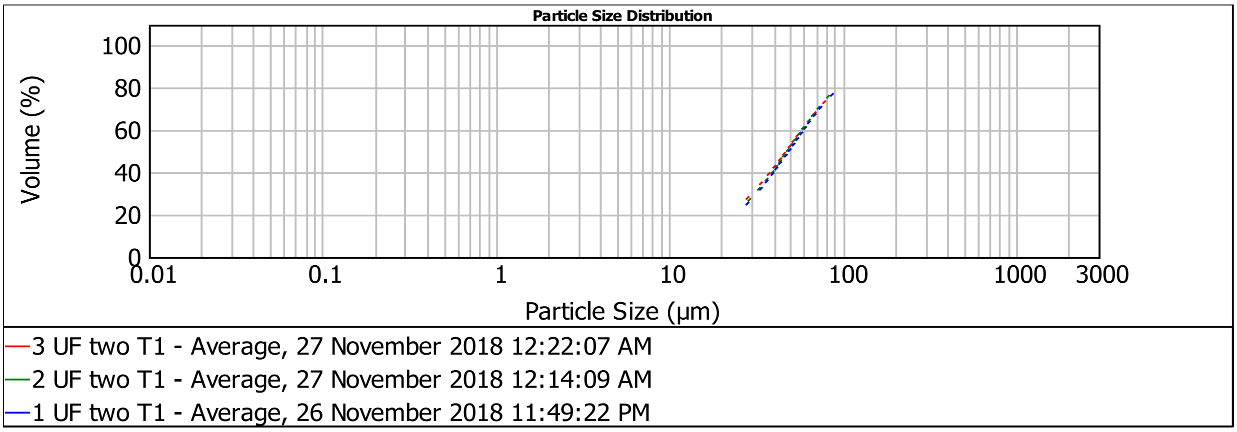

Figure F.17: Underflow Sample 2, worn spigot Malvern Mastersizer 2000 results.

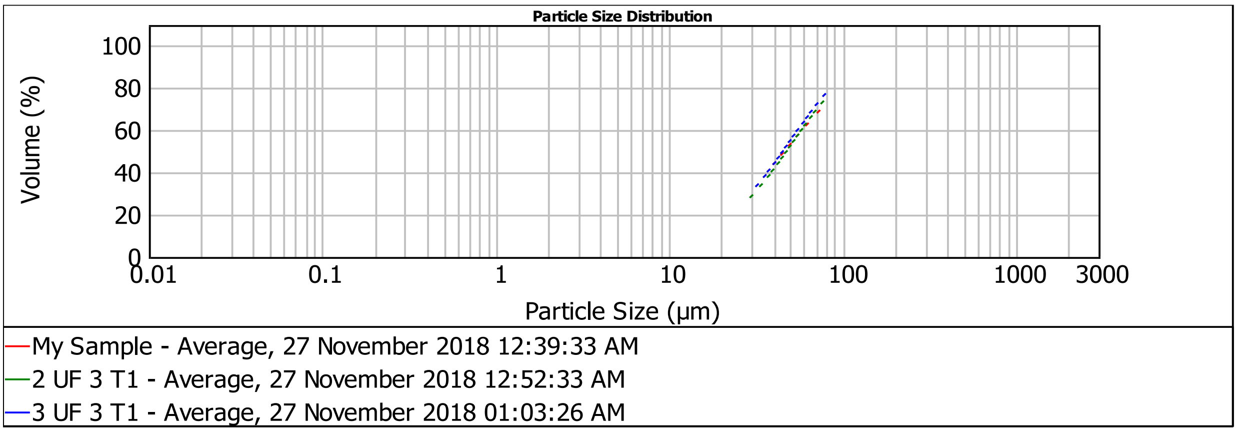

Figure F.18: Underflow Sample 3, worn spigot Malvern Mastersizer 2000 results.

Table F.18: Worn spigot Malvern results.

Overflow Samples - Worn Spigot			
Size (µm)	Sample 1 (vol % retained)	Sample 2 (vol % retained)	Sample 3 (vol % retained)
2000	0	0	0
1700	0	0	0
1400	0	0	0
1180	0	0	0
850	0	0	0
600	0	0	0
425	0	0	0
300	0	0	0
250	0	0	0
212	0	0.012784	0
150	0.246476	0.296005	0.158138
106	0.344592	0.35631	0.24896
90	0.662356	0.699901	0.507767
75	1.413848	1.527151	1.177351
60	3.207692	3.567659	2.895628
45	2.792595	3.145358	2.640827
38	10.197233	11.353083	9.934218
25	17.334623	18.188232	16.901345
15	14.079322	13.663304	13.539544
10	18.073143	16.434193	17.600915
5	4.361549	3.959814	4.417212
4	20.983366	20.442869	22.354556
1	79.016634	6.353337	7.623539

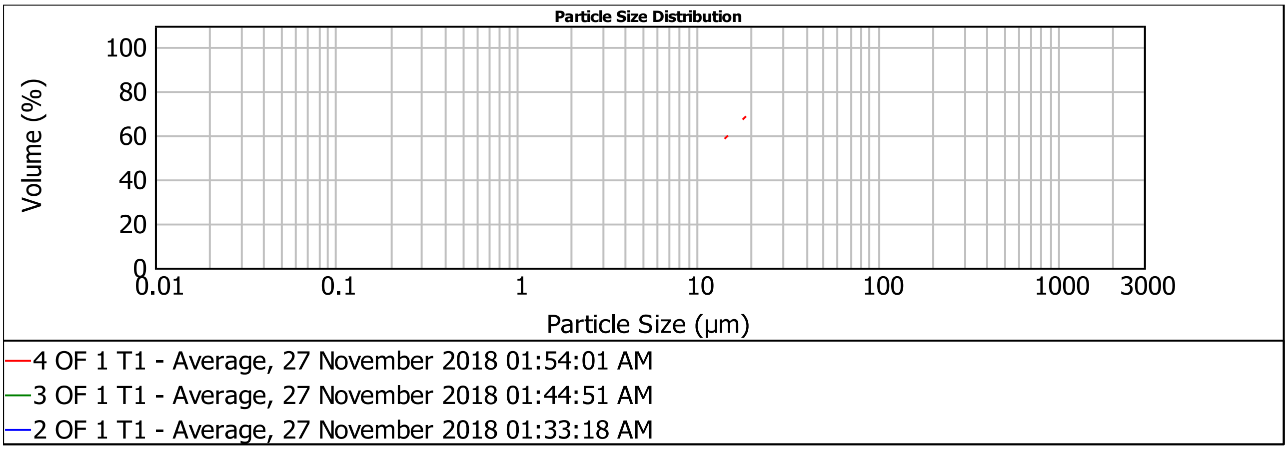

Figure F.19: Overflow Sample 1, worn spigot Malvern Mastersizer 2000 results.

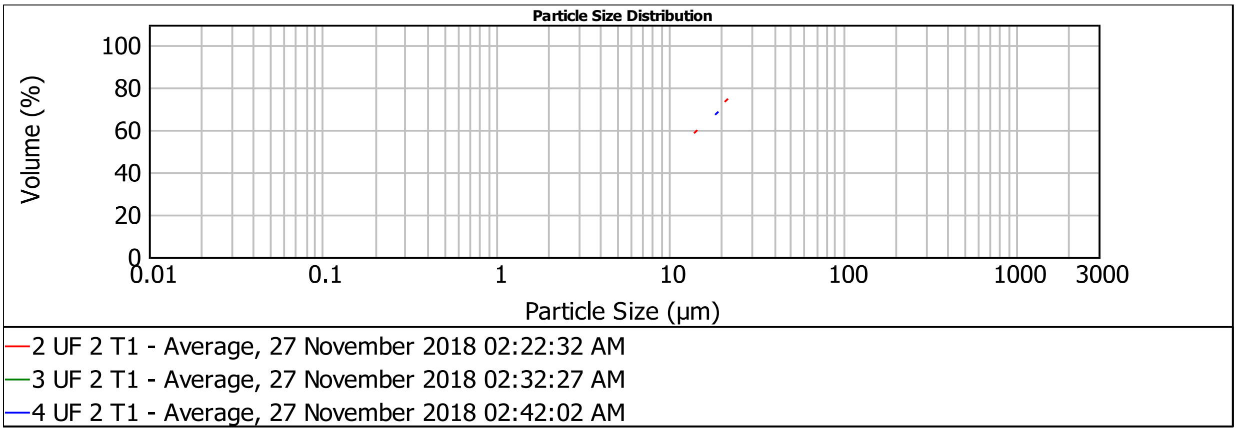

Figure F.20: Overflow Sample 2, worn spigot Malvern Mastersizer 2000 results.

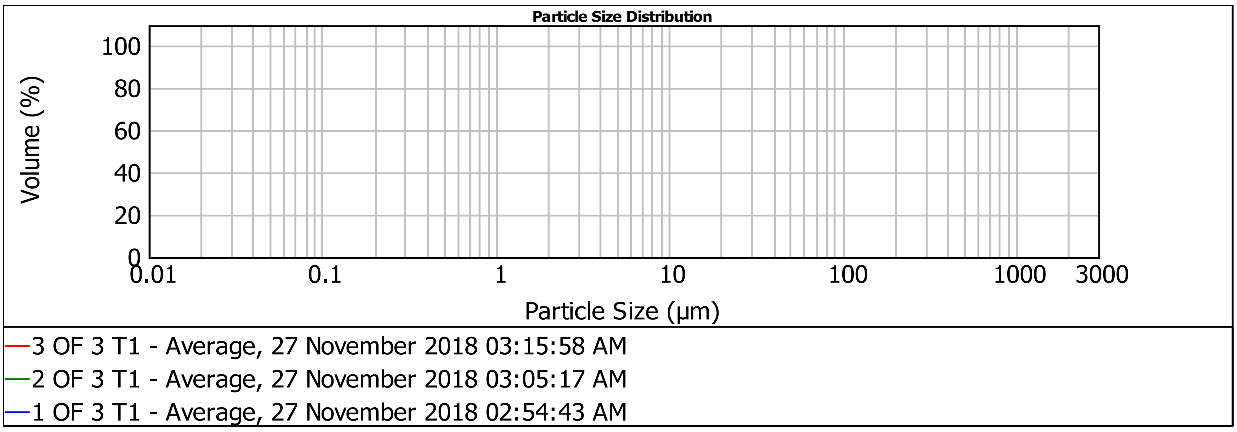

Figure F.21: Overflow Sample 3, worn spigot Malvern Mastersizer 2000 results.

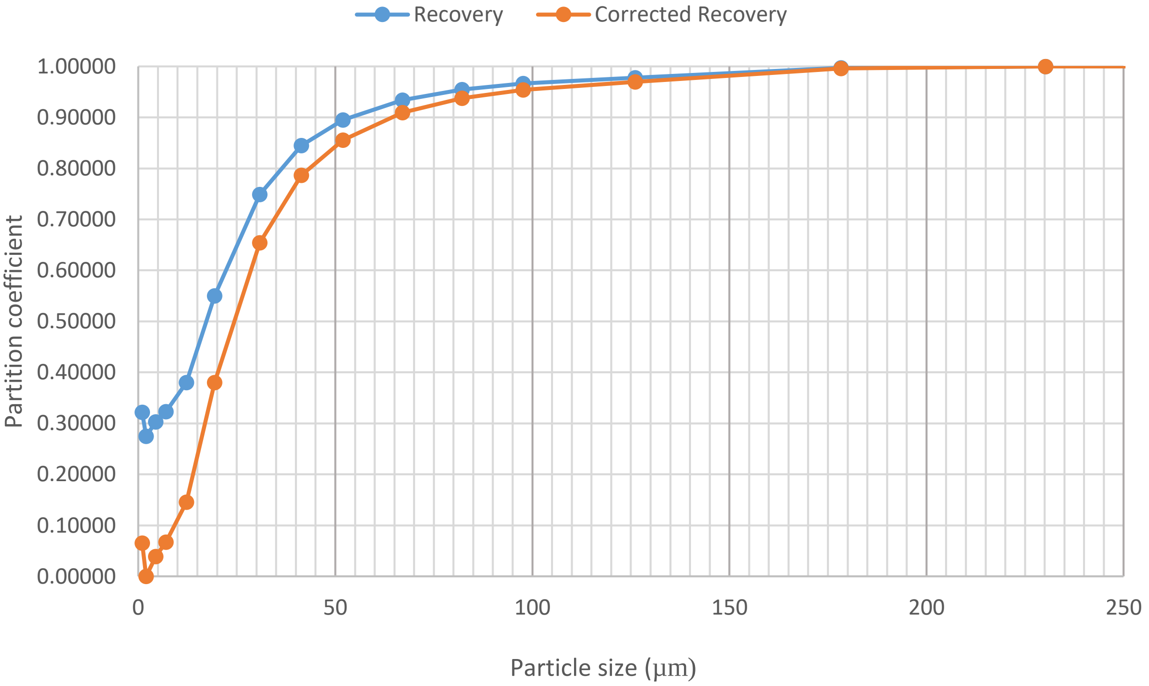

Figure F.22 Recovery to underflow and corrected recovery for worn 50 mm spigot, Sample 1.

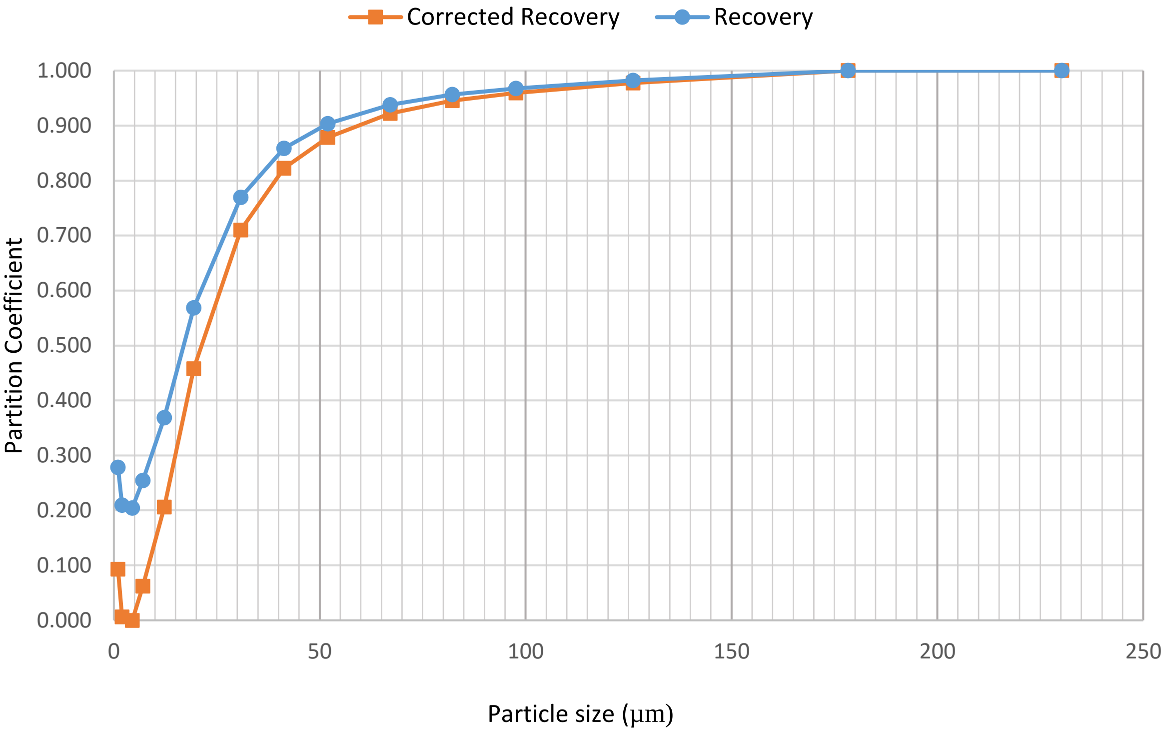

Figure F.23 Recovery to underflow and corrected recovery for worn 50 mm spigot, Sample 2.

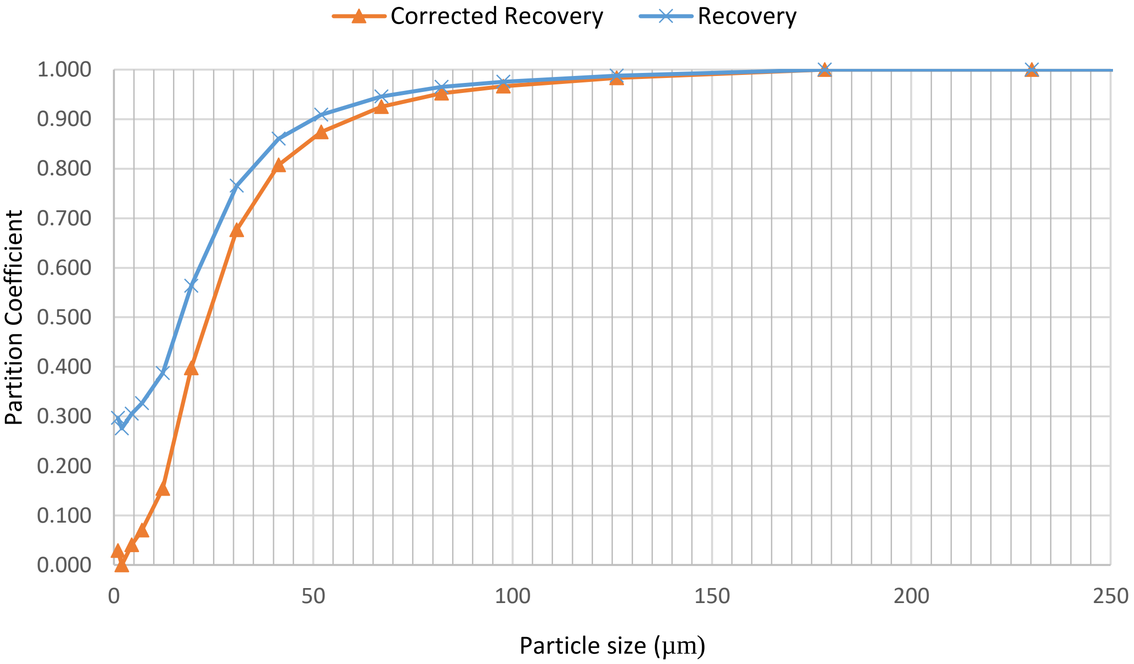

Figure F.24 Recovery to underflow and corrected recovery for worn 50 mm spigot, Sample 3.

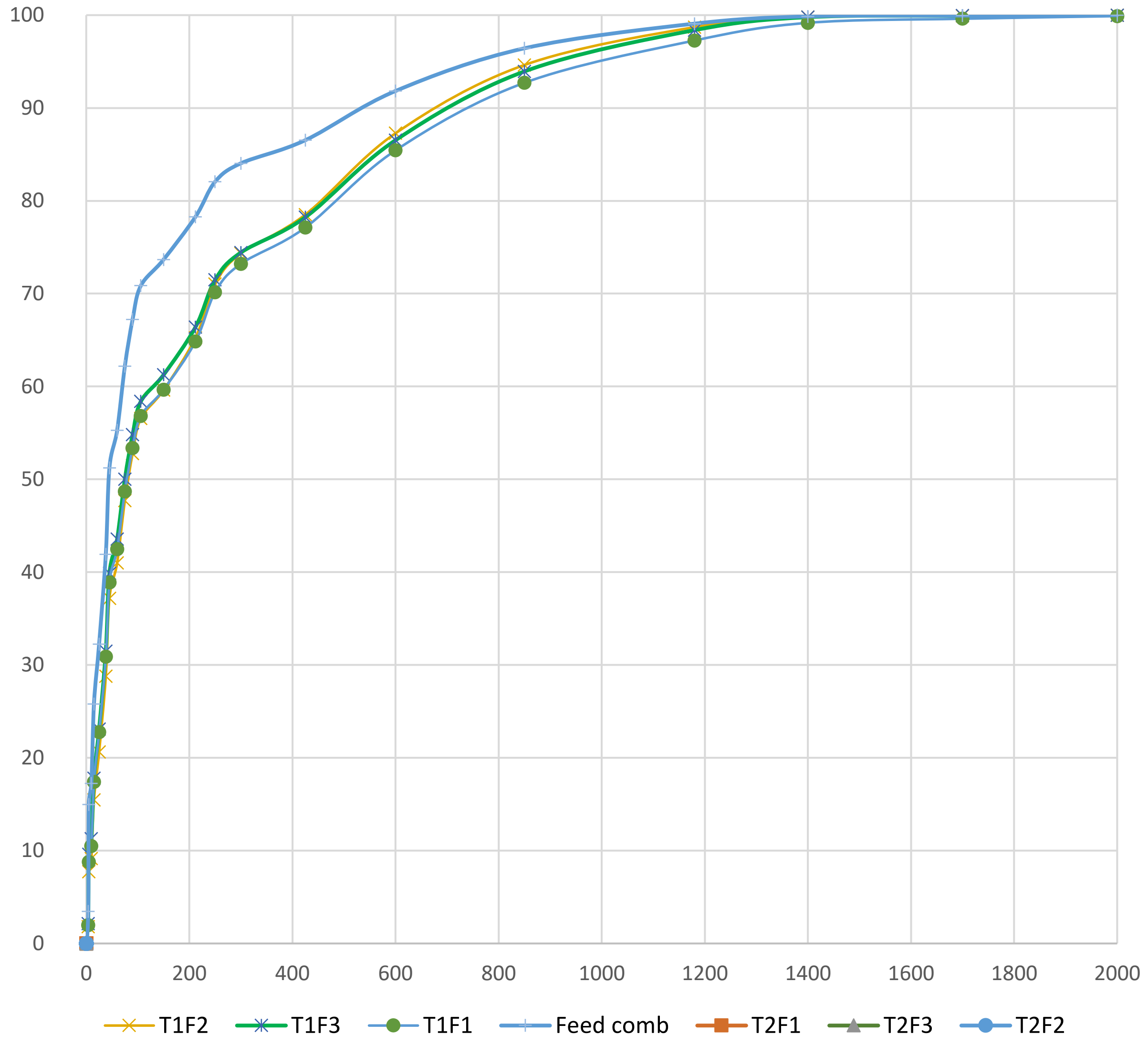

Figure F.25: Feed Malvern results for worn (T1) and new (T2) spigot efficiency tests.

APPENDIX G: PHOTOGRAPHS OF WEAR CHARACTERISTICS

G.1 Cast Iron Wear (Multotec C510-20-0/BB-A/110 (RH) Dense Medium Separation Cyclone)

Figure G.1: Wear pattern on spigot of a cast iron dense medium separation cyclone C510-20-0/BB-A/110 (RH) used for diamonds. The cyclone was in use for six months.

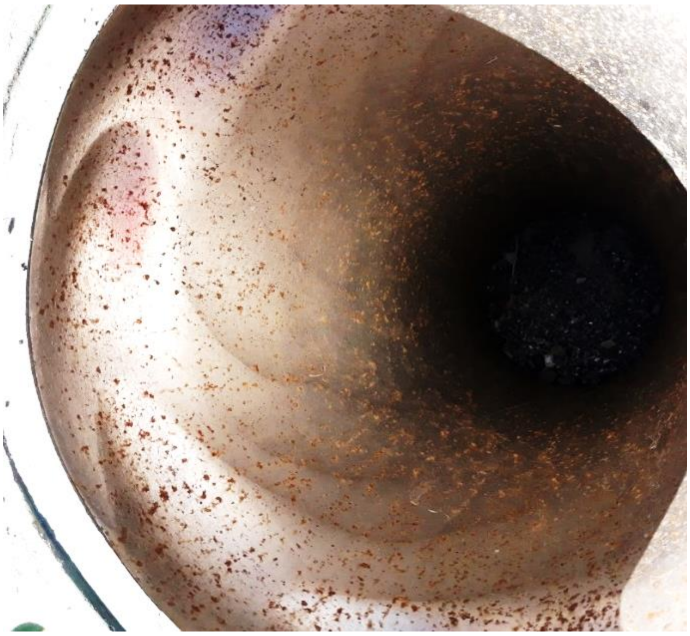

Figure G.2: Wear pattern on top part of a spigot of a dense medium separation cyclone C510-20-0/BB-A/110 (RH) used for diamonds. Top part of mono cone spigot was worn from 220 mm to 226 mm (new); bottom part was worn from 110 mm to 112 mm. The cyclone was in use for six months.

Figure G.3: Wear pattern in inlet and cast iron part of vortex finder of a dense medium separation cyclone C510-20-0/BB-A/110 (RH) used for diamonds. The cyclone was in use for six months.

Figure G.4: Wear pattern at bottom of cone within dense medium separation cyclone C510-20-0/BB-A/110 (RH) used for diamonds. The cyclone was in use for six months.

Figure G.5: Wear pattern on tiled part of overflow outlet of dense medium separation cyclone C510-20-0/BB-A/110 (RH) used for diamonds. The cyclone was in use for 6 months.

a)

b)

Figure G.6: Wear pattern on tiled part of overflow outlet of dense medium separation cyclone C510-20-0/BB-A/110 (RH) used for diamonds. The cyclone was in use for six months.

G.2 Polyurethane Wear (VV Series)

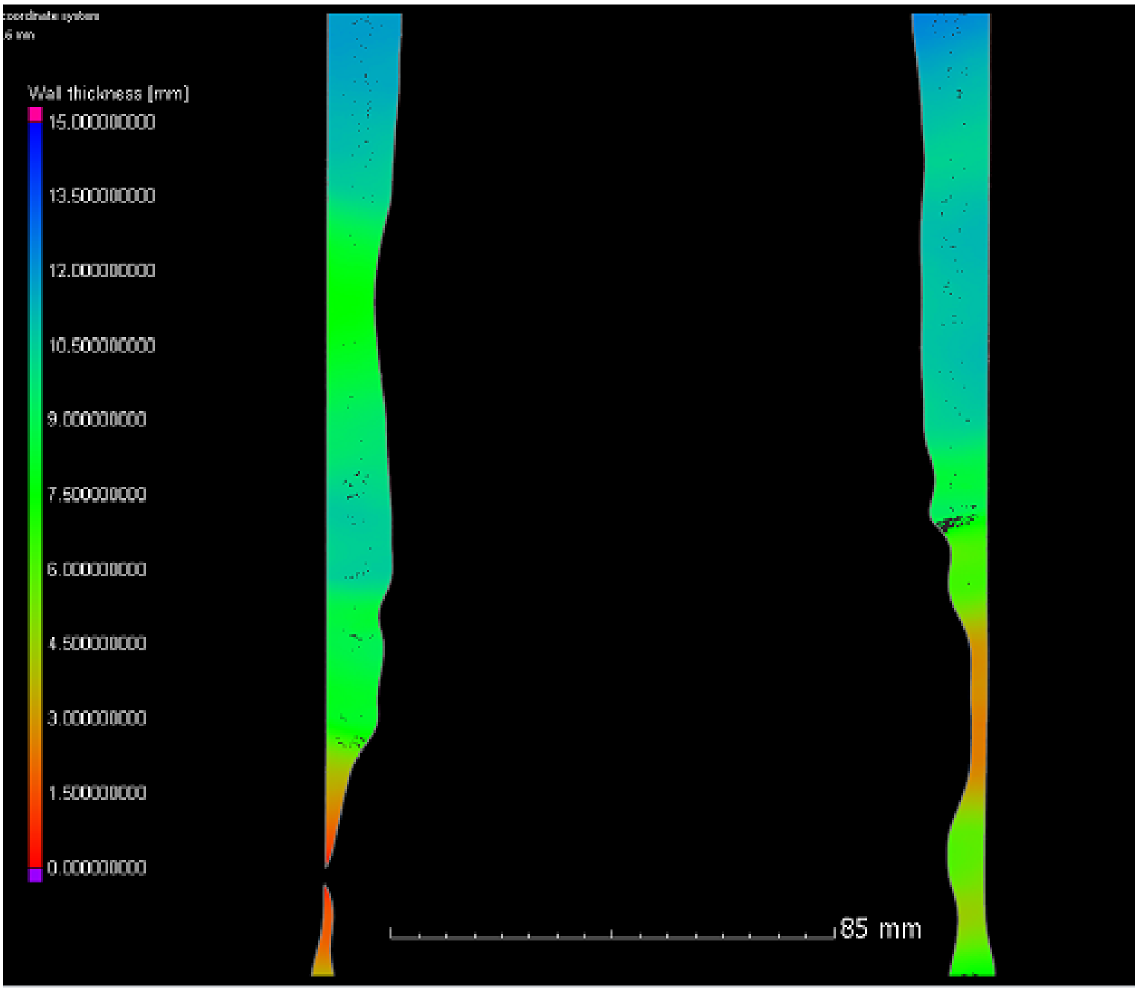

Figure G.7: Micro-computed tomography scan of worn lower cone of polyurethane hydrocyclone.